

# **Controlling Turbulence and Pattern Formation in Chemical Reactions**

von  
Matthias Bertram  
Berlin

Von der Fakultät II - Mathematik- und Naturwissenschaften  
der Technischen Universität Berlin  
zur Erlangung des akademischen Grades

Doktor der Naturwissenschaften  
- Dr. rer. nat. -

genehmigte Dissertation

Promotionsausschuss:

Vorsitzender: Prof. Dr. E. Sedlmayr

Berichter: Prof. Dr. A. S. Mikhailov

Berichter: Prof. Dr. E. Schöll

Berichter: Prof. Dr. H. Engel

Tag der wissenschaftlichen Aussprache: 27. Juni 2002

Berlin 2002

D 83



---

## Zusammenfassung

---

Räumlich ausgedehnte Systeme fern des thermodynamischen Gleichgewichts zeichnen sich durch die Fähigkeit aus, spontan raumzeitliche Strukturen und Turbulenz auszubilden. Die vorliegende Arbeit beschäftigt sich theoretisch und experimentell mit der Steuerung und Kontrolle derartiger Phänomene. Als Beispiel wird die katalytische Oxidationsreaktion von Kohlenmonoxid auf einer Platin-Einkristalloberfläche untersucht. Um Turbulenz zu unterdrücken sowie um neuartige Muster in dieses System zu induzieren werden zwei verschiedene Steuerungsverfahren, globale verzögerte Rückkopplung und periodische Forcierung, eingesetzt.

Die Effekte einer künstlich implementierten globalen Rückkopplungsschleife werden zunächst in einem mathematischen Reaktions-Diffusions-Modell der CO-Oxidation auf Pt(110) mit Hilfe numerischer Simulationen untersucht. Durch Variation eines globalen Kontrollparameters in Abhängigkeit einer räumlich gemittelten Systemgröße lässt sich chemische Turbulenz in dem Modell unterdrücken und ein homogen oszillierender Zustand stabilisieren. Weiterhin kann eine Vielzahl komplexer raumzeitlicher Strukturen, beispielsweise „phase flips“, asynchrone Oszillationen, intermittente Turbulenz in Form chaotischer Kaskaden von Blasen und Ringstrukturen, zelluläre Strukturen und verschiedene Arten von Domänenmustern induziert werden. Die simulierten raumzeitlichen Muster werden mit Hilfe einer zuvor entwickelten Transformation zu Phasen- und Amplitudenvariablen charakterisiert und analysiert. Es zeigt sich, daß die erhaltenen Strukturen große Ähnlichkeit mit dem Verhalten eines generischen Modells, der komplexen Ginzburg-Landau-Gleichung mit globaler Kopplung, aufweisen.

Eine globale verzögerte Rückkopplung kann in Experimenten mit der CO-Oxidation auf Pt(110) durch eine externe, zustandsabhängige Variation des CO-Partialdrucks in der Reaktionskammer realisiert werden. Die sich auf der Platinoberfläche ausbildenden Bedeckungsmuster werden dabei mit Hilfe von Photoemissions-Elektronenmikroskopie sichtbar gemacht. In solchen Experimenten kann chemische Spiralwellenturbulenz erstmals unterdrückt und ein Großteil der vorhergesagten Muster – unter anderem intermittente Turbulenz, Domänenmuster und zelluläre Strukturen – tatsächlich nachgewiesen werden. Die experimentell beobachteten Muster werden ebenfalls durch eine Phasen- und

Amplitudendarstellung charakterisiert.

In weiteren Experimenten wird die Wirkung periodischer Partialdruckmodulationen auf chemische Turbulenz untersucht. Auch mittels dieser Methode lässt sich Spiralwellenturbulenz unterdrücken und eine Vielfalt komplexer Muster induzieren. Als resonante Strukturen sind irreguläre Streifenmuster in subharmonischer Resonanz sowie Domänenmuster mit ko-existenten Resonanzen zu nennen. Zudem treten auch nichtresonante Muster in Form intermittenter Turbulenz und ungeordneter zellulärer Strukturen auf.

Die Resultate dieser Arbeit zeigen somit, daß sich mit Hilfe globaler Rückkopplung und periodischer Forcierung Turbulenz und Strukturbildung in der betrachteten Oberflächenreaktion wirkungsvoll kontrollieren und manipulieren lassen. Ähnliche Phänomene können auch in anderen Reaktions-Diffusions-Systemen erwartet werden.



---

## Abstract

---

Spontaneous pattern formation and spatiotemporal chaos (turbulence) are common features of spatially extended nonlinear systems maintained far from equilibrium. The aim of this work is to control and engineer such phenomena. As an example, the catalytic oxidation of carbon monoxide on a platinum (110) single crystal surface is considered. In order to control turbulence and to manipulate pattern formation in this reaction, two different control methods, global delayed feedback and periodic forcing, are employed.

The effects of a global delayed feedback on the self-organized behavior of the system are first studied numerically in a reaction-diffusion model of CO oxidation on Pt(110). By applying a global control force generated by the spatially averaged state of one of the system variables, turbulence can be suppressed and uniform oscillations can be stabilized. Moreover, global delayed feedback can be used as a tool to produce a variety of complex spatiotemporal patterns, including phase flips, asynchronous oscillations, intermittent turbulence represented by irregular cascades of ring-shaped objects on a uniformly oscillating background, cellular structures, and different types of cluster patterns. The simulated structures are analyzed using a newly developed transformation to phase and amplitude variables designed for non-harmonic oscillations. The obtained patterns resemble the structures exhibited by a general model, the complex Ginzburg-Landau equation with global feedback.

The simulated phenomena of pattern formation are then tested in laboratory experiments with CO oxidation on Pt(110). Global delayed feedback is introduced into the system via a controlled state-dependent variation of the CO partial pressure in the reaction chamber. The spatiotemporal patterns developing on the catalytic surface are imaged by means of photoemission electron microscopy. In such experiments, it is shown that chemical turbulence can be suppressed and a large part of the predicted patterns, including intermittent turbulence, clusters, and cellular structures, can be indeed observed. The experimentally obtained patterns are also transformed into the corresponding spatial distributions of oscillation phase and amplitude.

In a further set of experimental investigations, the effects of periodic external forcing on chemical turbulence in CO oxidation on Pt(110) are studied. Using this method, turbulence can be also suppressed and several complex patterns can be induced. The observed frequency

locked structures are represented by irregular stripes in subharmonic resonance with the forcing and cluster patterns with coexistent resonances. In addition, non-resonant patterns such as intermittent turbulence and disordered cellular structures are found.

Thus, the results of this work demonstrate that by means of global delayed feedback and periodic forcing, turbulence and pattern formation can be effectively controlled and manipulated in the considered surface reaction. Similar phenomena are expected to arise also in other reaction-diffusion systems of various origins.

---

# Contents

---

<b>1</b>	<b>Introduction</b>	<b>1</b>
<b>I</b>	<b>Background</b>	<b>7</b>
<b>2</b>	<b>Theoretical description of reaction-diffusion systems</b>	<b>9</b>
2.1	Limit sets, stability, and bifurcations . . . . .	10
2.2	Bistable, excitable, and oscillatory systems . . . . .	11
2.3	The complex Ginzburg-Landau equation . . . . .	14
<b>3</b>	<b>Strategies for controlling turbulence and pattern formation</b>	<b>19</b>
3.1	Periodic forcing . . . . .	19
3.1.1	Resonance phenomena . . . . .	19
3.1.2	Examples of pattern formation under periodic forcing . . . . .	23
3.2	Global feedback . . . . .	27
3.2.1	Overview of feedback schemes . . . . .	27
3.2.2	Complex Ginzburg-Landau equation with global feedback . . . . .	29
<b>4</b>	<b>Catalytic CO oxidation on platinum (110)</b>	<b>35</b>
4.1	Phenomenological overview . . . . .	35
4.2	Mechanism of the reaction . . . . .	37
4.3	Mathematical modeling . . . . .	40
<b>II</b>	<b>Theoretical Investigations of CO Oxidation on Pt(110)</b>	<b>45</b>
<b>5</b>	<b>Model equations and pattern characterization</b>	<b>47</b>
5.1	Model of CO oxidation with global delayed feedback . . . . .	47
5.2	Numerical methods . . . . .	49
5.3	Transformation to amplitude and phase variables . . . . .	50
<b>6</b>	<b>Pattern formation under global delayed feedback</b>	<b>55</b>
6.1	Manipulating non-chaotic patterns . . . . .	55
6.1.1	Overview of feedback effects . . . . .	55
6.1.2	Phase flips . . . . .	58
6.1.3	Asynchronous oscillations . . . . .	61
6.1.4	Cluster patterns . . . . .	62
6.1.5	Patterns in two space dimensions . . . . .	70
6.1.6	Comparison with the normal form approach . . . . .	75

6.2	Controlling chemical turbulence . . . . .	77
6.2.1	Amplitude turbulence . . . . .	77
6.2.2	Overview of feedback effects . . . . .	79
6.2.3	Intermittent turbulence . . . . .	81
6.2.4	Cluster patterns . . . . .	85
6.2.5	Wave patterns and phase turbulence . . . . .	87
6.2.6	Cellular structures . . . . .	89
6.2.7	Discussion and comparison with the normal form approach . . . . .	91
<b>III</b>	<b>Experiments with CO Oxidation on Pt(110)</b>	<b>95</b>
<b>7</b>	<b>Experimental setup</b>	<b>97</b>
7.1	UHV chamber and sample preparation . . . . .	97
7.2	Visualization of patterns . . . . .	98
7.3	Implementation of the control strategies . . . . .	100
<b>8</b>	<b>Pattern formation under global delayed feedback</b>	<b>103</b>
8.1	Manipulating non-chaotic patterns . . . . .	103
8.1.1	Synchronization and desynchronization of oscillations . . . . .	104
8.1.2	Cluster patterns . . . . .	107
8.1.3	Discussion . . . . .	108
8.2	Controlling chemical turbulence . . . . .	109
8.2.1	Spiral-wave turbulence . . . . .	109
8.2.2	Suppression of turbulence . . . . .	110
8.2.3	Intermittent turbulence . . . . .	112
8.2.4	Cluster patterns . . . . .	115
8.2.5	Standing waves . . . . .	117
8.2.6	Cellular structures . . . . .	118
8.2.7	Discussion . . . . .	120
8.3	Pattern characterization . . . . .	121
8.3.1	Transformation to amplitude and phase variables . . . . .	122
8.3.2	Amplitude and phase patterns . . . . .	123
<b>9</b>	<b>Pattern formation under periodic forcing</b>	<b>127</b>
9.1	Controlling chemical turbulence . . . . .	127
9.1.1	Uniform oscillations . . . . .	128
9.1.2	Irregular oscillatory stripes . . . . .	128
9.1.3	Clusters with coexistent resonances . . . . .	132
9.1.4	Intermittent turbulence . . . . .	133
9.1.5	Cellular structures . . . . .	135
9.2	Discussion . . . . .	136
<b>10</b>	<b>Summary</b>	<b>139</b>
	<b>Bibliography</b>	<b>143</b>

---

# Chapter 1

## Introduction

---

Pattern formation in dissipative systems is a field of research that has been growing rapidly during the last two decades. The field is based on the observation that systems out of thermodynamic equilibrium are capable of generating complex self-organized spatial and temporal patterns (*dissipative structures*) [1]. Prominent examples of such nonequilibrium structures include flow patterns in hydrodynamic systems such as convection rolls and turbulence [2], processes of self-organization in nonlinear optical systems [3, 4] and semiconductors [5], excitation waves in the heart [6], spiral patterns of a signal transmitter in populations of the amoeba *dictyostelium discoideum* [7], and traveling waves and turbulence in chemical reactions [8–10].

The concepts of self-organization and dissipative structures go back to Schroedinger and Prigogine [1, 11–13]. The spontaneous formation of spatiotemporal patterns can occur when a stationary state far from thermodynamic equilibrium is maintained through the dissipation of energy that is continuously fed into the system. While for closed systems the second law of thermodynamics requires relaxation to a state of maximal entropy, *open* systems are able to interchange matter and energy with their environment. By taking up energy of higher value (low entropy) and delivering energy of lower value (high entropy) they are able to export entropy, and thus to spontaneously develop structures characterized by a higher degree of order than present in the environment.

The research direction of *nonlinear dynamics* [14] has substantially contributed to a more detailed understanding of self-organization phenomena far from equilibrium. Studies of nonlinear phenomena can be traced back to Poincaré [15] in the end of the nineteenth century, but first received considerable interest when in the second half of the last century oscillations and traveling wave patterns were observed in chemical reactions [8]. Following studies made possible to quantitatively understand abrupt changes in the behavior of a system

(bifurcations). One of the most important findings was that complex behavior such as *deterministic chaos* [16] is possible even in systems with only a few degrees of freedom.

The interdisciplinary character of the field of nonequilibrium pattern formation is emphasized by the concept of *synergetics* which has been introduced by Haken [17]. In this approach, dissipative structures are analyzed in a system-independent way, based on the observation that there are fundamental similarities between the models that are used to describe phenomena of self-organization in physics, chemistry, biology, and social sciences. Due to this universality, studies devoted to a particular system may also be relevant for other systems of entirely different origin.

The present work is focused on pattern formation in a chemical reaction. Chemical systems are well suited for the investigation of processes of self-organization. They can be operated as open systems by constant supply of fresh reagents and continuous removal of the products. Moreover, the kinetics of many reactions are sufficiently well understood and they can be conducted under well-defined conditions. In typical experiments (e.g., experiments in liquid phase that employ an open gel reactor [18]), advective motion of the reagents is prevented and spatiotemporal concentration patterns arise from the interplay of reaction and diffusion processes.

Pattern formation in chemical reaction-diffusion systems is closely related to the spontaneous appearance of temporal oscillations in a corresponding system without spatial degrees of freedom. The most prominent example of a pattern forming chemical system is the Belousov-Zhabotinsky (BZ) reaction [8], which is a homogeneously catalyzed reaction in aqueous solution. It involves several reagents and various intermediate species; the central reaction step is the oxidation of malonic acid by bromate, catalyzed by metal ions. Chemical oscillations in the BZ system were first reported by Belousov in 1951 (see Ref. [19]) in a continuously stirred reactor. Two decades later, Zhabotinsky and Winfree observed traveling waves of chemical activity in an unstirred reactor [20,21]. Since then, the majority of studies of pattern formation in chemical reactions have focused on the BZ reaction [8,9].

Typical nonequilibrium phenomena in chemical reaction-diffusion systems include the formation of traveling waves and rotating spiral waves, target patterns, and spatiotemporal chaos (turbulence) [22,23]. The properties of spiral waves have been extensively studied for many years. Recent studies of the BZ reaction identified different spiral instabilities leading to spiral breakup and turbulence [24]. Alternatively, chemical turbulence may spontaneously develop from a uniformly oscillating state in absence of spiral waves [25]. In systems with

strongly differing diffusion constants for the individual species also stationary, spatially periodic patterns (hexagons and stripes) can occur. The mechanism for the formation of such structures was proposed already in 1952 by Turing [26] in the context of morphogenesis, but it was not before 1990 that they were observed experimentally in a chemical system [27,28].

A problem of much practical and scientific interest is to control and engineer pattern formation in spatially extended nonequilibrium systems. The main objectives are control of spatiotemporal chaos, modification of existing patterns, and production of new kinds of patterns. Controlling and understanding spatiotemporal chaos is one of the central problems in nonlinear dynamics. By exploring the response of a self-organizing chaotic or regular system to an external stimulus, one can gain information on the principles and mechanisms of pattern formation. Such studies are particularly important to understand the behavior of natural systems subject to external driving forces (e.g., circadian rhythm). The control of complex nonequilibrium systems also offers a variety of potential applications. For instance, by externally applying an acting force, one can potentially increase the yield and selectivity of chemical reactions taking place in cars, chemical factories, or the atmosphere [29–31]. Spatiotemporal chaos usually is undesired in industrial processes, and chaos control may improve their performance. The production of well-defined patterns may, for example, prove important for information storage and retrieval in distributed systems.

In order to control pattern formation and turbulence in spatially extended systems, global control methods are practical since local access to all system elements is often difficult to achieve. Global methods act on a single parameter that affects the dynamics of the entire medium. In the present work, two different types of global control strategies, uniform periodic forcing and global delayed feedback, are used to control pattern formation and turbulence in a surface chemical reaction. In case of periodic forcing, the control signal is given *a priori*, whereas it adjusts to the current state of the medium when feedback control is implemented. Previous studies performed in the framework of abstract models have theoretically investigated the effects of periodic forcing [32–35] and different schemes of global feedback [36–38], suggesting that turbulence and pattern formation can be successfully controlled in reaction-diffusion systems. Recent experimental studies [39–42] employing the oscillatory Belousov-Zhabotinsky reaction concentrated on the application of global control methods in a non-turbulent parameter regime and showed the formation of several types of spatiotemporal structures.

The reaction considered in this work is the catalytic oxidation of carbon monoxide on a platinum(110) single crystal surface, an idealized setting of the reaction that proceeds in

the catalytic converter of a car exhaust. In contrast to catalytic reactions in liquid phase such as the BZ reaction, surface reactions represent *heterogeneously* catalyzed chemical systems, where catalyst and reagents are present in different phases. The investigation of oscillatory surface reactions has a tradition of several decades (see Ref. [43] for a review). The systematic exploration of oscillations and spatiotemporal patterns in such systems has been started by Ertl and co-workers [44, 45]. Among surface chemical reactions, by far the richest variety of spatiotemporal patterns has been found in CO oxidation on Pt(110). The observed phenomena include propagating and standing waves, rotating spirals, target patterns, and turbulence [46]. The CO oxidation reaction on Pt(110) involves only a few species and its mechanism is well understood.

The effects of global delayed feedback on the self-organized behavior of CO oxidation on Pt(110) are studied both in a theoretical model of this reaction and in laboratory experiments. Two cases are considered, differing by the state of the unperturbed reaction: in the first case the system displays stable uniform oscillations or stable rotating spiral waves, while the second case is characterized by the presence of chemical turbulence. The influence of periodic forcing on pattern formation is studied in the second case and experimentally only. It is found that the chosen control methods allow to suppress turbulence, and that they can be successfully used as a tool to produce various complex patterns.

The following chapters are divided into three parts. The first part (Chapter 2-4) describes the background of this work. First a brief introduction into pattern formation and turbulence in reaction-diffusion systems is given in Chapter 2. Following this, the later used control methods – periodic forcing and global feedback – are explained and some of their possible effects are illustrated in Chapter 3. Subject of Chapter 4 is an introduction into phenomena, mechanism, and mathematical modeling of catalytic CO oxidation on Pt(110).

The theoretical investigations of CO oxidation on Pt(110) are presented in the second part of this work (Chapter 5-6). In Chapter 5, first the equations used for mathematical modeling are specified and their numerical implementation is briefly discussed. Then a method for the interpretation of simulated patterns is developed which allows a transformation of model variables into amplitude and phase variables. Thereafter, in Chapter 6, a detailed numerical study of CO oxidation under global delayed feedback is presented. In two different series of simulations, such feedback is applied first in a non-chaotic parameter regime, and then to control spatiotemporal chaos in the model. In both cases, various different spatiotemporal structures are obtained and subsequently analyzed.



The third part of this work (Chapter 7-9) is devoted to surface chemical experiments employing the CO oxidation on Pt(110). The used experimental setup is described in Chapter 7. In Chapter 8, experiments with global delayed feedback are reported that have been performed to test the theoretical predictions made in Chapter 6. Both in a non-chaotic and in a turbulent parameter region, several previously predicted spatiotemporal patterns are observed. The amplitude and phase characterization of such structures is achieved by employing a similar technique as was used before to analyze the simulated patterns. Furthermore, in Chapter 9, experiments with uniform periodic forcing are reported. The effects of such forcing are studied in the case when the unforced reaction exhibits chemical turbulence. Finally, the results of this work are summarized in Chapter 10.



**Part I.**  
**Background**



---

## Chapter 2

# Theoretical description of reaction-diffusion systems

---

Subject of this work are phenomena of spatiotemporal pattern formation in systems of reaction-diffusion type. In this chapter, the theoretical background of reaction-diffusion systems is described. Consider a spatially extended medium consisting of many identical active elements with deterministic dynamics. The momentary state of each individual element shall be uniquely defined by a set of variables  $\mathbf{u} = (u_1, u_2, \dots, u_n)$ . Assuming diffusive interaction between the elements, the spatiotemporal dynamics of the distributed system  $\mathbf{u}(x, t)$  in the continuum limit shall be governed by a set of coupled, in general nonlinear partial differential equations (PDE's) of the form

$$\frac{\partial \mathbf{u}}{\partial t} = \mathbf{f}(\mathbf{u}, \mathbf{p}) + \mathbf{D} \nabla^2 \mathbf{u} , \quad (2.1)$$

where  $\mathbf{f}$  denotes a set of  $n$  differentiable functions  $f_i$ ,  $\mathbf{p}$  represents the system parameters, and  $\mathbf{D}$  is the diffusion matrix. In chemical systems, the variables  $u_i$  may represent different chemical species and the functions  $f_i$  describe the reaction kinetics. It is assumed that diffusion follows *Fick's second law*,  $\partial_t u = D \nabla^2 u$  (provided that diffusion is constant in space). When the reagents diffuse independently of each other, the diffusion matrix has diagonal form.

The above description is a mean field approach, implying a characteristic diffusion length  $l = \sqrt{D\tau}$ , where  $\tau$  is the characteristic time scale of the reaction. To accurately describe phenomena occurring on spatial scales smaller than  $l$ , nanoscopic or mesoscopic approaches are necessary (see, e.g., Ref. [47]).

Reaction-diffusion systems of the form (2.1) are capable of generating a broad variety of complex spatiotemporal patterns [22, 23]. Such structures result from the interaction of nonlinear local dynamics (reaction) and spatial coupling due to diffusion. To understand

the collective behavior of distributed systems, it is helpful to first consider the dynamics of isolated elements, while neglecting their mutual interaction. This is done in Section 2.1. In Section 2.2, active media are classified into bistable, excitable, and oscillatory systems, and their basic properties are discussed. A standard model of a distributed oscillatory system, the complex Ginzburg-Landau equation, is described in Section 2.3. Its regular and spatiotemporally chaotic solutions provide generic examples of oscillatory reaction-diffusion patterns.

## 2.1 Limit sets, stability, and bifurcations

The dynamics of a single element of an active medium is obtained from equation (2.1) by simply dropping the diffusion term. This yields a usually low-dimensional set of  $n$  coupled ordinary differential equations (ODE's) of the form

$$\dot{\mathbf{u}} = \mathbf{f}(\mathbf{u}, \mathbf{p}) . \quad (2.2)$$

The theory of low-dimensional nonlinear dynamical systems is well established [14, 16, 48]. Dynamical processes correspond to trajectories in phase space spanned by the variables  $(u_1, u_2, \dots, u_n)$ . Starting from an initial condition  $\mathbf{u}(t_0)$ , the trajectory of the solution  $\mathbf{u}(t)$  is uniquely defined because the time derivative in system (2.2) is of first order. The subsets of phase space that are approached by the trajectories as  $t \rightarrow \pm\infty$  are called *limit sets*. Attractors are limit sets that are approached in the limit  $t \rightarrow +\infty$ . They may correspond to stationary, periodic, quasiperiodic, or chaotic dynamical states.

The stationary limit sets (fixed points)  $\mathbf{u}^*$  of system (2.2) fulfill the condition  $\dot{\mathbf{u}} = 0$ . The linear stability of such a fixed point  $\mathbf{u}^*$  is tested by perturbing it slightly,  $\mathbf{u} = \mathbf{u}^* + \delta\mathbf{u}$ . After linearization with respect to  $\delta\mathbf{u}$ , the perturbation then evolves according to the equation

$$(\dot{\delta\mathbf{u}}) = \mathbf{J}(\mathbf{u}^*) \delta\mathbf{u} , \text{ where } \mathbf{J}_{ij} = \frac{\partial f_i}{\partial u_j} . \quad (2.3)$$

Thus, the eigenvalues  $\lambda_1, \dots, \lambda_n$  of the linear evolution matrix  $\mathbf{J}$  evaluated at a fixed point  $\mathbf{u}^*$  govern its stability. The fixed point is stable if the real parts of all eigenvalues  $\lambda_i$  are negative; it is unstable if the real part of at least one eigenvalue is positive.

In two-dimensional phase space, the eigenvalues  $\lambda_1$  and  $\lambda_2$  may either be real or complex conjugated. Thus, five different types of fixed points are possible, see Fig. 2.1. Two real negative (positive) eigenvalues correspond to a stable (unstable) node, and a saddle point is given by the combination of one positive and one negative real eigenvalue. Complex conjugated eigenvalues correspond to a focus, whose stability depends on the real parts.

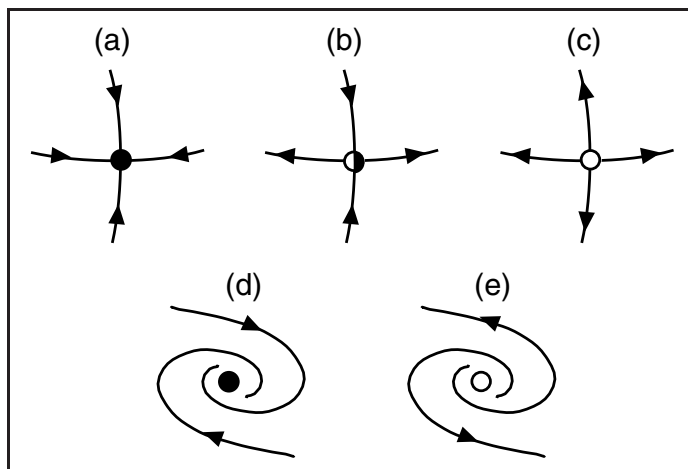


Figure 2.1: Fixed points in two-dimensional phase space: (a) stable node, (b) saddle point, (c) unstable node, (d) stable focus, and (e) unstable focus.

The stability of a fixed point may be changed when at least one of the eigenvalues changes its sign, a process which is termed *bifurcation*. The simplest example of a bifurcation leading to nonstationary dynamical behavior is the supercritical Hopf bifurcation, see Fig. 2.2. As an appropriate control parameter  $\mu$  is varied beyond its critical value  $\mu_c$ , a stable focus becomes unstable and simultaneously a stable limit cycle is born. Sufficiently close to the bifurcation point, the associated oscillations are harmonic and their amplitude grows as  $A \sim \sqrt{\mu - \mu_c}$ . At a larger distance from threshold, the oscillations might become strongly anharmonic, depending on the properties of a given system.

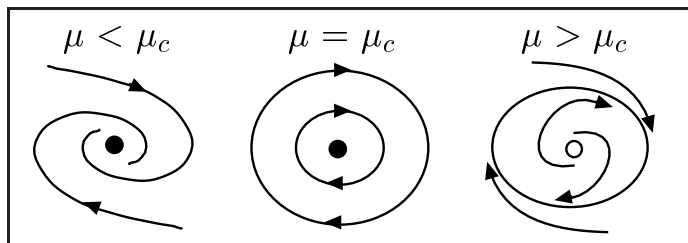


Figure 2.2: Phase space portraits in the vicinity of a supercritical Hopf bifurcation.

Further examples of local bifurcations include the subcritical variant of the Hopf bifurcation, where an unstable focus changes into a stable focus and an unstable limit cycle, and the saddle-node bifurcation, where a saddle point and a node are created (or destroyed). More detailed discussions of limit sets and their stability can be found in Ref. [49].

## 2.2 Bistable, excitable, and oscillatory systems

Depending on the number and kind of limit sets, the dynamical behavior of many systems of the form (2.2) can be classified as monostable, bistable, excitable, or oscillatory [22]. In this section, this classification is illustrated by considering the nullclines of a system of two

variables  $u_1$  and  $u_2$ . The nullclines are defined as the lines in phase space obeying  $\dot{u}_1 = 0$  and  $\dot{u}_2 = 0$ . Their intersection points are the fixed points of the system. Schematic drawings of the phase space in the cases of bistable, excitable, and oscillatory dynamics are displayed in Fig. 2.3.

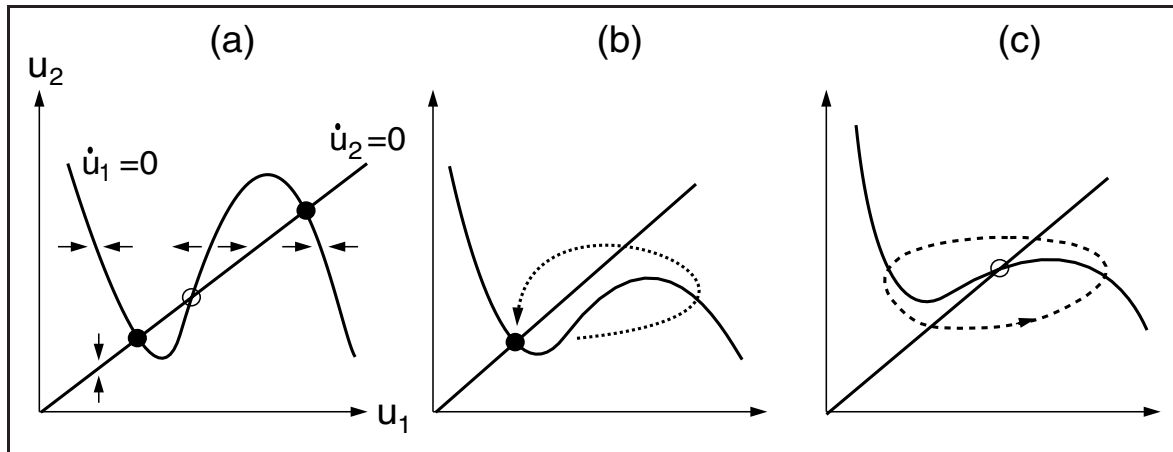


Figure 2.3: Schematic phase space drawings illustrating (a) bistable, (b) excitable, and (c) oscillatory dynamics.

### Bistable systems

The nullclines of bistable systems typically possess three intersection points, which correspond to two stable fixed points separated by a saddle point. This situation is illustrated in Fig. 2.3(a). The direction of the flow is indicated by small arrows. The straight nullcline  $\dot{u}_2 = 0$  is attracting with respect to  $u_2$ : the value of  $u_2$  decreases above the nullcline, whereas it increases below. Accordingly, the declining branches of the nullcline  $\dot{u}_1 = 0$  are stable with respect to changes in  $u_1$ ; however, its rising middle branch is unstable. To carry over the system state from one stable fixed point to the other, a sufficiently strong perturbation that crosses the middle branch of the nullcline  $\dot{u}_1 = 0$  is needed. In a distributed system consisting of many diffusively coupled bistable elements, the propagation of a front (*trigger wave*) can induce such a transition. Trigger waves travel with constant velocity and represent the basic type of pattern in extended bistable media.

### Excitable systems

Excitable systems are characterized by special dynamical properties in the vicinity of a stable fixed point. Small (subthreshold) perturbations of the stationary state straightly decay, but sufficiently large (superthreshold) perturbations induce a long excursion in phase space



before the system again relaxes to its stationary state. The trajectory of such an excitation is depicted in Fig. 2.3(b). The rising branch of the nullcline  $\dot{u}_1 = 0$  acts as excitation threshold. The time needed to recover from an excitation is called the refractory period of a system. Typically, excitable elements cannot be excited again within this period.

Spatially extended excitable media can support the steady propagation of excitation waves. The system relaxes in the tail of a traversing pulse and, in contrast to trigger waves in bistable systems, subsequent identical pulses may pass through the same region, one after another. Pulses usually annihilate upon head-on collisions. In two space dimensions, broken excitation waves can curl and form self-sustained rotating spiral waves. The shape and rotation frequency of such spirals are uniquely determined by the properties of the medium. Furthermore, rigidly rotating spiral waves may undergo instabilities leading to meandering of the spiral tip [50] and, via spiral breakup, to turbulence in excitable media [51].

### Oscillatory systems

Periodic oscillatory systems are characterized by the presence of an unstable fixed point and a stable limit cycle. This situation is illustrated in Fig. 2.3(c) where the nullclines intersect on the unstable branch of  $\dot{u}_1 = 0$ . The limit cycle is depicted by the dashed line. In autonomous systems of the form (2.2), trajectories cannot intersect in phase space, and therefore periodic limit cycle oscillations are the most complex type of oscillatory behavior possible in the case of two independent variables. In systems described by three or more variables, chaotic oscillations are also possible. Throughout this work, only spatially extended media are considered whose isolated elements display periodic oscillations.

Typical spatiotemporal patterns in diffusively coupled arrays of periodic oscillators include rotating spiral waves, target patterns, and spatiotemporal chaos (turbulence). The rotation frequency of spiral waves is, as in excitable media, a unique property of a given medium. Target patterns are patterns of concentric waves sent out by a wave source called pacemaker. Target waves are typically emitted by inhomogeneities of a medium, but in homogeneous systems described by at least three independent variables also stable self-organized pacemakers are possible [52, 53]. Turbulence occurs when diffusive coupling destabilizes uniform oscillations. This situation is encountered when existing phase gradients are steepened by diffusion rather than damped.

To understand the latter behavior, it is instructive to consider the phase dynamics of a field of periodic (but possibly anharmonic) oscillators [22, 25]. The momentary state of each oscillating element shall be given by its oscillation amplitude and phase. Under the condition that

the variation of the oscillation phase across the medium is sufficiently smooth, the characteristic time scale for the evolution of phase distributions is large as compared to the amplitude relaxation time for an individual oscillator. Then a universal phase equation can be derived. This equation describes the dynamical evolution of the (smooth) phase distribution  $\phi(x, t)$  and is of the generic form

$$\frac{\partial \phi}{\partial t} = a (\nabla \phi)^2 + b \nabla^2 \phi, \quad (2.4)$$

where the coefficients  $a$  and  $b$  depend on the particular system. By the Hopf-Cole transformation  $\phi = (b/a) \ln Q$ , equation (2.4) can be reduced to the linear equation

$$\frac{\partial Q}{\partial t} = b \nabla^2 Q. \quad (2.5)$$

If the coefficient  $b$  is positive, equation (2.5) is a standard diffusion equation and any localized perturbation in  $Q$  (and therefore also in  $\phi$ ) spreads out and decays as time proceeds. In contrast, if the value of  $b$  is negative, a localized perturbation increases in magnitude. Fluctuations on the smallest spatial scale typically show the most rapid growth. However, as phase variations are steepened, the condition of a sufficiently smooth phase field may no longer be fulfilled, and equation (2.4) may not be applicable anymore. Then the resulting turbulent state cannot be consistently described within the phase dynamics approximation and its properties must be determined from the complete set of reaction-diffusion equations. However, a universal description is possible for systems close to a supercritical Hopf bifurcation. This approach is followed in the next section.

## 2.3 The complex Ginzburg-Landau equation

The derivation of an amplitude equation leads to a simplified description of the universal properties of a system close to a bifurcation point [9, 25]. The behavior of any reaction-diffusion system that undergoes a supercritical Hopf bifurcation, regardless of its nature, is described by the complex Ginzburg-Landau equation (CGLE). Though the CGLE is strictly valid only sufficiently close the onset of oscillations, its predictions may remain qualitatively correct in a larger neighborhood of the bifurcation. The CGLE is one of the most-studied equations in nonlinear physics (see Ref. [54] for a recent review). It displays a wealth of phenomena, ranging from stable plane waves and spiral waves to spatiotemporal chaos. Selected solutions of the CGLE are discussed below, because they provide generic examples

of regular and turbulent spatiotemporal regimes that will be referred to in later parts of this work.

The CGLE describes harmonic oscillations in terms of the complex amplitude  $A = |A|e^{i\phi}$ , where  $|A|$  is the amplitude modulus and the phase is given by  $\phi = \arg(A)$ . In rescaled, dimensionless form the evolution equation for the complex field  $A(x, t)$  reads

$$\frac{\partial A}{\partial t} = (1 - i\omega)A - (1 + i\beta)|A|^2A + (1 + i\varepsilon)\nabla^2 A, \quad (2.6)$$

where  $\beta$  and  $\varepsilon$  are real parameters denoting the nonlinear shift of the oscillation frequency and the dispersion coefficient, respectively. The term  $(-i\omega A)$  can be eliminated by going to a rotating coordinate frame  $A \rightarrow A \exp(i\omega t)$  and therefore is often omitted. The derivation of the CGLE parameters from a reaction-diffusion system is explained in Refs. [25, 55].

The dynamics of a single isolated element is described by omitting the diffusion term  $(1 + i\varepsilon)\nabla^2 A$  in equation (2.6). Such an element performs harmonic limit cycle oscillations  $A = \exp(-i\omega_0 t)$  with frequency  $\omega_0 = \omega + \beta$ . In the distributed system, it follows from a linear stability analysis that the state of uniform oscillations is unstable with respect to small perturbations if the *Benjamin-Feir condition*

$$1 + \varepsilon\beta < 0. \quad (2.7)$$

is satisfied. The Benjamin-Feir instability corresponds to the occurrence of a negative coefficient  $b$  in the phase dynamics equation (2.5).

The chaotic spatiotemporal regimes beyond the Benjamin-Feir instability are known as chemical turbulence [23, 25]. When crossing the Benjamin-Feir boundary with spatially almost uniform initial conditions, at first *phase turbulence* develops. This state is characterized by weak phase and amplitude variations, such that trajectories still lie in the vicinity of uniform oscillations. In one space dimension, narrow regions with increased oscillation amplitude (*shocks*) randomly travel through the medium, see Fig. 2.4(a) for an example. Statistical analysis reveals that, though this state is chaotic, long-range spatial correlations are retained and oscillations of distant elements remain almost synchronous [56].

Farther away from the Benjamin-Feir boundary, strong phase fluctuations become more probable, such that phase slips occur with a nonzero average rate. Phase slips correspond to dynamical defects which are represented by narrow regions in the amplitude field where  $|A|$  locally nearly vanishes, see Fig. 2.4(b). The transition from phase turbulence to such *amplitude turbulence* (or defect turbulence) is characterized by a qualitative change of the spatial

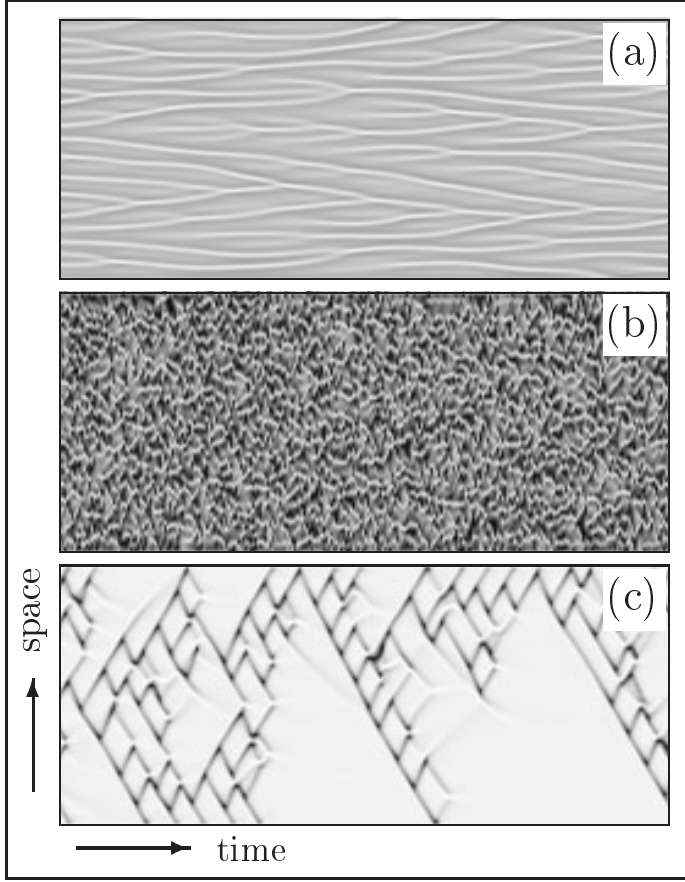


Figure 2.4: *Different turbulent regimes in the one-dimensional CGLE: (a) phase turbulence, (b) amplitude turbulence, and (c) intermittent turbulence. The space-time diagrams display the real oscillation amplitude  $|A|$  in gray scale; defects are seen in (b) and (c) as dark spots. The system size is  $L = 256$  and the time interval shown is  $\Delta t = 500$ . The parameters are (a)  $\beta = -1$ ,  $\varepsilon = 1.5$ , (b)  $\beta = -2$ ,  $\varepsilon = 2$ , and (c)  $\beta = -1.4$ ,  $\varepsilon = 0.6$ .*

correlation function for the complex amplitude. The correlation radius decreases strongly as defects appear in the system and becomes close to the mean distance between the defects [56].

Depending on the values of  $b$  and  $\varepsilon$ , the transition between phase and amplitude turbulence may involve hysteresis. For appropriate parameter values, there is a region termed bichaos where both phase and amplitude turbulence can occur, depending on the initial conditions. Defects may even persist into the Benjamin-Feir stable range where they coexist with plane waves [56–58]. In the latter regime of *intermittent turbulence*, defects cannot indefinitely reproduce to infect the entire medium. Instead, cascades of localized defects are observed on a laminar background of plane waves, see Fig. 2.4(c).

In two space dimensions, rotating spiral waves are solutions of the CGLE. Individual spiral waves may be stable, see Fig. 2.5(a), or spiral-breakup may occur due to absolute or convective instabilities, leading to turbulence [54]. Spiral waves provide topological defects of the phase distribution field. Along any closed contour around the center of the spiral wave, the phase changes by  $\Delta\phi = \pm 2\pi$ . Therefore, the phase is not defined in the center, which

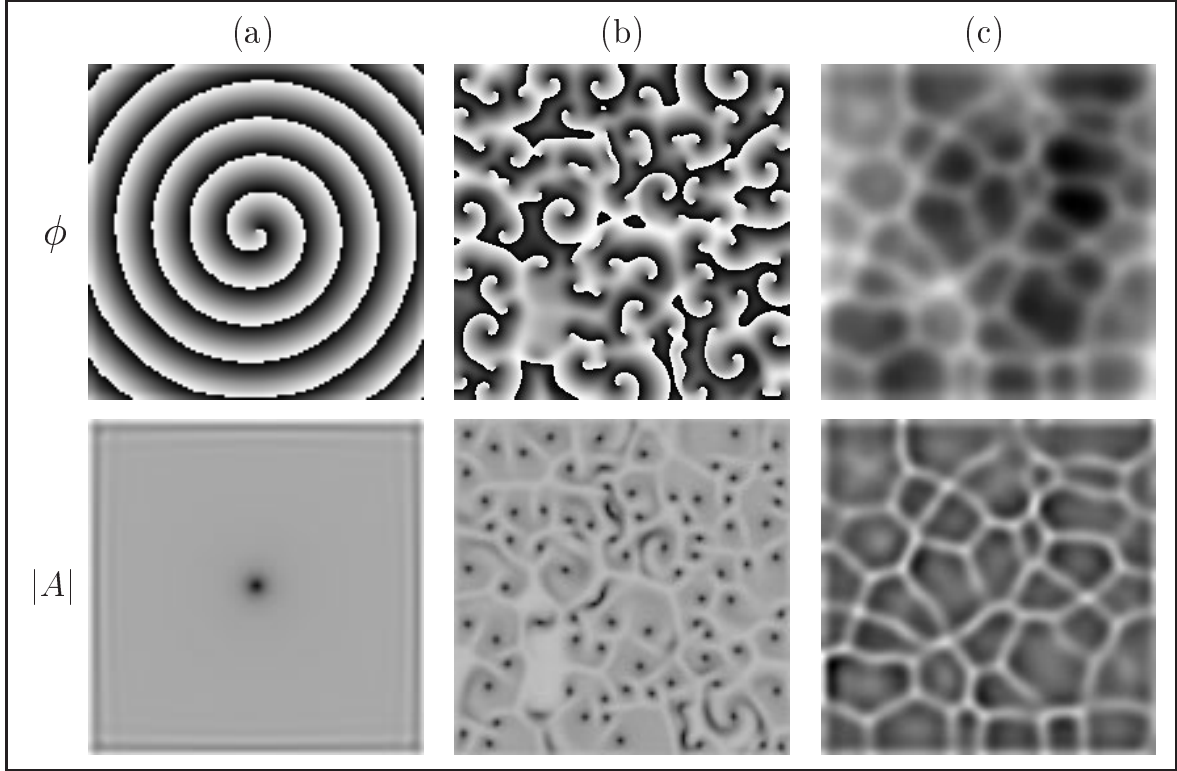


Figure 2.5: *Different patterns in the two-dimensional CGLE: (a) rotating spiral wave, (b) amplitude turbulence, and (c) phase turbulence. The variables  $\phi$  (top) and  $|A|$  (bottom) are displayed in gray scale; defects are seen in the bottom images of frames (a) and (b) as dark spots. The system size is  $L = 128$  for each pattern. The parameters are (a)  $\beta = -0.6$ ,  $\varepsilon = 2$ , (b)  $\beta = -1.8$ ,  $\varepsilon = 0$ , and (c)  $\beta = -0.752$ ,  $\varepsilon = 2$ .*

requires that the oscillation amplitude vanishes there. Simple spirals are associated with a topological charge defined as  $Q = \pm 1$ , where the sign depends on the rotation direction. The total topological charge of a medium with periodic boundary conditions is conserved, and topological defects can only be created or annihilated in pairs of opposite charge [22].

Two types of disordered regimes representing amplitude and phase turbulence can be distinguished in the two-dimensional case [59]. Amplitude turbulence, see Fig. 2.5(b), is characterized by the persistent creation and annihilation of (topological) defects. If the density of defects is large, they appear and disappear rapidly and only rarely form spirals. The statistics of defects has been investigated in Ref. [60]. In contrast, in phase turbulence no defects occur, see Fig. 2.5(c). The resulting state consists of a disordered cellular structure of shock lines, with only large-scale modulations of the phase field. Phase turbulence in two space dimensions is always metastable with respect to defect turbulence or frozen spiral regimes [54]. The latter non-chaotic state is characterized by spiral waves that occupy the individual cells of a network of shocks [59, 61]. The investigation of turbulent states and their

statistical properties in the CGLE in one, two, and three space dimensions is still an active field of research.

---

## Chapter 3

# Strategies for controlling turbulence and pattern formation

---

To control turbulence and pattern formation in extended nonequilibrium systems, different approaches have been proposed in the literature [36, 62–71]. Some of the proposed techniques require spatially resolved access to the medium under control, because the control force is applied locally or the variation of the control signal is continuous in space. In contrast, global control schemes act on a single system parameter that simultaneously affects the dynamics of the entire medium. In typical experimental situations, global methods are more practical because spatially resolved access to the system elements is often difficult, but a global system parameter (such as temperature) can be easily controlled.

In this chapter, two types of global control methods, uniform periodic forcing and global feedback, are considered. Possible effects of periodic forcing are outlined and then illustrated at two examples in Section 3.1. In Section 3.2, different schemes of global feedback are introduced and the effects of global feedback in the complex Ginzburg-Landau equation are reviewed.

### 3.1 Periodic forcing

#### 3.1.1 Resonance phenomena

Periodic forcing is abundant in nature (e.g. circadian rhythm, beating of the heart). Applied to a distributed oscillatory system, periodic forcing can lead to the formation of various complex spatiotemporal patterns. To understand the occurring phenomena, it is helpful to first consider the response of a single oscillatory element to a periodic stimulus.



Assume a nonlinear oscillator that periodically oscillates at its natural frequency  $\omega_0$ . When the system is now driven by a periodic force with frequency  $\omega_f$ , it can become entrained to the external stimulus. In such a resonant case, the forced system oscillates at a frequency  $\omega$  that is rationally related to the applied frequency  $\omega_f$ . This phenomenon is known as frequency locking [14]. Frequency locking has been observed in various nonlinear systems of physical, chemical, and biological origin [39, 72–77].

The simplest type of entrainment occurs when the forcing frequency  $\omega_f$  is sufficiently close to the natural frequency  $\omega_0$ . In this case, the system adapts its oscillation frequency to the frequency of the driving force, such that it oscillates in harmonic resonance with the stimulus. However, entrainment can also lead to locking at other frequency ratios. The  $n : m$  resonance (where  $n$  and  $m$  are integers) is defined such that the oscillator entrains at a frequency ratio  $\frac{\omega_f}{\omega} = n/m$ . For example, a system entrained in 2:1 resonance oscillates exactly once per two periods of the driving force. If  $n > m$ , the entrainment is denoted as subharmonic, and for  $n < m$  it is called superharmonic.

The frequency range for resonant locking at a given ratio  $n : m$  depends on the forcing amplitude. The frequency-amplitude plane of the driving force shows tongue-shaped entrainment bands (*Arnol'd tongues* [79]), see Fig. 3.1 for an example. At low forcing amplitudes  $\gamma$ , these resonant bands are separated by regions where the response to the periodic stimulus is quasiperiodic, i.e., in the resulting oscillations a finite number of incommensurate modes is excited. At higher forcing amplitudes, the entrainment bands overlap and various bifurcations can occur, leading to period doubling and temporal chaos. The entrainment of

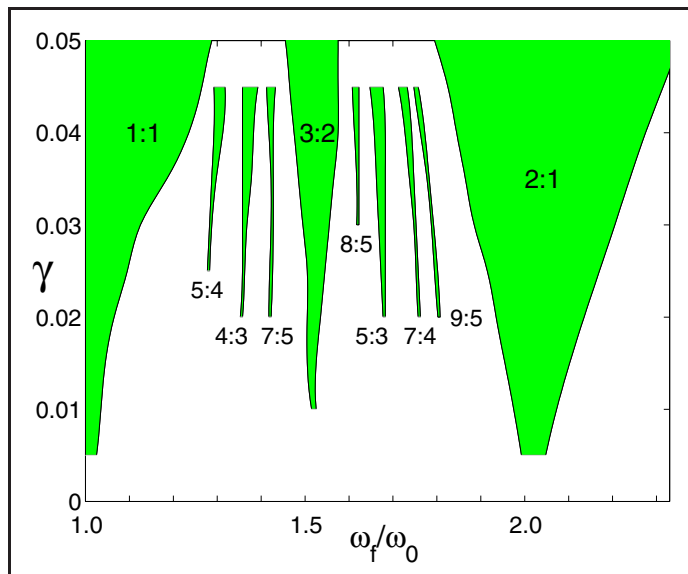


Figure 3.1: *Frequency locked regions in a periodically forced two-variable model of a nonlinear chemical oscillator, the parametrically forced Brusselator model (see the next section). Shaded regions show frequency locked behavior, where the system is entrained with the indicated ratios. Outside the resonant bands, the system response is quasiperiodic or locked with higher ratios. From Ref. [78].*



single oscillatory elements has been studied extensively and is well understood (see, e.g., Ref. [80]).

Much less is known on frequency locking in spatially extended systems. The response of a distributed oscillatory system to a periodic stimulus is more complicated than that of a single oscillator since it is possible for individual elements to oscillate with different magnitude and phase with respect to each other. Moreover, the ability of individual oscillatory elements to entrain to a periodic stimulus may change through the influence of diffusive coupling. For example, the dominating contribution of the diffusion terms can prevent frequency locking at small forcing amplitudes [35, 81]. On the other hand, close to the boundaries of Arnol'd tongues stable frequency locked patterns may exist at forcing parameters where single oscillatory elements are not locked [35]. Thus, depending on the parameter values, diffusion may either enhance or suppress frequency locking.

So far, most of the theoretical studies [32–35, 62, 82–84] on resonant pattern formation in reaction-diffusion systems have concentrated on the forced complex Ginzburg-Landau equation [85, 86], which is the normal form of such a forced system near the soft onset of oscillations. In presence of periodic forcing with frequency  $\omega_f = \frac{n}{m}(\omega_0 - \nu)$ , where  $n/m$  is an irreducible integer fraction and  $\nu$  denotes the detuning of the forcing frequency from exact resonance, the CGLE becomes

$$\frac{\partial A}{\partial t} = (\mu + i\nu)A - (1 + i\beta)|A|^2A + (1 + i\epsilon)\nabla^2 A + \gamma_n \tilde{A}^{n-1}. \quad (3.1)$$

Here, the parameter  $\mu > 0$  represents the distance from the Hopf bifurcation,  $\gamma_n$  is the forcing amplitude, and  $\tilde{A}$  denotes the complex conjugate of  $A$ . Note that equation (3.1) is independent of  $m$ . The resonance is specified only by the parameter  $n$ .

The stationary solutions of equation (3.1) mean frequency locking. Without the diffusion term, linear stability analysis of the stationary state yields the Arnol'd tongue of a single oscillator. In each resonance, frequency locking of a single oscillator is found in a V-shaped region in the plane spanned by the forcing parameters  $\nu$  and  $\gamma_n$  [35].

There are  $n$  equivalent stable stationary solutions for  $n : m$  resonances, which differ only by a phase shift of  $2\pi/n$  [62]. In spatially extended systems, each individual oscillatory element may lock to one of these  $n$  different states. If diffusive coupling synchronizes spatial domains of oscillators, phase patterns consisting of different domains that belong to the  $n$  different phase values can occur. The phase domains are then separated by fronts that shift the oscillation phase from one domain to another. Typically,  $2\pi/n$  phase fronts are stationary

in the case  $n = 2$  and travel in the cases  $n = 3, 4$ , thereby forming  $n$ -armed spiral patterns in two space dimensions [35, 62]. Domain patterns are also referred to as  $n$ -phase clusters [42].

Starting from strong resonance, the phase fronts can undergo a variety of bifurcations as the forcing parameters are varied. In particular, instabilities leading to motion of  $\pi$ -fronts and to the formation of labyrinthine patterns have been reported in the case  $n = 2$  [32, 87] (such instabilities are illustrated in the next section). Another bifurcation causes a transition from rotating four-phase patterns to standing two-phase patterns in the 4:1 resonance [33, 83, 88]. Similar phenomena have been found also in the  $2k:1$ ,  $k > 2$  entrainment bands [33, 83]. Other interesting effects arise due to competition between the diffusion-induced phase instability and periodic forcing. Such phenomena include the development of stripe patterns and hexagonal structures [32], and the spontaneous formation of phase kinks [34] in the case  $n = 1$ .

In addition to the amplitude equation, also other reaction-diffusion models are useful to study the effects of periodic forcing on pattern formation. Kinetic models such as the Brusselator, Oregonator, or FitzHugh-Nagumo model allow a numerical investigation of the resulting behavior farther away from the onset of oscillations [40, 78, 84, 88]. In such models, the forcing is introduced as a periodic modulation of an otherwise constant parameter. Some of the occurring phenomena are illustrated in the next section at the example of the forced Brusselator reaction-diffusion model [78].

Experimental studies of resonant pattern formation in oscillatory reaction-diffusion systems have been conducted only recently and almost exclusively focused on the periodically forced Belousov-Zhabotinsky (BZ) reaction [39, 40, 42, 88]. So far, all experiments were performed in a non-chaotic parameter regime where stable spiral waves were present in absence of forcing. Such experiments revealed a variety of resonant spatiotemporal patterns, depending on the forcing parameters. Some experimentally observed phenomena are also further described below.

The response of excitable media to a periodic stimulus has been studied in related works [89–92]. It was found that the motion of spiral waves can be effectively controlled, and a variety of resonant spiral tip trajectories has been reported. In subexcitable media, sustained wave propagation could be achieved due to the effects of periodic forcing [93].

### 3.1.2 Examples of pattern formation under periodic forcing

In order to illustrate some possible resonant phenomena, effects of periodic forcing on two oscillatory reaction-diffusion systems, the Brusselator model and the Belousov-Zhabotinsky reaction, are briefly exemplified below.

#### Brusselator model with periodic forcing

First the periodically forced Brusselator reaction-diffusion model is considered. The results of this study have been presented in detail in Refs. [40, 78, 88]. The Brusselator [12, 94] is a hypothetical scheme of chemical reactions from which a simple set of reaction-diffusion equations can be derived. The model describes the kinetics of two chemical species  $u$  and  $v$ . By adding a parametric forcing term  $\gamma \sin(\omega_f t) u^2 v$ , the model reads

$$\frac{\partial u}{\partial t} = A - (B + 1)u + u^2 v [1 + \gamma \sin(\omega_f t)] + \nabla^2 u, \quad (3.2)$$

$$\frac{\partial v}{\partial t} = Bu - u^2 v + \delta \nabla^2 v. \quad (3.3)$$

Here  $A = 0.5$  and  $B = 1.5$  are constant parameters,  $\delta = 5.0$  denotes the ratio of the diffusion coefficients of species  $u$  and  $v$ , the parameter  $\gamma$  specifies the forcing amplitude, and  $\omega_f$  is the forcing frequency. At the above specified parameters, unforced isolated system elements perform non-harmonic limit cycle oscillations. For appropriate initial conditions, rotating spiral waves are stable solutions of the reaction-diffusion equations.

Pattern formation in model (3.2)-(3.3) has been studied numerically in two space dimensions using a partial differential equation solver [95]. Here the attention is focused on the 2:1 locked band. Typical examples of patterns observed near and inside this resonance are displayed in Fig. 3.2. Outside the frequency locked regions, unlocked spiral waves with underlying quasiperiodic oscillations are present, see Fig. 3.2(a) for a typical example. Domain patterns with anti-phase oscillations prevail in the center of the 2:1 locked band, see Fig. 3.2(b).

Below a critical forcing amplitude  $\gamma_c \approx 0.007$  and near the high-frequency edge of the 2:1 resonance, the fronts in the phase domain patterns undergo an instability. This so-called nonequilibrium Ising-Bloch (NIB) bifurcation causes a transition from standing to traveling two-phase patterns. The NIB bifurcation has been analyzed previously by Coulet *et. al.* in the framework of the forced CGLE [32, 62]. Through the front bifurcation a stationary (Ising) phase front loses stability to a pair of counter-propagating (Bloch) fronts. While Bloch fronts

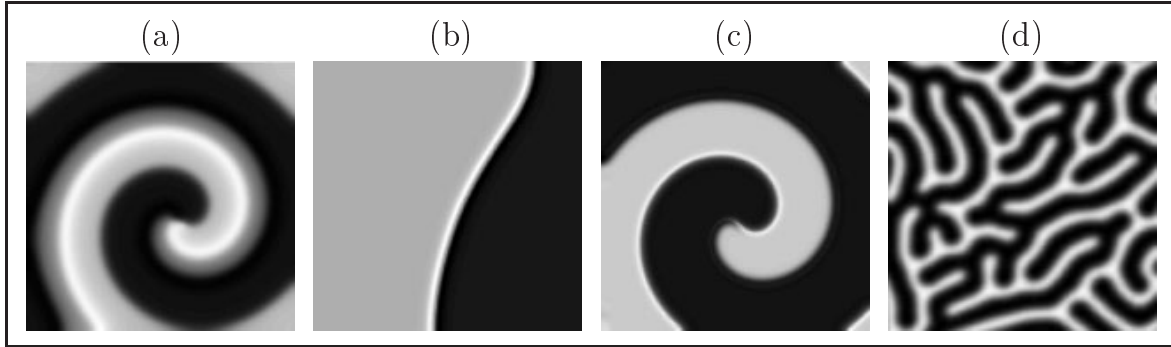


Figure 3.2: Patterns in the forced Brusselator model in the vicinity and within the 2:1 sub-harmonic entrainment band. The images display snapshots of the spatial distribution of concentration  $u$ : (a) unlocked spiral wave, (b) frequency locked standing two-phase pattern, (c) locked rotating two-phase spiral, and (d) locked labyrinthine pattern. The values of the forcing parameters  $\omega_f/\omega_0$  and  $\gamma$  are, respectively, (a) 1.58, 0.05; (b) 1.66, 0.07; (c) 2.12, 0.05; and (d) 2.40, 0.06. From Ref. [78].

continuously shift the oscillation phase from one spatial domain to the other, along an Ising front the phase is constant except in the front center. At that point there is an oscillation node where the oscillation amplitude vanishes and the phase undergoes a jump of  $\pi$ . The NIB instability is also observed later in simulations of catalytic CO oxidation under global delayed feedback.

As a consequence of counter-propagating fronts, rotating two-phase spiral patterns can arise in two space dimensions, see Fig. 3.2(c). Such patterns develop due to the following mechanism: assume a continuous, initially straight phase front consisting of an upper and a lower part that travel in opposite directions. For continuity reasons, there exists a kink at the boundary between the two front parts which does not move. During the further evolution, the front will curl in the vicinity of the kink, thereby forming a two-phase spiral that rotates with constant angular velocity. Such a pattern can also develop from less special initial conditions, provided that a kink is present.

A different, transverse front instability leads to the formation of labyrinthine patterns in the 2:1 resonance of the Brusselator model, see Fig. 3.2(d) for a fully developed example. The growth mechanism of the labyrinthine patterns is as follows: starting with an initially planar phase front with superimposed noise, lateral perturbations along the front grow in time and evolve into fingers. Evolving fingers repel each other if they come too close. They also can undergo tip-splitting, thereby creating further branches. The growth of such objects is not saturated until finally the full system is covered by a standing labyrinthine structure.

### Belousov-Zhabotinsky reaction with periodic forcing

A rich variety of resonant spatiotemporal patterns has been also found in laboratory experiments using the Belousov-Zhabotinsky (BZ) reaction [39, 40, 42, 88]. To provide an experimental example of possible resonance phenomena and to introduce a method for pattern characterization, the results of a study by Lin *et al.* [40] are summarized below.

The BZ reaction consists of the oxidation of malonic acid by bromate, catalyzed by metal ions in acidic aqueous solution. The reaction is known to exhibit oscillatory behavior for a wide range of control parameters when maintained in a nonequilibrium state [8, 19]. The experiments described in Ref. [40] have used a light-sensitive ruthenium-catalyzed version of the BZ reaction, where forcing can be externally applied as spatially uniform, time-periodic light pulses. The reaction proceeds in a thin porous membrane (0.4 mm thick, 22 mm in diameter) sandwiched between two continuously refreshed reservoirs of reagents. Quasi-two-dimensional patterns in the spatial distribution of the ruthenium catalyst Ru(II) are imaged by measuring the light transmission through the membrane.

When periodic light pulses with intensity  $\gamma^2$  and frequency  $f$  are applied, several resonances (1:1, 2:1, 3:1, 3:2, 4:1) occur. The most complex behavior is found in the subharmonic resonance with 2:1 frequency ratio and includes various qualitatively different types of patterns, see Fig. 3.3. In the top row of Fig. 3.3, snapshots of reactor images are displayed. To detect resonance in the experimental data, the temporal response of each resolving pixel of a pattern forced with frequency  $f$  was determined. To do this, the fast Fourier transform (FFT) was calculated for the time series of each pixel. In a 2:1 resonant case the average power spectrum over all pixels exhibits a dominant peak at  $f/2$ .

To extract information on the local oscillation magnitude and phase in a pattern, for each pixel the complex Fourier coefficient  $a$  that corresponds to the  $f/2$  mode was then plotted into the complex plane. The resulting *phase portraits* are shown in the middle row of Fig. 3.3. Each point in the phase portraits corresponds to a pixel in the patterns. The oscillation magnitude  $|a|$  of the considered mode for each point in the complex plane corresponds to its distance to the plane origin, and the phase  $\arg(a)$  is given by the polar angle. Hence, phase portraits allow to simultaneously image the amplitudes and phases of all oscillating elements at the expense of information on their spatial arrangement. Finally, the bottom row of Fig. 3.3 displays a histogram of the distribution of phase angles for each pattern.

The unforced BZ system exhibits stable rotating spiral waves, see Fig. 3.3(a). The circular distribution of points in the corresponding phase portrait and the phase histogram show

that the phase angles are uniformly distributed in the interval  $[0, 2\pi]$ . When strong forcing is introduced, frequency locked patterns as shown in Figs. 3.3(f) (labyrinthine patterns) and 3.3(g) (Ising front patterns) form. Both pattern types show a sharp distribution of phase angles. They consist of stationary spatial domains with synchronous oscillations that are phase shifted by  $\pi$ . In contrast, the gradient of phase angles in the frequency locked pattern in Fig. 3.3(b) is so small that there are no distinguishable phase fronts. In the 2:1 resonant patterns shown in Figs. 3.3(c)-3.3(e) the oscillation phase is moderately weighted. The Fourier coefficients in the complex plane show a rough S-shaped distribution. It can be seen more clearly in the bottom row of Fig. 3.3 that for each resonant pattern the phase angle distribution is weighted differently around two  $\pi$ -shifted phases, depending on the forcing parameters.

The above described experiments [40] demonstrate that pattern formation in the BZ reaction can be efficiently manipulated by means of external forcing. Using a similar setup of the light-sensitive BZ reaction, in a subsequent study Vanag *et al.* [42] could reproduce some of the observed patterns and additionally found further types of cluster patterns. Other studies

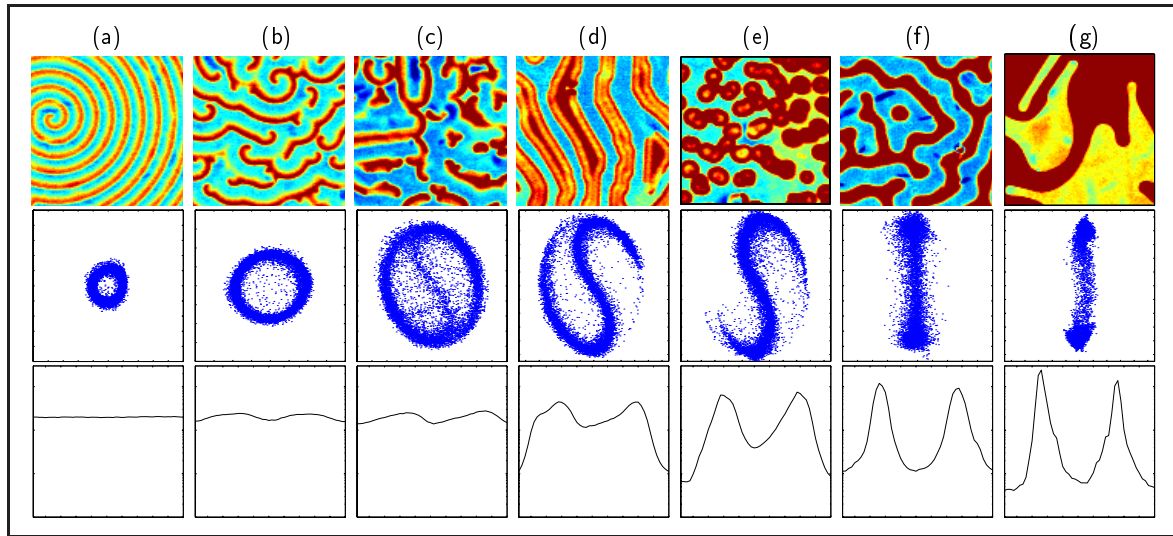


Figure 3.3: (top row) Typical reactor images ( $9 \times 9 \text{ mm}^2$ ) of different patterns observed in the Belousov-Zhabotinsky reaction: (a) unforced rotating spiral wave, (b) rotating spiral wave fragments, (c) mixed rotating spiral and standing wave pattern, (d)-(g) qualitatively different standing wave patterns. Patterns (b)-(g) exhibit a 2:1 resonance in the average temporal power spectrum of the pattern. (middle row) The complex Fourier amplitudes  $a$  after frequency demodulation at  $f/2$  for all pixels in each pattern: the abscissa is  $\text{Re}(a)$ ; the ordinate is  $\text{Im}(a)$ . (bottom row) Histograms of phase angles for all the pixels in each image; the abscissa range is  $[0, 2\pi]$  and the ordinate range is arbitrary. For each pattern the parameter values of  $f(\text{Hz})$  and  $\gamma^2(\text{W/m}^2)$  are, respectively, (a) 0, 0; (b) 0.1000, 119; (c) 0.0625, 214; (d) 0.0556, 248; (e) 0.0417, 358; (f) 0.0455, 386; (g) 0.0385, 412. The figure was taken from Ref. [40].



of the forced BZ reaction have also reported resonant patterns locked at different frequency ratios [39, 88].

## 3.2 Global feedback

### 3.2.1 Overview of feedback schemes

Feedback techniques differ from periodic forcing by the fact that the control signal is not fixed *a priori*, but an acting force is generated by the system itself. Feedback techniques were originally designed for the control of chaos in dynamical systems with only a few degrees of freedom [96–99], but were later extended for the application to high-dimensional systems governed by partial differential equations [36, 63–71].

In global feedback methods, information continuously gathered from all system elements is summed up and used to generate a control signal which acts back on a common parameter that affects the dynamics of the entire medium. Such a feedback loop can be easily implemented into many experimental systems, and does not require the knowledge of the governing equations. The action of global feedbacks on chaotic extended systems has been recently investigated experimentally for arrays of electrochemical oscillators [100], and theoretically for semiconductors [38] and surface chemical reactions [101, 102]; effects of global feedback also have been discussed in the general context of the complex Ginzburg-Landau equation [36, 37]. Furthermore, various forms of global feedback have been successfully applied to control pattern formation in non-chaotic oscillatory [41, 103, 104] and excitable [105–109] chemical systems.

A feedback method useful to control chaotic oscillatory dynamics has been developed by Pyragas [97]. This method of *time-delay autosynchronization* (TDAS) is based on a comparison between present and past system states. The global variant of this method, designed to control turbulence in spatially extended systems, is implemented via continuous application of a global control signal of the form

$$F(t) = K [\bar{u}(t) - \bar{u}(t - \tau)], \quad (3.4)$$

where  $\bar{u}(t) = \frac{1}{S} \int_S u(x, t) dx$  denotes the spatial average of a system variable  $u$  at time  $t$ , and the parameters  $K$  and  $\tau$  specify feedback intensity and delay time, respectively. When acting back on the variable  $u$ , in the limit  $\tau \rightarrow 0$  such feedback aims to stabilize uniform steady state solutions of the system. In the limit  $\tau \rightarrow T_{\text{UPO}}$ , the goal of feedback application is to stabilize an otherwise unstable periodic orbit (UPO) with period  $T_{\text{UPO}}$ . In case of successful

stabilization, the control signal has to compensate only for small fluctuations and practically vanishes.

As a natural extension of the method described by equation (3.4), not only one but several past global system states  $\bar{u}(t - m\tau)$  can be considered [99], yielding the global *extended time-delay autosynchronization* (ETDAS) scheme

$$F(t) = K [\bar{u}(t) - (1 - R) \sum_{m=1}^{\infty} R^{m-1} \bar{u}(t - m\tau)], \quad 0 \leq R < 1, \quad (3.5)$$

where the parameter  $R$  controls the contributions of previous states. The simple TDAS scheme is recovered in the case  $R=0$ . It is known that ETDAS is capable of stabilizing unstable periodic orbits that cannot be stabilized using the TDAS method [110, 111]. Using the global ETDAS scheme (3.5) successful control of chaotic spatiotemporal dynamics in a reaction-diffusion model describing charge transport in a semiconductor has been demonstrated by Franceschini *et al.* [38]. Other studies briefly exemplified the effects of global autosynchronization methods in a surface chemical reaction [101, 102].

A different form of global feedback useful both for the effective synchronization of spatiotemporally chaotic states and for the generation of new spatiotemporal patterns in oscillatory systems has been proposed by Battogtokh and Mikhailov [36]. In this method the forcing signal is directly proportional to the difference of a past global system state and a reference state,

$$F(t) = K [\bar{u}(t - \tau) - u^*], \quad (3.6)$$

where  $u^*$  denotes the steady state value of the variable  $u$ , and  $K$  and  $\tau$  again specify feedback intensity and delay time, respectively. Henceforth, this method is referred to as *global delayed feedback*. The control force  $F(t)$  may be applied to the evolution equation of *any* system variable (or even to all of them). Also control forces collectively generated by several system variables may be considered. The delay can be used to modify the phase relation between the control signal and the oscillating pattern. Related research [36, 37, 112–114] so far has been focused on a normal form approach valid close to the soft onset of oscillations. These previous studies provide a basis for the interpretation of the results obtained in the present work and so are discussed in more detail below.



### 3.2.2 Complex Ginzburg-Landau equation with global feedback

In this section results of previous investigations by Battogtokh and Mikhailov [36, 37] are reviewed. They studied the normal form of a reaction-diffusion system close to a supercritical Hopf bifurcation and in presence of a global feedback of the form (3.6). The considered system is the complex Ginzburg-Landau equation (CGLE) (cf. Section 2.3) supplemented by an additive force  $\mu e^{i\chi}\bar{A}$ ,

$$\frac{\partial A}{\partial t} = A - (1 + i\beta)|A|^2 A + (1 + i\varepsilon)\nabla^2 A + \mu e^{i\chi}\bar{A}, \quad (3.7)$$

where  $\bar{A}(t) = \frac{1}{S} \int_S A(x, t) dx$  is the spatial average of the complex oscillation amplitude,  $\mu$  represents the feedback intensity, and  $\chi$  characterizes an effective phase shift between the global amplitude and the control force. In the derivation of equation (3.7) the assumption has been made that the time delay is short as compared to the characteristic evolution times of the complex amplitude  $A(x, t)$ . When this condition is fulfilled, the only (but important) effect of the delay  $\tau$  is that it controls the effective phase shift  $\chi = \chi_0 + \omega\tau$ , where  $\chi_0$  is a constant and  $\omega$  denotes the linear oscillation frequency of individual oscillators.

The global feedback in equation (3.7) modifies the frequency and the amplitude of uniform oscillations. By substituting  $A(x, t) = \rho e^{-i\Omega t}$  one finds that in presence of global feedback uniform oscillations have the frequency

$$\Omega = -\beta - \mu(\sin\chi - \beta\cos\chi),$$

and the modulus of the complex amplitude for uniform oscillations is

$$\rho = (1 + \mu\cos\chi)^{1/2}.$$

These corrections are small when the feedback intensity  $\mu$  is low.

The linear stability of uniform oscillations is investigated by considering the evolution of small perturbations. Small homogeneous perturbations always decay. Linear stability analysis of *inhomogeneous* perturbations  $\delta A \sim e^{(ikx - \Omega t) + \gamma_k t}$ , where  $k \neq 0$ , leads to an equation for the increment of growth  $\gamma_k$  of the mode with wavenumber  $k$ . This equation has two solutions  $(\gamma_k)_{1,2}$ . Depending on the parameters of equation (3.7) and the wavenumber  $k$ , these solutions are either real or complex conjugated. Instability of uniform oscillations occurs when the real part of at least one solution changes its sign and becomes positive.

The stability diagram of uniform oscillations is shown in Fig. 3.4. For this diagram the parameters ( $\varepsilon = 2$ ,  $\beta = -1.4$ ) have been chosen deep in the Benjamin-Feir unstable regime

(cf. Section 2.3). Hence, uniform oscillations are unstable in absence of feedback ( $\mu = 0$ ) and the final state reached in numerical simulations of equation (3.7) is characterized by developed defect turbulence. However, the action of sufficiently strong global delayed feedback allows to stabilize uniform oscillations within certain intervals of the phase shift  $\chi$ . In presence of feedback, uniform oscillations are stable with respect to small perturbations above the boundary shown by the solid curve.

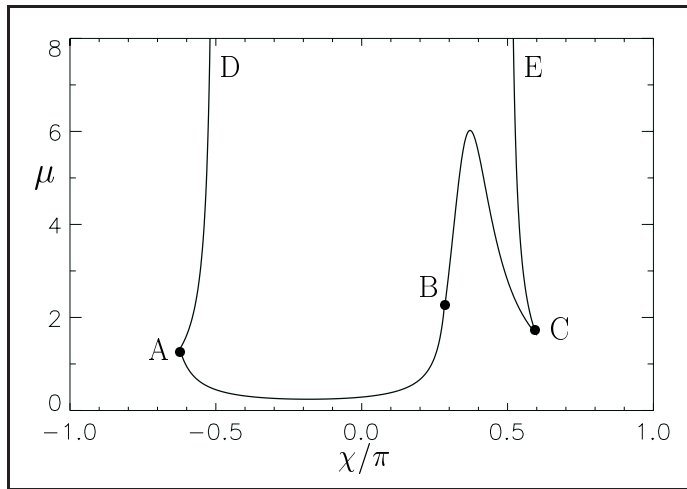


Figure 3.4: *Stability diagram of uniform oscillations in the CGLE with global feedback ( $\epsilon=2$ ,  $\beta=-1.4$ ). Uniform oscillations are stable inside the region bounded by the solid line. Characteristic points on this curve correspond to the values of the phase shift  $\chi_- = 0.6235\pi$  (point A),  $\chi^* = 0.275\pi$  (B), and  $\chi_+ = 0.599\pi$  (C). The figure was reproduced after Ref. [37].*

Depending on where the solid line in Fig. 3.4 is crossed, the instability of uniform oscillations leads to the occurrence of different types of spatiotemporal patterns. First, the system behavior is discussed when the solutions  $(\gamma_k)_{1,2}$  are both real. When the curve AB is crossed, standing waves (periodic spatial modulations superimposed on the state of uniform oscillations) with wavenumber  $k \neq 0$  appear. Their wavelength  $\lambda = 2\pi/k$  strongly depends on the phase shift and diverges as the point B is approached. When the curve BC is crossed, large-scale domain structures develop, with the characteristic size of domains comparable to the size of the medium. In this case, the most unstable mode is encountered in the limit  $k \rightarrow 0$  (in finite systems, this limit is understood in the sense that the minimal possible wavenumber, given by the size of the medium and the boundary conditions, is considered).

When the solutions  $(\gamma_k)_{1,2}$  are complex conjugated, long-wavelength oscillatory perturbations start to grow when uniform oscillations become unstable. This scenario, which in numerical simulations leads to turbulent behavior, is encountered when crossing the curves DA or CE. Again, the least stable mode is the one with  $k \rightarrow 0$ . In contrast to the previously considered cases, this instability develops under *increase* of the feedback intensity beyond

the critical value

$$\mu_c = -\frac{1}{2\cos\chi}.$$

Hence, the instability can occur only if  $\cos\chi < 0$ . Note that the critical value for the feedback intensity does not depend on the parameters  $\epsilon$  and  $\beta$ .

Typical two-dimensional structures that result from numerical simulations of equation (3.7) upon variation of the feedback parameters  $\mu$  and  $\chi$  are displayed in Fig. 3.5. Suppression of defect turbulence by gradually increasing global feedback is achieved by different scenarios, depending on the phase shift  $\chi$ . Synchronous oscillations emerge through appearance of a cellular structure [Fig. 3.5(b)], through the regime of intermittent turbulence [Fig. 3.5(c)], or through the formation of large phase domains [Fig. 3.5(d)].

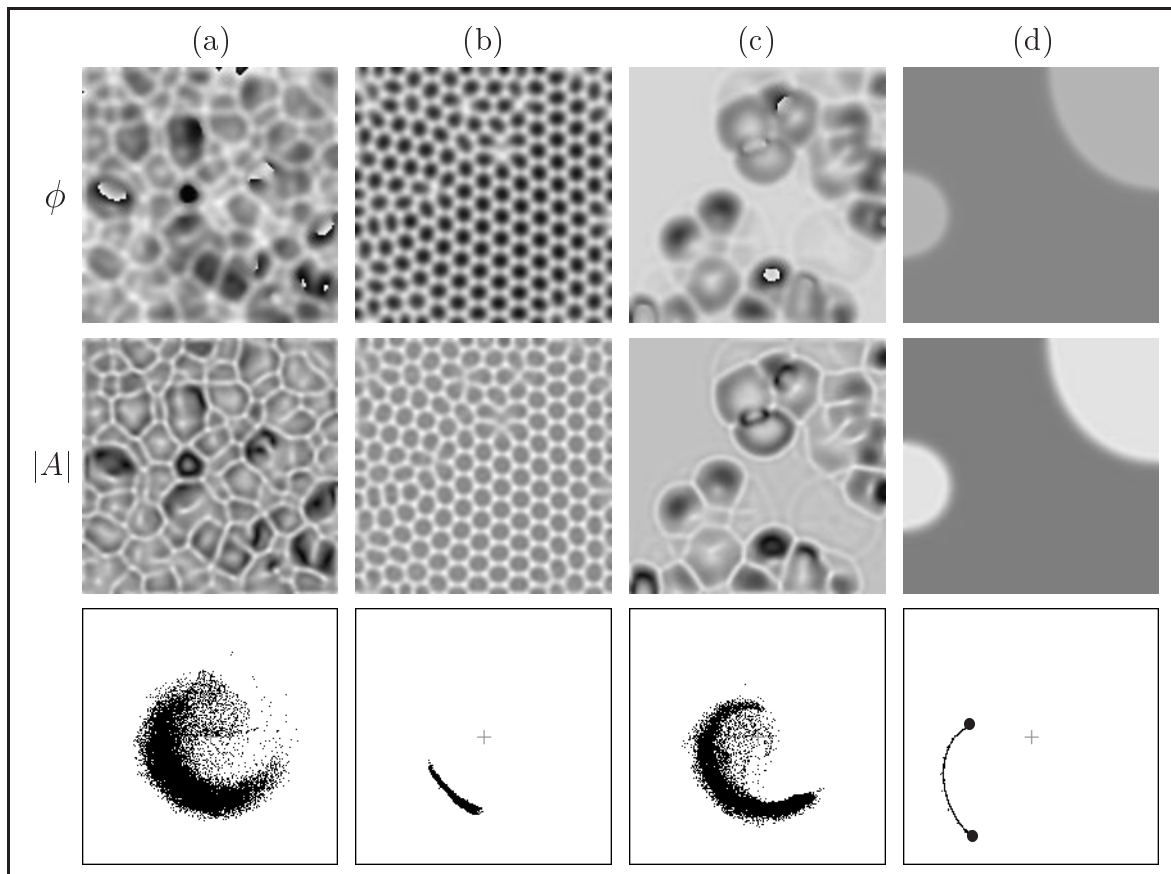


Figure 3.5: Different two-dimensional patterns in the CGLE with global feedback ( $\epsilon=2$ ,  $\beta=-1.4$ ). For each pattern the distributions of phase (top row), amplitude modulus (middle row), and the phase portraits (bottom row) are displayed. Defects appear dark in the amplitude images. The parameters of  $\mu$  and  $\chi$  are, respectively: (a) 0.18, -0.2; (b) 0.26, -0.2; (c) 0.55, 0; and (d) 4.0, 0.4.

In all three cases fully developed defect turbulence is first replaced by turbulence on the background of a cellular structure [Fig. 3.5(a)] when gradually increasing the feedback intensity from  $\mu = 0$ . Cellular structures initially consist of an irregular, mobile network of cells which are populated by amplitude defects. The boundaries of the cells are formed by regions with an increased modulus of the oscillation amplitude (shocks). When  $\mu$  is further increased, the cells become less mobile and arrange into more regular structures. Occasionally, defects inside some cells disappear, thereby producing empty inactive cells, or defects destroy a cell boundary and penetrate into neighboring cells. Upon increase of the feedback intensity, the number of defects decreases and they gradually lose their ability to destroy the cell boundaries.

In the first scenario, the global feedback eventually completely eliminates the defects when  $\mu$  is further increased, and an ordered pattern of hexagonal cells forms after a slow relaxation process, see Fig. 3.5(b). Such structures are formed by triplets of standing wave modes, whose wave vectors satisfy the conditions  $\mathbf{k}_1 + \mathbf{k}_2 + \mathbf{k}_3 = 0$  and  $|\mathbf{k}_1| = |\mathbf{k}_2| = |\mathbf{k}_3|$ . The growth of these modes is saturated by nonlinear effects and thus a steady hexagonal cellular structure is formed. As can be deduced from the phase portrait in Fig. 3.5(b), the hexagonal network represents a comparatively small spatial modulation of a uniformly oscillating state. At still higher values of  $\mu$ , the cell boundaries are gradually washed out until uniform oscillations are established. Due to hysteresis effects, the transition to the uniform state occurs at a higher feedback intensity than indicated by the solid line in Fig. 3.4.

The second scenario takes place at higher values of the phase shift  $\chi$ . Empty cellular structures which form the background dissolve now before the disappearance of cells that are occupied by defects. As a result, the infected cells form clusters or islands on the background of uniform oscillations, see Fig. 3.5(c). Size and shape of such turbulent bubbles vary in time, and they can move through the medium. The turbulent islands shrink as the feedback intensity is further increased, until all of them finally die out and the system is found in the state of synchronous oscillations. In comparison to the first scenario, a higher feedback intensity is needed here to establish uniform oscillations.

The third scenario is observed when the phase shift  $\chi$  is chosen such that by increasing  $\mu$ , the line BC in Fig. 3.4 is crossed. The initial stage of pattern evolution is similar to the previously described case, where empty cells dissolve and turbulent islands are surrounded by uniform oscillations. Upon further increase of global feedback, however, the cell boundaries inside the islands disappear and large, almost uniform domains are formed. At still higher feedback intensities, such domains shrink and finally disappear.

When fixing the feedback intensity in the regime of large-scale domains, they slowly rearrange their initially complex shape, tending to minimize the curvature of their border lines. An example of this later stage is displayed in Fig. 3.5(d). Now the domains consist of completely synchronous oscillations which differ from the background both by their oscillation phase and amplitude, but have the same frequency. Henceforth, such structures are referred to as *amplitude clusters*. The two clusters – one representing the background, the other the domains – are indicated in the phase portrait in Fig. 3.5(d) by the enlarged dots; the points distributed on the curved line correspond to pixels in the domain borders.

In summary, it has been found in Refs. [36, 37] that global delayed feedback essentially influences the properties of developed turbulence in the CGLE and leads to the appearance of complex patterns. Inside a synchronization window a sufficiently strong feedback suppresses turbulence and establishes uniform oscillations. Synchronization develops according to three different scenarios, i.e. via formation of hexagonal cellular structures, via localized turbulence on the background of uniform oscillations, and via formation of amplitude clusters.

It should be noted that global delayed feedback can also be efficiently used to modify pattern formation in the CGLE in the Benjamin-Feir stable regime. For an appropriate choice of the phase shift this kind of feedback has a desynchronizing effect and induces the breakdown of global oscillations [112]. Moreover, global feedback in the Benjamin-Feir stable regime allows suppression of spiral waves [37], and can induce phase flips, standing waves, and amplitude clusters [112, 114].



---

## Chapter 4

### Catalytic CO oxidation on platinum (110)

---

In this chapter, the oxidation of carbon monoxide on a platinum (110) single crystal surface is introduced. Spatiotemporal pattern formation in this heterogeneous catalytic reaction is further investigated theoretically and experimentally in the later parts of this work, where the control strategies described in Chapter 3 are applied.

Section 4.1 starts with a brief phenomenological overview of CO oxidation on platinum single crystal surfaces. The mechanism of the reaction on Pt(110) is described in Section 4.2. Finally, mathematical modeling of this reaction is discussed in Section 4.3.

#### 4.1 Phenomenological overview

Oscillatory kinetics in heterogeneous catalysis was first observed in the early seventies by the group of E. Wicke, who discovered oscillations of the reaction rate in catalytic oxidation of carbon monoxide [115, 116]. Since then, oscillatory surface reactions have developed into a very active field of research, the catalytic CO oxidation on platinum surfaces being the most extensively studied example (see Ref. [43] for a review).

To explain the origin of kinetic instabilities, experiments with single crystal surfaces were started (see Ref. [117]). Such experiments typically were carried out under low pressure conditions ( $p < 10^{-3}$  mbar), where the reaction proceeds in an isothermal way due to low total reaction rates and high thermal conductivity of the crystal. On single crystal surfaces, oscillatory kinetics was first observed in 1982 by Ertl *et al.* [44] in CO oxidation on Pt(100). In 1986, oscillations were also reported on Pt(110) [118], where they showed rich behavior, ranging from periodic and mixed-mode oscillations to deterministic chaos [119]. Furthermore, upon application of periodic forcing, resonance phenomena were observed [75, 120].



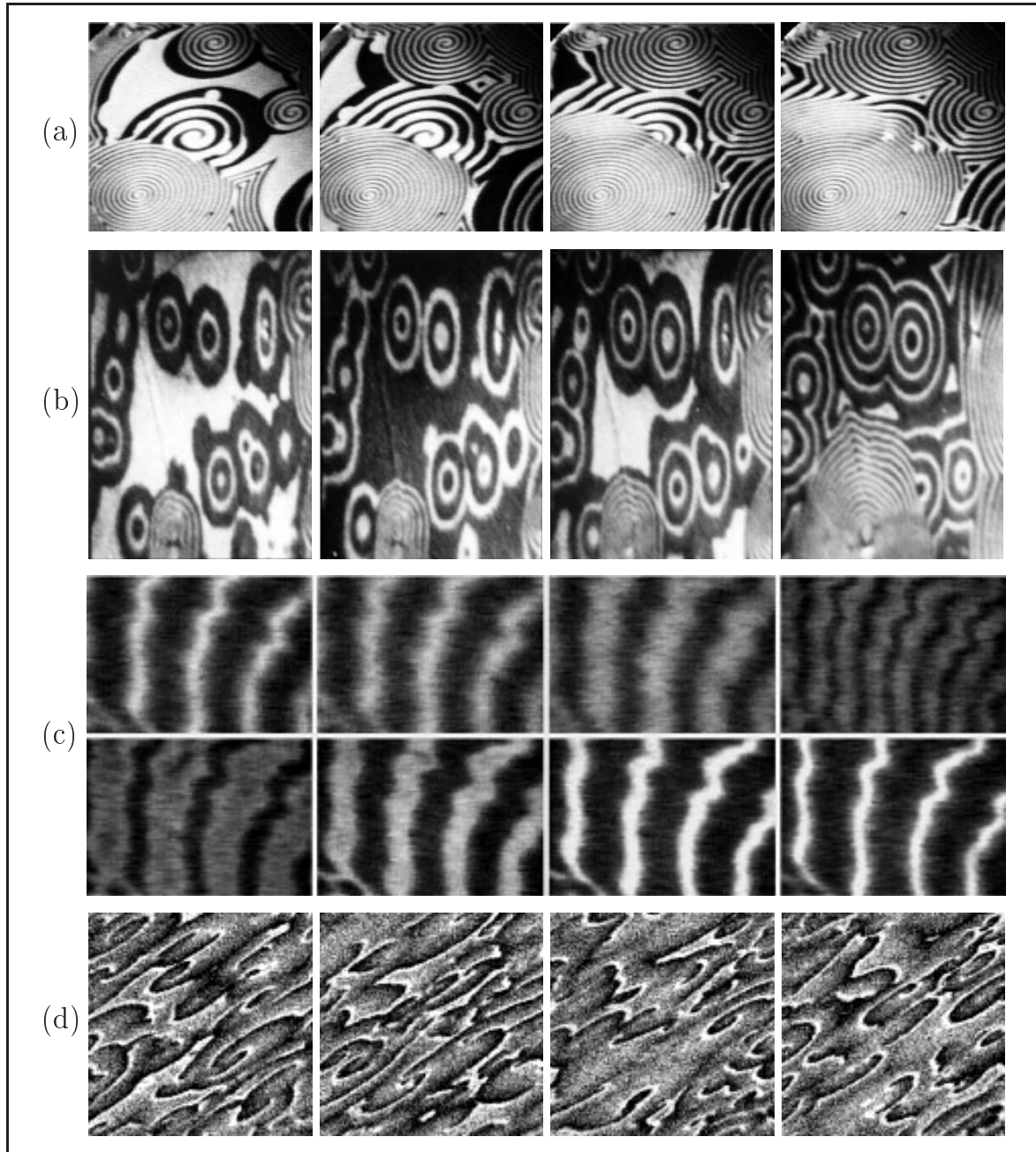


Figure 4.1: Snapshots of PEEM images displaying different patterns in CO oxidation on Pt(110). Dark areas in the images correspond to predominantly oxygen covered regions, and bright areas indicate mainly CO covered regions. (a) Rotating spiral waves (from Ref. [121]). The different spatial wavelengths of spirals are due to the existence of surface defects to which some of the spirals are pinned. (b) Target patterns [46], (c) standing waves [122], and (d) chemical turbulence (temperature  $T = 536$  K, CO partial pressure  $p_{\text{CO}} = 6.4 \times 10^{-5}$  mbar, oxygen partial pressure  $p_{\text{O}_2} = 20.0 \times 10^{-5}$  mbar). The size of individual frames is (a)  $400 \times 400 \mu\text{m}^2$ , (b)  $200 \times 300 \mu\text{m}^2$ , (c)  $300 \times 200 \mu\text{m}^2$ , and (d)  $360 \times 360 \mu\text{m}^2$ .

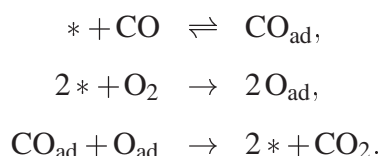


The development of spatially resolving techniques such as photoemission electron microscopy (PEEM) [123, 124] has shifted the focus from purely temporal phenomena to spatiotemporal pattern formation. Measurements employing PEEM allow to display the local work function, which is changed by the adsorbates, across a surface area of about  $500\mu\text{m}$  in diameter. The evolution of patterns on the catalytic surface can be followed in real time with a spatial resolution of about  $0.2\mu\text{m}$ . Among surface chemical reactions, by far the richest variety of spatiotemporal patterns has been found in CO oxidation on Pt(110). The observed phenomena include rotating spiral waves, target patterns, standing waves, cellular structures, chemical turbulence, and solitary waves [45, 46, 121, 125, 126]. Examples of such patterns are displayed in Fig. 4.1.

Similar spatiotemporal structures have also been observed on other substrates, such as Pt(100), Pt(210), and polycrystalline Pt samples, and in other surface chemical reactions [43]. Further studies of catalytic CO oxidation investigated the effects of catalytic boundaries and microdesigned catalytic domains [127, 128], and the influence of laser heating on spatiotemporal patterns [129]. While the operation of PEEM is restricted to pressures below  $10^{-3}$  mbar, the development of new optical imaging techniques such as ellipsomicroscopy for surface imaging (EMSI) and reflection anisotropy microscopy (RAM) [124] made also possible to perform studies of pattern formation up to atmospheric pressures [130, 131].

## 4.2 Mechanism of the reaction

The mechanism of CO oxidation on Pt single crystal surfaces is well established (see Ref. [43] for a review). Under isothermal low-pressure conditions ( $p < 10^{-3}$  mbar), the net reaction  $2\text{CO} + \text{O}_2 \rightarrow 2\text{CO}_2$  follows the Langmuir-Hinshelwood scheme



Here,  $*$  denotes a free adsorption site on the catalytic surface. Molecules of CO and oxygen have to adsorb before the reaction due to a high energy barrier in the gas phase. The adsorption of oxygen is dissociative. Adsorbed CO molecules are bound to the surface considerably less strongly than oxygen atoms and hence may desorb as well as diffuse on the surface; such processes are negligible for  $\text{O}_{\text{ad}}$  under typical reaction conditions ( $T < 600\text{ K}$ ).

At temperatures above 300 K, produced carbon dioxide almost immediately desorbs into the gas phase, leaving again free space for adsorption. The reaction mechanism is illustrated in Fig. 4.2.

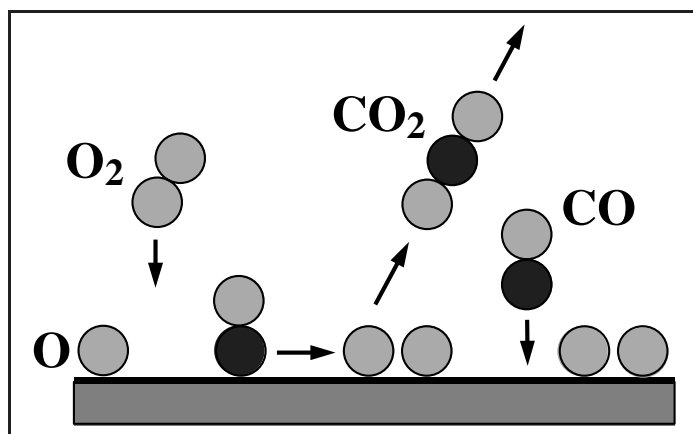


Figure 4.2: *Illustrative drawing of the basic reaction mechanism: adsorption of CO and O<sub>2</sub> molecules, CO diffusion, and reaction.*

In a wide range of parameters, the system exhibits bistability between a mainly oxygen covered, reactive state, and a non-reactive CO covered state. This bistability can be traced back to an asymmetric inhibition of adsorption. Adsorbed oxygen forms an open structure where CO molecules still can adsorb and react, whereas a fully CO covered surface completely inhibits the adsorption of oxygen, and hence poisons the reaction.

Temporal rate oscillations require an additional mechanism, provided by an adsorbate-driven structural phase transition in the top substrate layer. The clean Pt(110) surface reconstructs into a  $1 \times 2$  ‘missing row’ structure, see Fig. 4.3. The reconstruction can be reversibly lifted by adsorbed CO molecules. Oxygen adsorption is more likely on the non-reconstructed  $1 \times 1$  phase and therefore the phase transition can cause periodic switching between the two states with different catalytic activity. The mechanism of oscillations can be understood as follows [43]: starting with a partwise CO covered  $1 \times 1$  phase, the adsorption rate of oxygen will be high. As a consequence, the consumption of adsorbed CO molecules by the reaction will increase, and hence the CO coverage will decrease. Below a critical value of the CO coverage, the surface will reconstruct into the  $1 \times 2$  phase. On this surface, oxygen adsorption is low, and consequently the CO coverage will rise. Above threshold, the reconstruction is lifted, and the initial situation of a CO covered  $1 \times 1$  surface is established again.

Another reversible restructuring process, where the initially flat surface facets under the influence of the catalytic reaction into new orientations, was observed on Pt(110) at relatively low temperature ( $T < 530$  K). Above this temperature, a thermal reordering keeps the surface flat. The facets are formed on a time scale of several minutes, and their size is of the

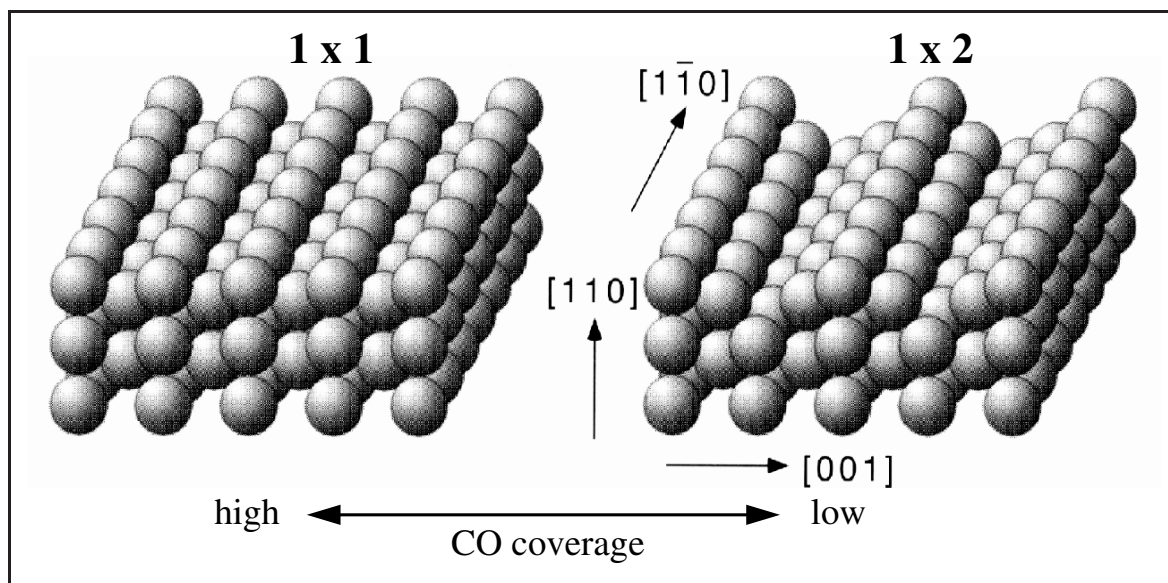


Figure 4.3: Illustration of the CO induced surface phase transition of Pt(110), which is responsible for the occurrence of rate oscillations.

order of 100 Å. The faceting process on Pt(110) is responsible for an induction period in the development of rate oscillations and for the occurrence of mixed-mode oscillations [118].

An additional feature of the reaction mechanism is the formation of subsurface oxygen. Under certain conditions, oxygen atoms not only adsorb on the surface, but also an oxygen species may form below the surface, which in PEEM measurements appears as very bright patches in the images [132]. After being stored below the surface for a certain time, oxygen atoms may later be released back onto the surface. The formation of subsurface oxygen is responsible for the reflective collision of traveling excitation waves [133], a rather unusual phenomenon in reaction-diffusion systems.

Spatial coupling along the catalytic surface is provided by two different mechanisms. Surface diffusion of adsorbed CO molecules gives rise to local coupling between neighbored sites. Diffusion is fast along the  $[1\bar{1}0]$  orientation of the Pt(110) single crystal surface, while it is slower by a factor of about 2 parallel to the  $[001]$  orientation of the substrate lattice. Due to this diffusion anisotropy, spatial patterns are elliptically deformed. The second type of spatial coupling acts via the gas phase as a consequence of mass balance in the reaction. Since the mean free path in the gas phase is typically large in comparison to the size of the chamber, local partial pressure variations that result from the consumption of the educts by the reaction quickly extend to affect the whole system. Therefore, the gas-phase coupling is *global*. It has been experimentally found that the interplay between diffusion and gas phase coupling

can lead to phenomena such as synchronous oscillations [134], standing waves [46] [see Fig. 4.1(c)], and cellular structures [126]. The accompanying relative variations of partial pressures typically are less than 2-3% in magnitude.

### 4.3 Mathematical modeling

A simple mathematical model of CO oxidation on Pt(110), consisting of a set of coupled ordinary differential equations and neglecting the spatial degrees of freedom, has been developed by Krischer, Eiswirth, and Ertl [49, 135–137]. The model is based on a decomposition of the entire reaction into elementary steps. If the coverages of CO<sub>ad</sub> and O<sub>ad</sub> are denoted by the variables  $u$  and  $v$ , respectively, their kinetics may be described by the equations

$$\dot{u} = k_1 p_{\text{CO}} s(\text{CO}) - k_2 u - k_3 u v, \quad (4.1)$$

$$\dot{v} = k_4 p_{\text{O}_2} s(\text{O}_2) - k_3 u v. \quad (4.2)$$

Both variables can vary in the interval from 0 to 1. The production of carbon dioxide with rate constant  $k_3$  is described by the last term in each equation. The second term in equation (4.1) quantifies desorption of CO molecules with rate constant  $k_2$ . The first term in equations (4.1) and (4.2) describes the kinetics of CO and oxygen adsorption, respectively. The adsorption rates are determined by the respective impingement rate constants of CO and O<sub>2</sub> molecules  $k_1$  and  $k_4$ , the CO and O<sub>2</sub> partial pressures  $p_{\text{CO}}$  and  $p_{\text{O}_2}$ , and the sticking coefficients of molecules impinging on the surface, which are given by the expressions

$$s(\text{CO}) = s_{\text{CO}} (1 - u^3), \quad (4.3)$$

$$s(\text{O}_2) = s_{\text{O}_2} (1 - u - v)^2. \quad (4.4)$$

Here, the parameters  $s_{\text{CO}}$  and  $s_{\text{O}_2}$  denote the sticking probabilities for CO and oxygen adsorption on the clean surface. The term  $(1 - u^3)$  for CO adsorption describes a precursor effect [138]: impinging molecules of CO can occupy a state on top of another CO molecule and from there diffuse to other surface sites. The cubic exponent specifies that the assumed average number of surface sites tested by CO molecules before returning to the gas phase is three. The dissociative adsorption of oxygen proceeds via second order kinetics in the fraction of free sites  $(1 - u - v)$ .

To account for the  $1 \times 1 \rightleftharpoons 1 \times 2$  phase transition, a third variable  $w$ , denoting the fraction of the surface area found in the non-reconstructed  $1 \times 1$  structure, must be introduced into the

model. The temporal variation of this additional variable can be described by the equation

$$\dot{w} = k_5 [f(u) - w], \quad (4.5)$$

where  $f(u)$  is the equilibrium value of  $w$  as determined by the CO coverage, and  $k_5$  denotes the temperature dependent rate constant of the phase transition [137]. In the original model, a piecewise approximation of the function  $f(u)$  was used. Later, the following functional form was proposed [139]:

$$f(u) = \frac{1}{1 + \exp(\frac{u_0 - u}{\delta u})}. \quad (4.6)$$

Here, the parameter  $u_0$  determines the threshold value above which adsorbed CO molecules significantly affect the surface structure, and  $\delta u$  specifies the steepness of the threshold. The function  $f(u)$  is plotted as solid line in Fig. 4.4 for parameters which are used later; the dashed line indicates the original piecewise approximation.

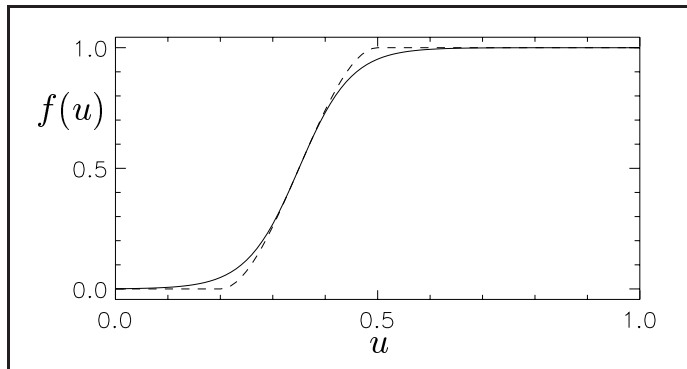


Figure 4.4: The function  $f(u)$  for parameters  $u_0 = 0.35$  and  $\delta u = 0.05$  (solid line), and its piecewise original form (dashed line). Below  $u \approx 0.2$ , the surface is found almost completely in the reconstructed  $1 \times 2$  structure, whereas the non-reconstructed  $1 \times 1$  structure is almost exclusively present above  $u \approx 0.5$ .

As already noted in Section 4.2, the oxygen sticking probabilities on the two different structural states of the surface are different, with  $s_{1 \times 1} \approx 0.6$  and  $s_{1 \times 2} \approx 0.4$ . Thus, equation (4.5) is coupled to equation (4.4) [and thus to equation (4.2)] via the oxygen sticking probability  $s_{O_2}$ , which in fact is given by the expression

$$s_{O_2} = [s_{1 \times 1} w + s_{1 \times 2} (1 - w)]. \quad (4.7)$$

This coupling provides a negative feedback on the reaction kinetics, such that oscillatory dynamics becomes possible.

The parameters of the three-variable system (4.1), (4.2), and (4.5) have been previously determined in independent studies of each elementary reaction step (see Ref. [137]). Three

external control parameters can be varied freely, namely the partial pressures  $p_{\text{CO}}$  and  $p_{\text{O}_2}$ , and the temperature  $T$ , which determines the rate constants  $k_2$ ,  $k_3$ , and  $k_5$  according to the Arrhenius activation law, i.e.,

$$k_i = v_i \exp \left( \frac{-E_i}{kT} \right).$$

Numerical integration of the above set of model equations was found to reproduce many experimental observations. Depending on the control parameters, the model exhibits monostable, bistable, oscillatory, or excitable dynamics. The resulting bifurcation diagram has been studied with the piecewise approximation of the function  $f(u)$  by Krischer *et al.* [137]. The response of the system to periodic external perturbations was also investigated, yielding detailed insight into the structure of entrainment bands [140].

To reproduce the properties of spatiotemporal pattern formation, the model has been extended to include surface diffusion of adsorbed CO molecules. Numerical simulations of the resulting system of partial differential equations (PDE's) by Bär *et al.* revealed propagating reaction fronts and solitary-wave phenomena [141, 142]. It was also found that such behavior can already be described by a reduced version of the model that contains only two variables [143] and represents a variant of a model proposed by Barkley [144]. The reduced model was successfully applied to understand the properties of spiral waves [145, 146] and chemical turbulence [51, 147] under excitable conditions.

Further studies of the three-variable model have concentrated on the effects of intrinsic global gas-phase coupling on pattern formation [114, 148–153]. Assuming that the CO kinetics in the chamber obeys the laws of an ideal gas, the evolution equation of the CO partial pressure in the reaction chamber reads [151, 153]

$$\frac{\partial p_{\text{CO}}}{\partial t} = \frac{1}{\tau} (p_0 - p_{\text{CO}}) - \kappa \int_S [k_1 s_{\text{CO}} p_{\text{CO}} (1 - u^3) - k_2 u] dx, \quad (4.8)$$

where  $\tau$  is the residence time of CO molecules in the pumped reaction chamber,  $p_0$  denotes the base CO partial pressure in absence of any reaction, the coupling coefficient  $\kappa$  is specified by the gas temperature and the chamber volume,  $u(x, t)$  denotes the local CO coverage, and the integration is performed over the entire surface area  $S$ . The global variations of CO partial pressure are given as superposition of the incoming flux of CO molecules, the flux pumped out of the chamber, and the rate of consumption of CO molecules in the surface reaction. A similar evolution equation can be derived for the variation of the oxygen partial pressure. However, in relation to the CO partial pressure variations, the consumption of oxygen molecules produces an effect of less than a quarter, because each  $\text{O}_2$  molecule provides

two atoms for the reaction, and the  $O_2$  partial pressure is typically at least two times larger than the CO pressure.

The effects of intrinsic gas phase coupling according to equation (4.8) have been studied by Falcke and Engel [114, 150–152]. Their numerical simulations have shown a large variety of patterns, including clusters, standing waves, and irregular coverage patterns. By supplementing the model by a fourth species [133, 139] accounting for the formation of subsurface oxygen, the experimentally observed pattern of alternating standing waves [46] was later successfully modeled by von Oertzen *et al.* [153].





**Part II.**  
**Theoretical Investigations of**  
**CO Oxidation on Pt(110)**



---

## Chapter 5

### Model equations and pattern characterization

---

The second part of this work is devoted to theoretical investigations of pattern formation in CO oxidation on Pt(110). The following chapter is organized as follows: in Section 5.1, the used reaction-diffusion model of CO oxidation on Pt(110) with global delayed feedback is described. Subject of Section 5.2 is the numerical implementation of the model equations. In Section 5.3, a tool developed for the interpretation of numerically generated patterns is presented.

#### 5.1 Model of CO oxidation with global delayed feedback

The employed model of CO oxidation on Pt(110) is based on the original scheme by Krischer, Eiswirth, and Ertl [137] which has been introduced in Section 4.3. The model contains three variables which all depend on both space and time. The variables  $u$  and  $v$  denote the surface coverages of carbon monoxide and oxygen, respectively. The variable  $w$  is related to the structural state of the surface and denotes the local fraction of the surface area found in the non-reconstructed  $1 \times 1$  structure. All three variables can vary in the interval from 0 to 1. The equations are

$$\frac{\partial u}{\partial t} = k_1 p_{\text{CO}} s_{\text{CO}} (1 - u^3) - k_2 u - k_3 u v + D \nabla^2 u, \quad (5.1)$$

$$\frac{\partial v}{\partial t} = k_4 p_{\text{O}_2} [s_{1 \times 1} w + s_{1 \times 2} (1 - w)] (1 - u - v)^2 - k_3 u v, \quad (5.2)$$

$$\frac{\partial w}{\partial t} = k_5 \left( \frac{1}{1 + \exp(\frac{u_0 - u}{\delta u})} - w \right). \quad (5.3)$$

Most parameters of the model are fixed throughout this work; their values are given in Table 5.1. The only parameters that are later varied are  $p_{\text{CO}}$  and  $p_{\text{O}_2}$  (denoting CO and O<sub>2</sub> partial

Symbol	Value	Meaning
$k_1$	$3.14 \times 10^5 \text{ s}^{-1} \text{ mbar}^{-1}$	Impingement rate of CO molecules
$k_2$	$10.21 \text{ s}^{-1}$	Desorption rate of CO molecules
$k_3$	$283.8 \text{ s}^{-1}$	Reaction rate
$k_4$	$5.860 \times 10^5 \text{ s}^{-1} \text{ mbar}^{-1}$	Impingement rate of O <sub>2</sub> molecules
$k_5$	$1.610 \text{ s}^{-1}$	Rate for the phase transition
$s_{\text{co}}$	1.0	CO sticking probability
$s_{1 \times 1}$	0.6	Oxygen sticking probability on the 1x1 phase
$s_{1 \times 2}$	0.4	Oxygen sticking probability on the 1x2 phase
$u_0, \delta u$	0.35, 0.05	Parameters for the structural phase transition
$D$	$40 \mu\text{m}^2 \text{ s}^{-1}$	CO diffusion coefficient

Table 5.1: *Parameters of the model at  $T = 545 \text{ K}$ . All parameters have been previously determined in independent studies of each elementary reaction step (see Ref. [137]).*

pressure, respectively). Equations (5.1)–(5.3) take into account the reaction, the adsorption of CO and oxygen molecules, the desorption of CO molecules, the structural phase transition of the platinum surface, and the surface diffusion of adsorbed CO molecules. Oxygen desorption and diffusion are negligible at the considered temperature ( $T = 545 \text{ K}$ ). For simplicity, faceting of the surface, the formation of subsurface oxygen, and effects caused by surface defects are not taken into account. The intrinsic gas-phase coupling is also neglected because it is weak compared to the typical modulation levels that can be achieved with external variations of the partial pressures. Furthermore, state-independent diffusion is assumed, and the coordinates are rescaled to counterbalance the diffusion anisotropy.

### Implementation of global delayed feedback

In surface chemical experiments, global delayed feedback can be artificially introduced by means of controlled variation of one of the partial pressures in the reaction chamber. Therefore, to implement global delayed feedback in the CO oxidation model, it is assumed that the CO partial pressure  $p_{\text{co}}$  in equation (5.1) is not constant but varies according to the equation

$$p_{\text{co}}(t) = p_0 - \mu [\bar{u}(t - \tau) - u_{\text{ref}}], \quad (5.4)$$

where  $\bar{u}(t) = \frac{1}{S} \int_S u(x, t) dx$  denotes the spatial average of the CO coverage  $u$  at time  $t$ . The integration is performed over the entire surface area  $S$ . The two control parameters are the

feedback intensity  $\mu$  and the time delay  $\tau$ . The delay can be adjusted to control the phase relation between the total CO coverage and the feedback signal. The parameter  $p_0$  specifies the base CO pressure for vanishing feedback. The reference value  $u_{\text{ref}}$  is chosen as the value of  $u$  in the unstable steady state in absence of feedback. In the limit of a small delay  $\tau$  the feedback acts towards stabilization of the target state  $\bar{u} = u_{\text{ref}}$ .

According to equation (5.4), the integral CO coverage  $\bar{u}$  is used to generate the feedback signal. In the surface chemical experiments presented later in this work, the PEEM intensity which is a nonlinear function of both the CO and oxygen coverages is actually used to compute the control signal. However, the functional form of this dependence is not exactly known (see Ref. [124]). The description in equation (5.4) therefore is a simplification of the experimental setup.

## 5.2 Numerical methods

The system of partial differential equations (5.1)–(5.3), with the parameter  $p_{\text{CO}}$  varying according to equation (5.4), has been solved numerically in one and two space dimensions. Two different combinations of the parameters  $p_{\text{O}_2}$  and  $p_0$  have been used, and in each case multiple simulations with varying feedback parameters  $\mu$  and  $\tau$  were performed.

The following discretization of space and time is used for one-dimensional systems of length  $L$ :

$$\begin{aligned} x &= 0, \Delta x, 2\Delta x, \dots, N\Delta x = L, \\ t &= 0, \Delta t, 2\Delta t, \dots \end{aligned}$$

A corresponding spatial discretization is employed for  $x$  and  $y$  in rectangular two-dimensional systems. A second-order finite difference scheme [154] is used for the approximation of the second order spatial derivative in equation (5.1). The temporal derivatives are approximated using an explicit Euler scheme. For instance, equation (5.1) is numerically solved in one space dimension according to the scheme

$$u_i^{n+1} = u_i^n + \Delta t g(u_i^n, v_i^n) + \frac{D\Delta t}{(\Delta x)^2} (u_{i+1}^n + u_{i-1}^n - 2u_i^n), \quad (5.5)$$

where  $g(u, v)$  describes the local dynamics of  $u$ , the subscripts denote the spatial position and the superscripts represent the time step. In two dimensions, the corresponding computation scheme for the diffusive part is given by a five-point formula.

In most computations, the system size is  $L = 0.8 \text{ mm}$  for one-dimensional systems and  $0.4 \times 0.4 \text{ mm}^2$  or  $0.8 \times 0.8 \text{ mm}^2$  for two-dimensional systems. The minimal number of grid points is 200 (or  $200 \times 200$ ) in one (two) space dimensions, resulting in a mesh size of  $\Delta x = 4 \mu\text{m}$ . Smaller mesh sizes like  $\Delta x = 1 \mu\text{m}$  have not been found to produce qualitatively different results. A constant time step  $\Delta t = 0.001$  is used. This time step well fulfills the condition for numerical stability of algorithm (5.5) [155],

$$\Delta t \leq \frac{(\Delta x)^2}{2D}.$$

Long integration times ( $t > 3000 \text{ s}$ ) ensure that transients have decayed before the end of a calculation. Different initial conditions are employed, depending on the problem under study. The boundary conditions in one-dimensional simulations are either of Neumann (no-flux) type,

$$\left. \frac{\partial u}{\partial x} \right|_{x=0} = \left. \frac{\partial u}{\partial x} \right|_{x=L} = 0,$$

or, alternatively, periodic boundaries are imposed,

$$u(0) = u(L).$$

In two-dimensional systems, always no-flux boundary conditions are employed. The numerical algorithm has been implemented on a computer using the programming language C.

### 5.3 Transformation to amplitude and phase variables

As already pointed out in Section 2.3, the complex Ginzburg-Landau equation (CGLE) is the amplitude equation of a field of diffusively coupled Hopf oscillators and describes small-amplitude harmonic oscillations. The oscillations observed in real experimental situations and in realistic models are usually non-harmonic, and the system is not close to a Hopf bifurcation. Nonetheless, the normal form approach is often applied to interpret the data even in such cases. To provide a link to general studies of pattern formation in oscillatory reaction-diffusion systems performed in the framework of the CGLE, it would thus be convenient to have the amplitude and the phase variable also defined for anharmonic oscillations, in such a way that they can be compared to the amplitude and the phase of harmonic oscillations in

the normal form theory. It should be noted that the local phases of general anharmonic oscillations were first introduced by Kuramoto [25] in his analysis of phase dynamics. However, only small amplitude deviations from the non-perturbed limit cycle were then considered.

A recent approach to such a variable transformation has been undertaken by employing a frequency demodulation technique to filter relevant information from numerical and experimental data [40] (cf. Section 3.1.2). This technique is efficient when the majority of the dynamical power is concentrated in a single mode, but it is also limited to this case. The time-resolved description of oscillatory behavior requires extensive data processing and is only achievable for sufficiently slow pattern evolutions.

The variable transformation presented below follows a different idea. It is an empirical method to transform a pair of model variables into an amplitude and a phase after computational modeling. It cannot be ensured that this transformation is generally applicable. However, when certain conditions on the spatiotemporal dynamics of the pattern under analysis are fulfilled, the method turns out to be a useful tool for the time-resolved characterization of patterns involving anharmonic dynamics.

When a system shows periodic oscillations in absence of spatial coupling, visualization of two variables is usually sufficient to capture the relevant dynamical features. In the projection plane of these two variables, the limit cycle then yields a closed trajectory. Assume that the projection variables are chosen in such a way that this trajectory has no self-intersection. The idea is that, when spatial coupling is eventually introduced, the projected uniform limit cycle can be used as a reference for the characterization of the dynamics in a spatiotemporal pattern.

The developed variable transformation is illustrated in Fig. 5.1. Suppose that  $u$  and  $w$  are the projection variables and the reference trajectory is the closed orbit shown in Fig. 5.1. For any state  $P$  with coordinates  $(u, w)$  in the projection plane, a pair of new variables  $R$  and  $\phi$  shall be defined such that  $R$  can be interpreted as an amplitude and  $\phi$  as a phase corresponding to this local state of the system. To do this, at first some point  $O$  inside the reference orbit is chosen, and it is taken as the coordinate origin in the projection plane. Hence, any point  $P$  is characterized by a radius vector of length  $\rho = \overline{OP}$ . Notice the point  $Q$  where this radius (or its extension) intersects with the chosen orbit. The length  $\rho_{\text{ref}} = \overline{OQ}$  determines the reference radius for the point  $P$ . Next, some ‘initial’ point  $Q_0$  is marked on the orbit and the time  $\tilde{T}$  needed to reach point  $Q$  along the reference cycle is determined. The amplitude and the phase are then defined as  $R = \rho / \rho_{\text{ref}}$  and  $\phi = 2\pi\tilde{T} / T_{\text{ref}}$ , where  $T_{\text{ref}}$  is the

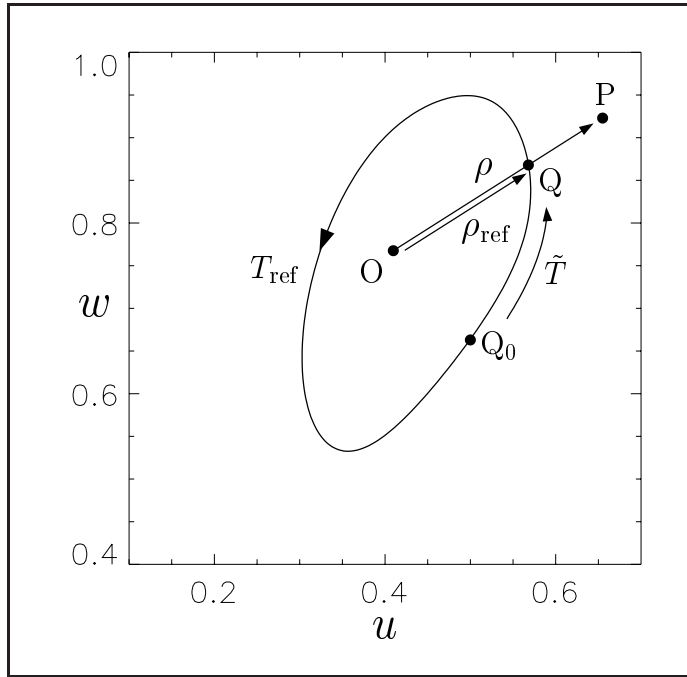


Figure 5.1: Definition of the amplitude  $R = \rho / \rho_{\text{ref}}$  and phase  $\phi = 2\pi \tilde{T} / T_{\text{ref}}$  for non-harmonic oscillations.

period of the reference orbit.

Note that according to this definition, the amplitude is  $R = 1$  as long as the system stays on the reference orbit. Moreover, for the motion corresponding to the reference orbit, the phase  $\phi$  increases at a constant velocity with time and changes by  $2\pi$  after each period. When local oscillations are nearly harmonical and the reference orbit is a circle with point O in its center, the above definition yields the usual phase and amplitude variables. The coordinate origin O is best chosen as the unstable uniform steady state of the system to guarantee that a local suppression of oscillations indeed corresponds to a vanishing amplitude  $R$ .

In the following chapter, this empirical amplitude-phase description is applied to qualitatively interpret spatiotemporal patterns obtained in numerical simulations of the CO oxidation model with artificial global feedback. To obtain the reference orbit, the projection of uniform oscillations on the plane with the variables  $u$  and  $w$  shall be used.

It should be noted that the presence of the feedback may significantly affect the shape of uniform oscillations. Therefore, different reference orbits are employed for different feedback parameters by generating a new reference cycle following each fixed parameter simulation of the model (5.1)–(5.4). This is done by an additional numerical simulation of the model (5.1)–(5.3) in absence of diffusion ( $D = 0$ ), where the feedback signal generated previously by the full pattern forming system is applied as external  $p_{\text{CO}}$  forcing. When the resulting attractor is periodic it directly can be used as a reference. When the full system generates



an aperiodic forcing signal the resulting attractor in the projection plane deviates from a periodic orbit. In such cases, the reference orbit is chosen as the long-time average of the resulting projected trajectory. The reference orbit is computed and the variable transformation is performed by a numerical routine that has been numerically implemented using the programming language *PV-Wave*.



---

## Chapter 6

# Pattern formation under global delayed feedback

---

In this chapter, a detailed numerical study of pattern formation in CO oxidation on Pt(110) with artificial global delayed feedback is presented. Two cases are considered in the following, differing in the initial reaction state. In Section 6.1, the effects of global delayed feedback on stable uniform oscillations and stable spiral waves are investigated. The observed phenomena include phase flips, asynchronous oscillations, and dynamical clustering. In Section 6.2, global delayed feedback is applied to a spatiotemporally chaotic state. It is shown that turbulence can be suppressed by this method, and various chaotic and regular spatiotemporal patterns are found near the transition from turbulence to uniform oscillations.

## 6.1 Manipulating non-chaotic patterns

In the numerical study presented in this section, the parameter values of model (5.1)–(5.4) are chosen in such a way that oscillations are non-harmonic and uniform oscillations are stable in absence of feedback. At first, the effects of global delayed feedback on pattern formation are studied in one space dimension. The chosen parameter values of the partial pressures are  $p_0 = 4.15 \times 10^{-5}$  mbar and  $p_{\text{O}_2} = 0.90 \times 10^{-5}$  mbar. The reference value of the CO coverage is  $u_{\text{ref}} = 0.4097$ , which corresponds to the unstable steady state. The other parameters are given in Table 5.1. Unless stated otherwise, the system size is 0.8 mm and periodic boundary conditions are used.

### 6.1.1 Overview of feedback effects

Multiple simulations of model (5.1)–(5.4) at different values of the feedback intensity  $\mu$  and the delay time  $\tau$  have been performed. The results are summarized in Fig. 6.1. This diagram shows the types of stable regimes reached after transients have decayed. The delay time is

measured in multiples of the natural oscillation period in absence of feedback,  $T_0 = 3.33$  s (note that when feedbacks are operating the actual period of uniform oscillations is feedback-dependent and will to some extent differ from  $T_0$ ). The feedback intensity in Fig. 6.1 is normalized to the equilibrium CO partial pressure  $p_0$  in the reaction chamber in absence of feedback. Note that the ratio  $\mu/p_0$  yields an estimate of the relative variation of partial pressure caused by such a feedback.

Depending on the delay and intensity, the feedback can maintain uniform oscillations or induce various spatiotemporal patterns. Examining Fig. 6.1, it is seen that as the delay is increased, the diagram is approximately repeated at integer multiples of  $T_0$  (this trend is continued at larger delays, not shown in Fig. 6.1). However, the stability regions of the patterns other than uniform oscillations shrink at larger delays.

Uniform oscillations are found in a large region of the two-parameter plane. The uniform oscillations show strong hysteresis (bold lines show the boundaries where uniform

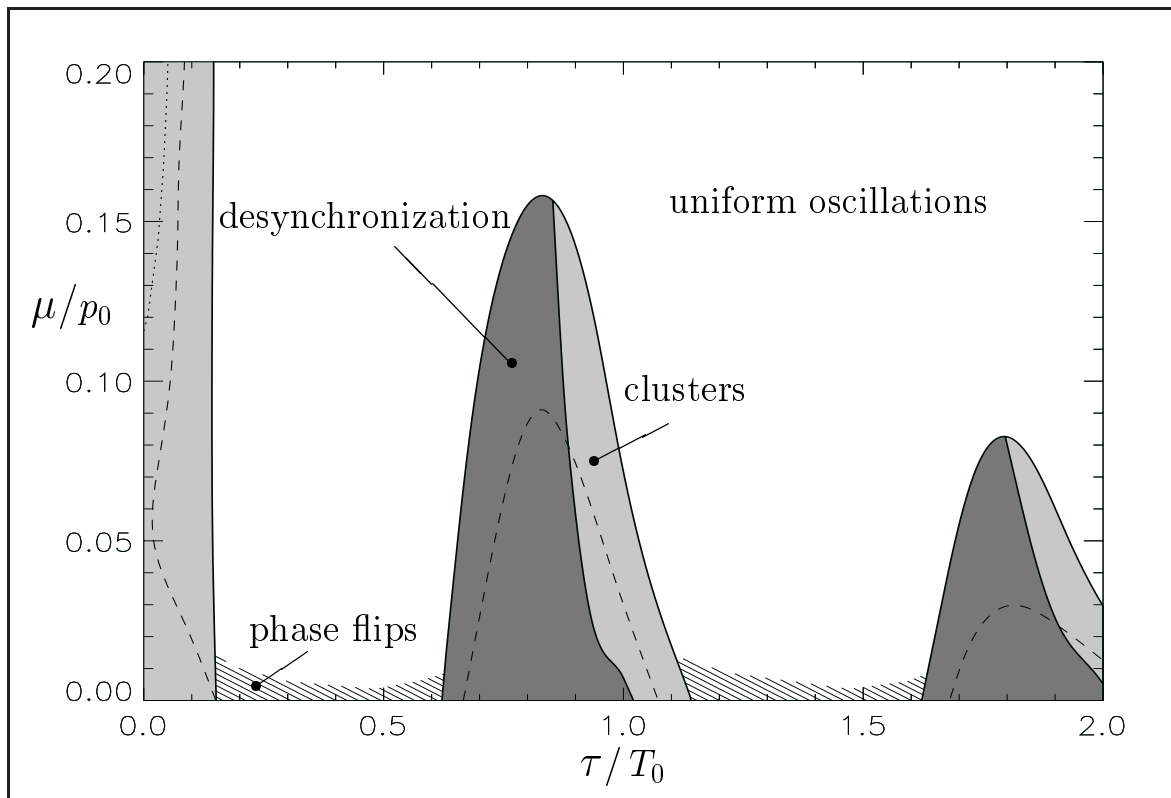


Figure 6.1: Approximate existence regions of various feedback-induced patterns in the one-dimensional system: uniform oscillations (white), asynchronous oscillations (dark gray), cluster patterns (light gray), and phase flips (hatched regions). The dashed lines mark the borders of the hysteresis of uniform oscillations.

oscillations set on when increasing the feedback intensity, whereas dashed lines indicate the boundaries where such oscillations break down as the feedback intensity is decreased). In the hysteresis regions, the final pattern depends on the initial conditions because the uniform attractor coexists here with the attractor of another pattern.

For comparison, by the dotted line in Fig. 6.1 the boundary is shown where in absence of diffusion the unstable steady state of the system becomes stabilized by the applied feedback (the stabilization takes place at small delays  $\tau/T_0 < 0.06$  and large feedback intensities  $\mu/p_0 > 0.11$ ). An example of this process is shown in Fig. 6.2. However, in the full pattern forming system that includes diffusion, the spatially uniform suppression of oscillations is never observed. Instead, at small delays the system evades the suppression of oscillations through the formation of clusters.

Fig. 6.3 displays three typical examples of different nonuniform feedback-induced patterns. In the pattern shown in Fig. 6.3(a), the medium is in the uniform state almost anywhere except for a narrow interval with strong spatial variation. As it is shown later, this pattern corresponds to a *phase flip* traveling across the medium. In contrast to this, the pattern in Fig. 6.3(b) is characterized by a gradual spatial variation extending over the whole medium. It is shown below that such patterns are found when *desynchronization* through the feedback takes place. In Fig. 6.3(c) the pattern consists of different large regions with almost uniform distributions separated by narrow interfaces. Such *cluster patterns* are also discussed below.

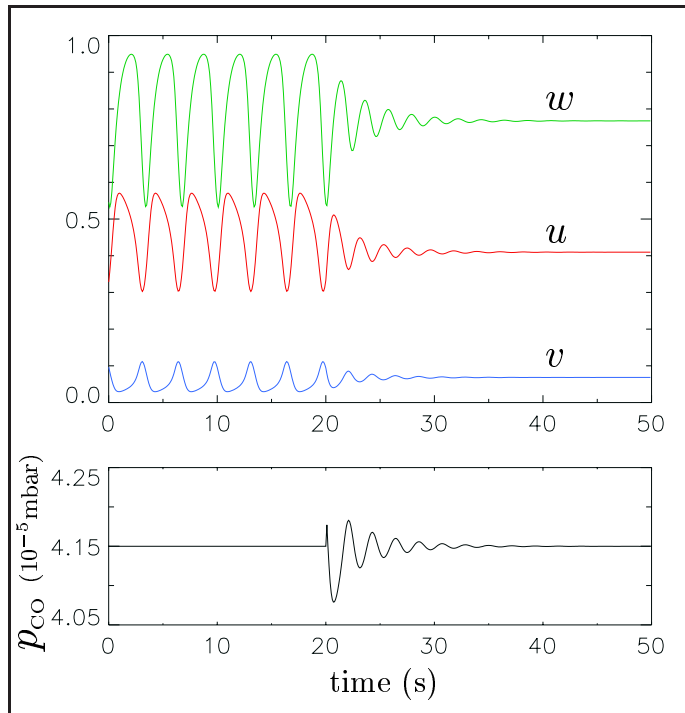


Figure 6.2: Stabilization of the steady state in the homogeneous system ( $D = 0$ ). The temporal evolution of the model variables (top) and the feedback-induced variations of the CO partial pressure (bottom) are shown. The feedback is switched on at  $t = 20$  s. After successful suppression of the oscillations, the control signal vanishes. The feedback parameters are  $\tau/T_0 = 0$  and  $\mu/p_0 = 0.17$ .

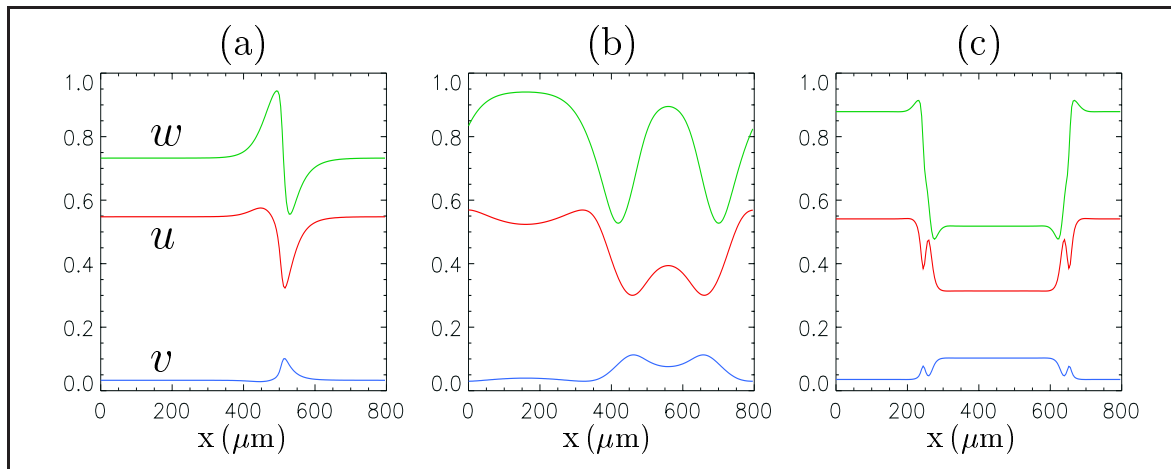


Figure 6.3: Feedback-induced coverage patterns: (a) phase flip, (b) asynchronous oscillations, and (c) a cluster pattern. For each pattern the values of the parameters  $\tau/T_0$  and  $\mu/p_0$  are, respectively, (a) 0.165, 0.012, (b) 0.781, 0.012, and (c) 0.045, 0.289.

### 6.1.2 Phase flips

As already noted, for the chosen model parameters uniform oscillations are stable with respect to spontaneous phase modulation in absence of feedback. For the same parameters, traveling waves (and spiral waves in the two-dimensional system) can also be observed, depending on the choice of the initial and the boundary conditions. Sufficiently strong global delayed feedbacks suppress all such structures, so that only uniform oscillations are found inside the white region in Fig. 6.1. After a transient, any initial condition eventually leads to uniform oscillations here. The time needed to reach uniform oscillations greatly increases near the instability boundaries of uniform oscillations.

At small feedback intensities corresponding to the hatched areas in Fig. 6.1, either uniform oscillations or patterns of propagating *phase flips* are found in the simulations, depending on the initial conditions. To produce a phase flip, a simulation is started with a constant phase gradient of  $2\pi$  across the system. The feedback tends to establish uniform oscillations, but, if it is relatively weak, it cannot achieve this in the whole medium. Thus, a narrow region with strong concentration gradients is formed, see Fig. 6.3(a). This region travels through the medium. To analyze the properties of such traveling patterns, the variable transformation technique described in Section 5.3 is used. After transformation to local phase and amplitude variables, the pattern of a phase flip takes the form displayed in Fig. 6.4(a). It is seen that the phase  $\phi$  undergoes a full rotation of  $2\pi$  inside the nonuniform region, whereas the amplitude  $R$  displays only small modulations. The states of the medium on the left and right side of the phase flip differ by a phase shift of  $2\pi$  only and hence are physically indistinguishable.

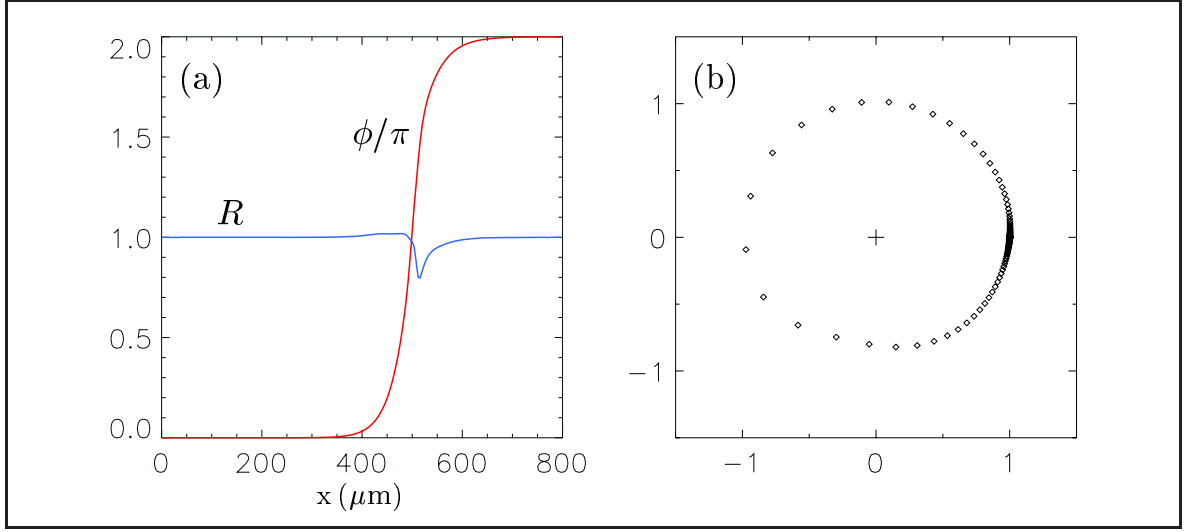


Figure 6.4: (a) Spatial dependence of the amplitude  $R$  (blue line) and the phase  $\phi$  (red line) in a phase flip. The phase portrait (b) shows the same data in polar coordinates. The same parameters as in Fig. 6.3(a).

A phase portrait of the same structure is shown in Fig. 6.4(b). Here, the amplitudes and phases of all points along the phase flip are displayed in polar coordinates. The phase  $\phi$  of a point is represented by the polar angle and the amplitude  $R$  is the distance to the coordinate origin. The points accumulate in the state corresponding to the uniformly oscillating regions.

Phase flips were first reported for the periodically forced CGLE [62] (see also Ref. [34]). They have been systematically investigated for the CGLE in the presence of a global feedback [37, 112], revealing that, depending on the feedback parameters, a phase flip can stop and reverse its direction of motion. Following Ref. [112], a phase flip is said to have positive velocity if the phase is increased by  $2\pi$  after its passage and the velocity is negative if the phase decreases by  $2\pi$  behind it. With this in mind, the dependence of the propagation velocity of phase flips on the delay time  $\tau$  has been numerically examined in the currently investigated model with anharmonic oscillations. As displayed in Fig. 6.5, the velocity decreases for higher delays and changes its sign at  $\tau/T_0 \approx 0.155$ . Another prediction of the study of the CGLE with global feedback is that, as the feedback intensity  $\mu$  is decreased, the width of the phase flip grows as  $\delta x \sim \mu^{-1/2}$  and in the limit  $\mu \rightarrow 0$  the phase flip transforms into uniform oscillations in a finite system. It has been checked that this effect is also observed for phase-flip patterns in the presently considered model.

On the other hand, phase flips become unstable in the simulations if the feedback intensity exceeds a certain delay-dependent threshold (see Fig. 6.1). They disappear through the formation of an amplitude defect if the feedback intensity is increased beyond the critical

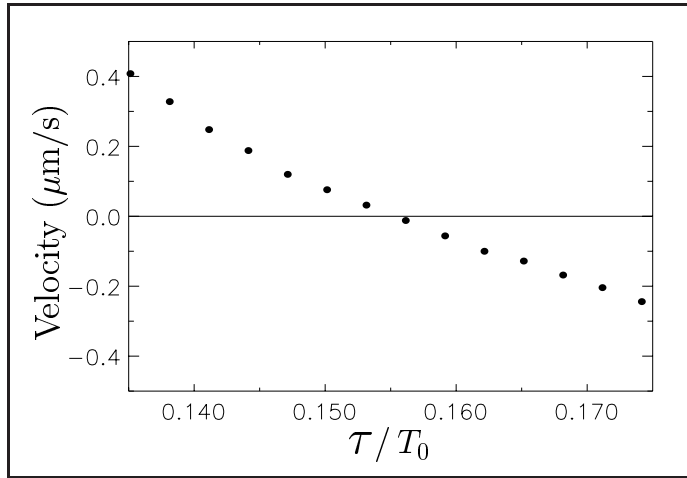


Figure 6.5: *Dependence of the velocity of phase flips on the delay time. The feedback intensity is constant,  $\mu/p_0 = 0.012$ .*

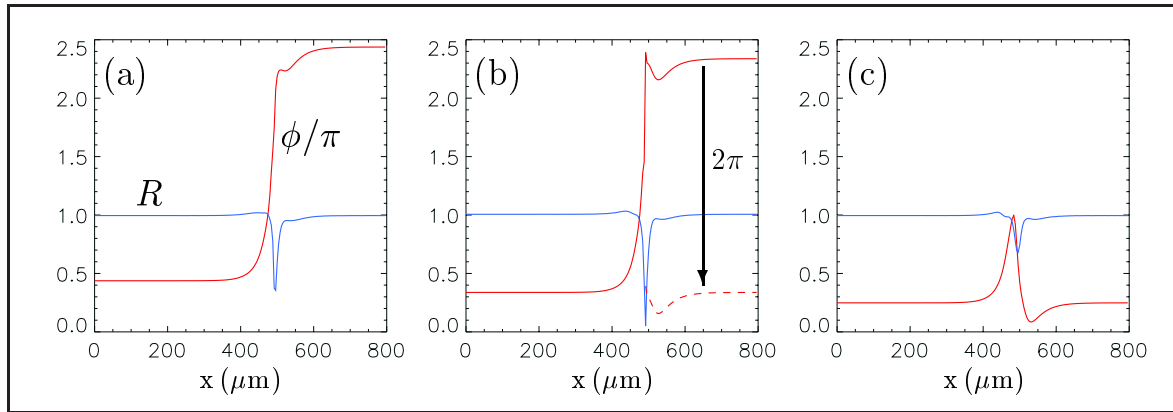


Figure 6.6: *Destruction of a phase flip by strong global feedback. The time interval between the subsequent snapshots (a)-(c) showing oscillation phases (red lines) and amplitudes (blue lines) is 3 seconds. The feedback parameters are  $\tau/T_0 = 0.167$  and  $\mu/p_0 = 0.014$ . The initial phase flip was obtained using a slightly smaller feedback intensity  $\mu/p_0 = 0.012$ .*

value. This process is analyzed in Fig. 6.6 by means of the amplitude and phase characterization. Before the amplitude defect occurs, the phase variation is steepened, see Fig. 6.6(a). Then, at some moment the oscillation amplitude drops down to zero inside the phase flip. When this occurs, the phase makes a slip of  $2\pi$  at one side of the defect, as illustrated in Fig. 6.6(b). After the phase slip, the amplitude slowly approaches unity and the phase variation smears out, eventually giving rise to uniform oscillations. This scenario is in perfect agreement with the disappearance of phase flips in the CGLE under increasing global feedback intensity [37] (the destruction of phase flips by strong external forcing in the CGLE has also been observed [34]).



### 6.1.3 Asynchronous oscillations

Patterns with smooth spatial gradients of chemical variables can be induced by the feedback in the desynchronization region displayed in Fig. 6.1. Below the dashed lines in this region, asynchronous patterns develop from any initial condition. The duration of the desynchronization process diverges for feedbacks of vanishing intensity. Applying the transformation to local phase and amplitude variables, asymptotic asynchronous patterns established in this regime can be analyzed. Spatial profiles of  $R$  and  $\phi$  in such a pattern are shown in Fig. 6.7(a). It is found that only the local oscillation phase  $\phi$  is varying in this pattern, whereas the amplitude  $R$  is almost constant. This means that all local oscillations correspond to the same limit cycle. The phase profile shows smooth variation. When the size of the medium is varied in simulations, the pattern readjusts to the size of the medium, therefore lacking an intrinsic wavelength.

In the phase portrait representation of such a pattern, all points are distributed on the unit circle, see Fig. 6.7(b). However, not all possible phases are occupied, and the density of points increases towards the ends of the structure which correspond to the extrema of the phase profile. As time goes on, the structure rotates in the plane with constant velocity.

Under periodic boundary conditions, the total phase gradient along the pattern always adjusts to an integer multiple of  $2\pi$  given by the winding number of the initial phase distribution. For a nonzero winding number, the asymptotic spatial profile of the phase  $\phi$  is linear,

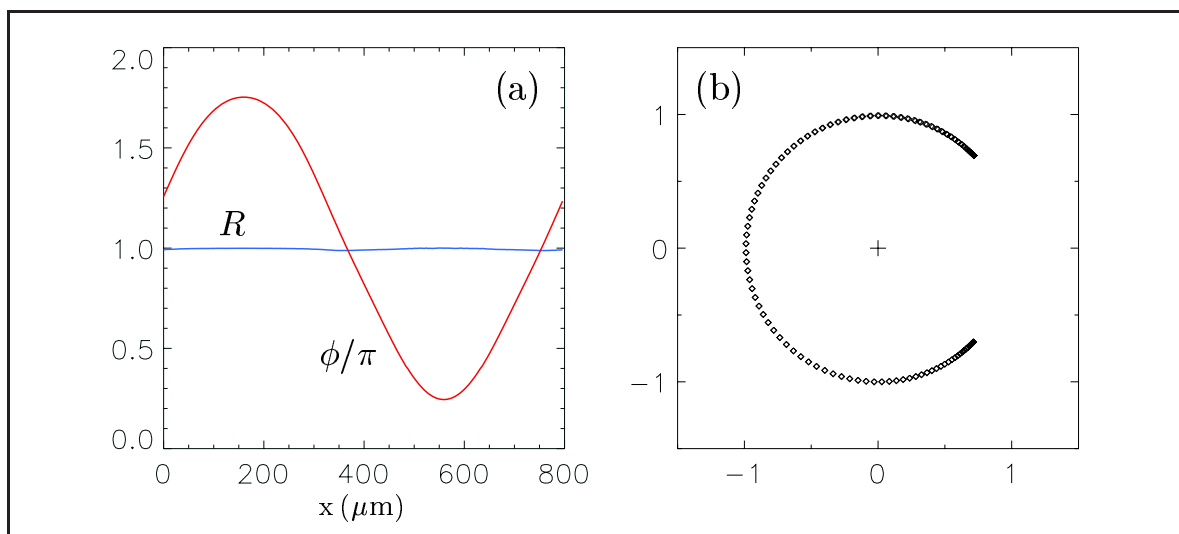


Figure 6.7: (a) Spatial dependence of the phase (red line) and the amplitude (blue line) and the phase portrait (b) of a pattern of asynchronous oscillations. A slightly perturbed uniform distribution was taken as initial condition. The same parameters as in Fig. 6.3(b).

so that the temporal shift between oscillations at different sites is proportional to their spatial distance. No-flux boundary conditions do not conserve the winding number. In the latter case, the final total phase gradient does not exceed  $2\pi$ .

An important consequence of the spatial desynchronization of oscillations is the accompanying breakdown of the global oscillations that generate the feedback signal. As shown in Fig. 6.8, the amplitude of the feedback signal decreases as the desynchronization gradually develops in the system. Thus, the global feedback effectively induces its own breakdown. It should be noted that the feedback oscillations do not, however, completely vanish in the asymptotic state. A small remaining feedback signal that compensates the synchronizing tendency of diffusion is needed to maintain the desynchronized state. Such desynchronization phenomena have previously been found in numerical investigations of the CGLE with global feedback [112].

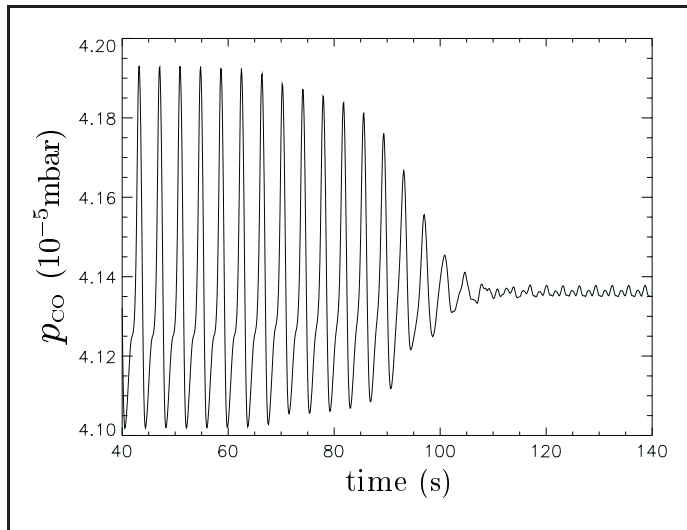


Figure 6.8: Breakdown of the feedback-induced CO pressure variations during the desynchronization of initially slightly perturbed uniform oscillations. The feedback parameters are  $\tau/T_0 = 0.781$  and  $\mu/p_0 = 0.048$ .

### 6.1.4 Cluster patterns

The third principal mechanism of feedback-induced pattern formation involves clustering of oscillations. The cluster regimes include a variety of qualitatively different patterns. Their common feature is the presence of a small number of synchronized domains, occupied by one of two possible oscillatory states. No intrinsic spatial wavelength of the domains is observed. In the following, different cluster solutions are divided into *amplitude clusters*, *phase clusters*, and *cluster turbulence*.

### Amplitude clusters

In amplitude clusters, not only the oscillation phase  $\phi$ , but also the oscillation amplitude  $R$  is different in the regions occupied by the two different states, as shown in Fig. 6.9(a). Thus, uniform oscillations within two different clusters correspond to different coexisting limit cycles of equal period. The phase shift between the oscillations in the two cluster states (about  $0.88\pi$  in the example shown) is constant, but depends on the feedback parameters. At the interface between two stationary cluster domains, the phase  $\phi$  is monotonously increased and the amplitude  $R$  undergoes small variations. The total size ratio of the domains that belong to each state is independent of the initial domain sizes and has a characteristic value that changes with the feedback parameters. The difference in the contributions to global oscillations coming from the two clusters results in period-doubled oscillations of the control signal, see Fig. 6.9(b). Amplitude clusters were previously seen in studies of the CGLE with global feedback [37, 114]. They were also investigated in the model of the CO oxidation reaction under intrinsic gas phase coupling [114, 151] and similar properties were then found.

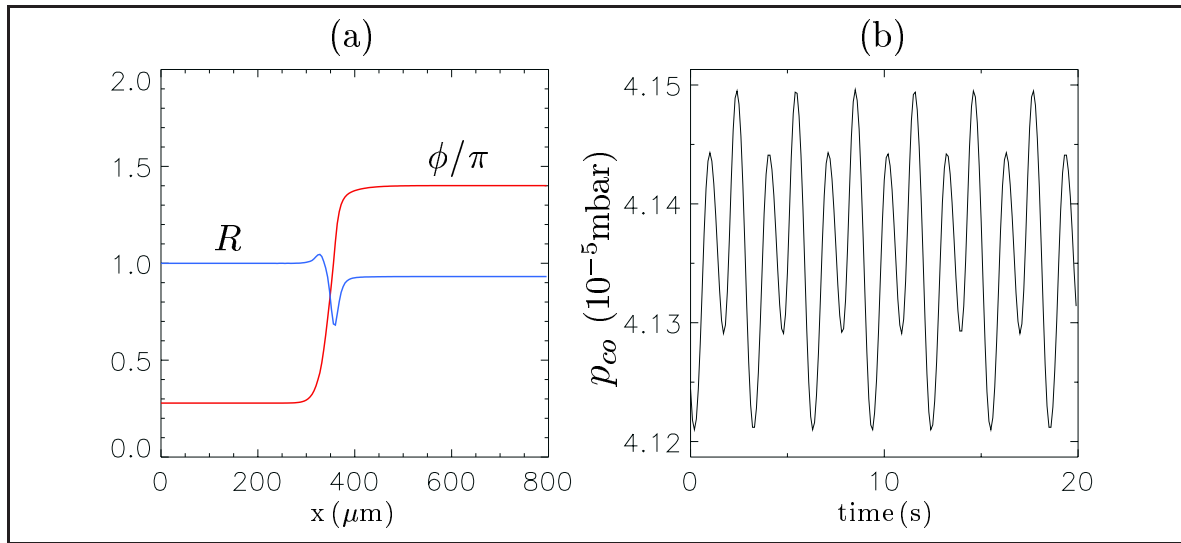


Figure 6.9: (a) Phase and amplitude profiles of amplitude clusters. The reference limit cycle for the variable transformation is chosen as the attractor of the cluster state with the higher amplitude. No-flux boundary conditions are used. Frame (b) shows global oscillations corresponding to the pattern in frame (a). The feedback parameters are  $\tau/T_0 = 0.045$  and  $\mu/p_0 = 0.072$ .

### Phase clusters

Phase clusters are characterized by equal oscillation amplitudes and a constant phase shift between the cluster states. The oscillations in both cluster states correspond now to the same limit cycle, but are of opposite phase. The phase fronts that separate different cluster domains exhibit rich behavior, as demonstrated below. At high feedback intensities, stationary phase clusters prevail, see Fig. 6.10(a) for a space-time diagram. A blue/green/red/yellow color map, shown on the right in Fig. 6.10, is used here and throughout this chapter. Blue color corresponds to low values of the shown variable (here the phase  $\phi$ ), and yellow color denotes high values. Green and red color represent intermediate levels.

The asymptotic spatial formation of the domains in the standing cluster pattern shown in Fig. 6.10(a) depends on the initial conditions. However, the total fraction of the medium occupied by the domains of each cluster is balanced, a phenomenon which, following Ref. [103], is called *phase balance*. When a simulation is started with a different initial size ratio, the fronts between the cluster domains slowly drift and finally come to rest in the state of phase balance. As a consequence, the average that generates the feedback signal is periodic and resonantly oscillates with a frequency twice larger than that of the periodic local oscillations inside the cluster domains.

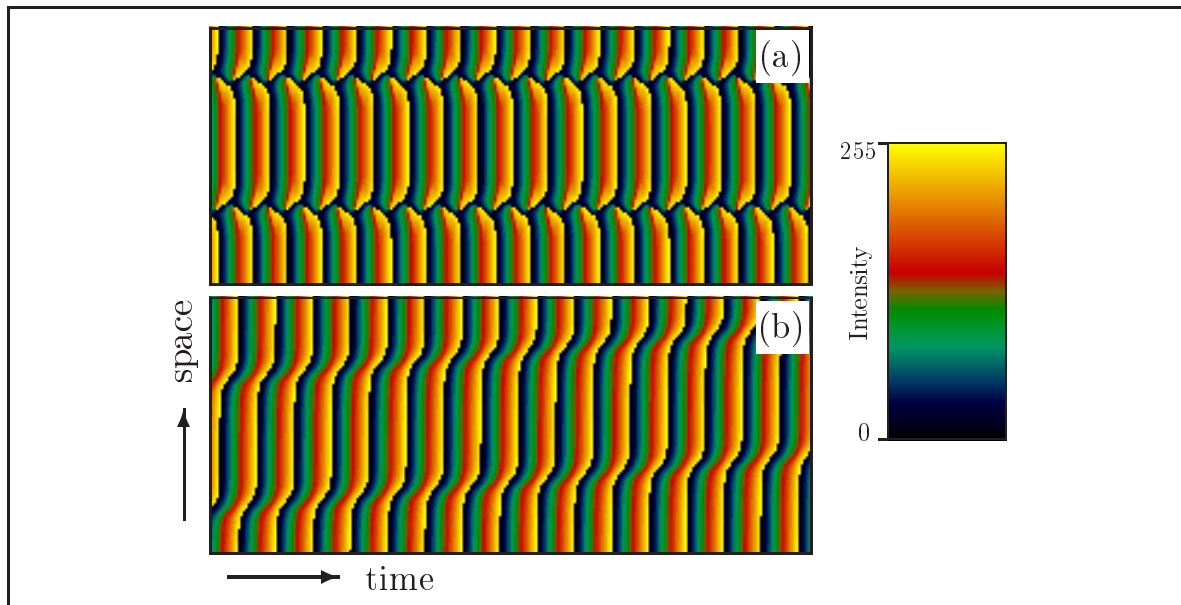


Figure 6.10: Phase clusters with (a) stationary (Ising) phase fronts and (b) traveling (Bloch) phase fronts. Both diagrams display the oscillation phase  $\phi$  in a time interval of 50 s, using the color map shown on the right. The system size is 0.4 mm. The values of the parameters  $\tau/T_0$  and  $\mu/p_0$  are, respectively, (a) 0.105, 0.241, and (b) 0.120, 0.096.

### Bifurcation to traveling phase clusters

Stationary phase clusters can undergo a transition to traveling clusters, an example of which is shown in Fig. 6.10(b). Periodic boundary conditions are necessary for the observation of such propagating patterns, because they preserve the size ratio between the clusters. This transition is related to a symmetry-breaking bifurcation known as the nonequilibrium Ising-Bloch bifurcation [32] (cf. Section 3.1.2), that leads to fronts traveling with constant velocity. The two branches of this pitchfork bifurcation correspond to counter-propagating fronts with equal absolute velocity and opposite sign. The dependence of the absolute velocity of traveling phase clusters on the feedback intensity at a fixed delay is shown in Fig. 6.11. It is seen that a bifurcation from stationary (Ising) fronts to traveling (Bloch) fronts occurs when the feedback intensity is decreased.

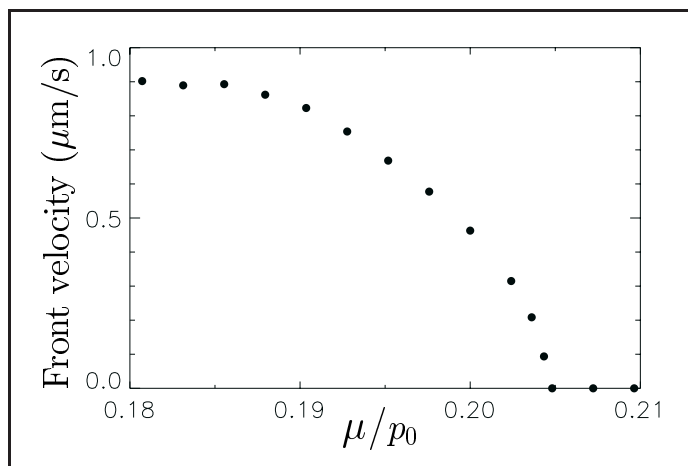


Figure 6.11: Long-time average of the phase front velocity in cluster patterns as function of the feedback intensity. The data points were obtained numerically with a system size equal to 0.4 mm. The delay time is kept constant,  $\tau/T_0 = 0.105$ .

It is interesting to compare the phase and amplitude properties of oscillations in stationary and traveling phase-cluster patterns. The phase portraits of such patterns are shown in Fig. 6.12. In the stationary cluster pattern displayed in Fig. 6.12(a), the two cluster states correspond to the ends of the S-shaped structure where the points accumulate. The other points in this structure correspond to the front which separates the clusters. Note that the S-shaped structure goes through the origin of the plane, i.e. there is a point inside the front where the oscillation amplitude  $R$  vanishes. At this point the phase  $\phi$  undergoes a jump of  $\pi$ .

At the transition to traveling Bloch fronts a topological bifurcation is observed in the phase portrait. When the bifurcation occurs, the S-shaped curve splits into two different branches that connect the two cluster states. Farther away from the bifurcation point, the fronts between the cluster states are mapped almost to a circle, as shown in Fig. 6.12(b). The phase  $\phi$  undergoes a continuous rotation with a total of  $\pi$  when traversing such a Bloch

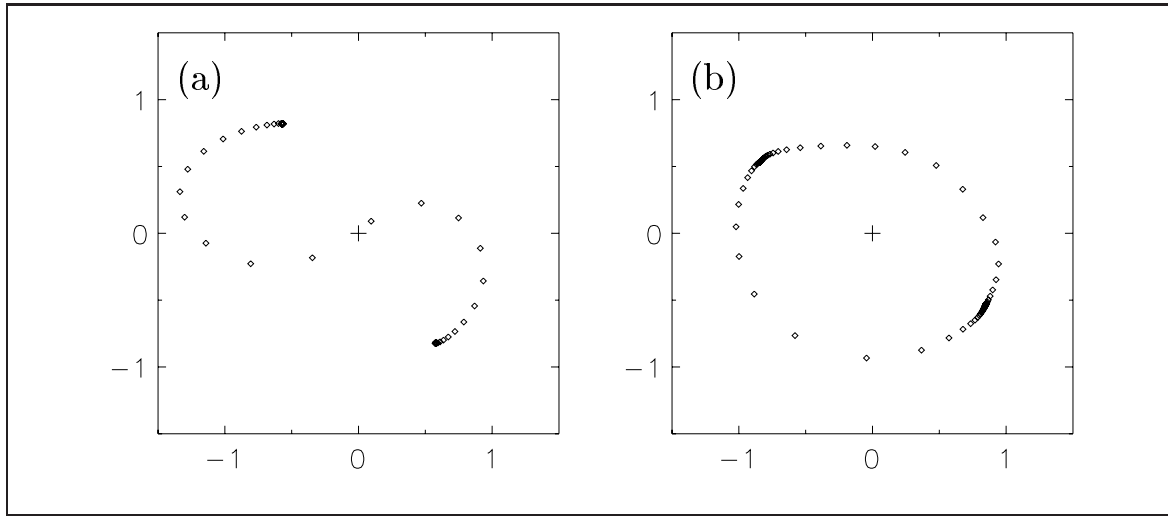


Figure 6.12: Phase portraits of cluster patterns with (a) a stationary Ising phase front and (b) traveling Bloch phase fronts. The values of the parameters  $\tau/T_0$  and  $\mu/p_0$  are, respectively, (a) 0.045, 0.289, and (b) 0.120, 0.096.

front, whereas  $R$  shows only small modulations. By application of the transformation to phase and amplitude variables, it is thus found that the properties of such Ising and Bloch fronts are close to those found for the amplitude equation of oscillatory media under external forcing [32].

### Bifurcation to oscillating phase clusters

Furthermore, another phase front instability has been observed: a Hopf bifurcation of a front that separates two clusters. The origin of this bifurcation is an instability of the phase balance that gives rise to periodic oscillations of the cluster size ratio. As a consequence, cluster fronts periodically change their spatial position, see Fig. 6.13. The front position can be defined as the location within the front where the amplitude  $R$  is minimal. The period of the front oscillations comprises several local oscillations.

Figure 6.14 shows the dependence of the amplitude of front oscillations on the feedback intensity at a constant delay. The bifurcation from a stationary front to an oscillating cluster front occurs when the feedback intensity is decreased. The parabolic fit (solid line in Fig. 6.14) is in good agreement with the numerical data close to the bifurcation point where front oscillations are harmonic. Hence, this is a supercritical Hopf bifurcation for the fronts. At larger distances from the bifurcation point, the front oscillations become strongly anharmonic and zig-zag shaped, see Figs. 6.13(a) and 6.13(b). The spatial amplitude profile of such an oscillating front is time-dependent. At the turning points of the front the amplitude

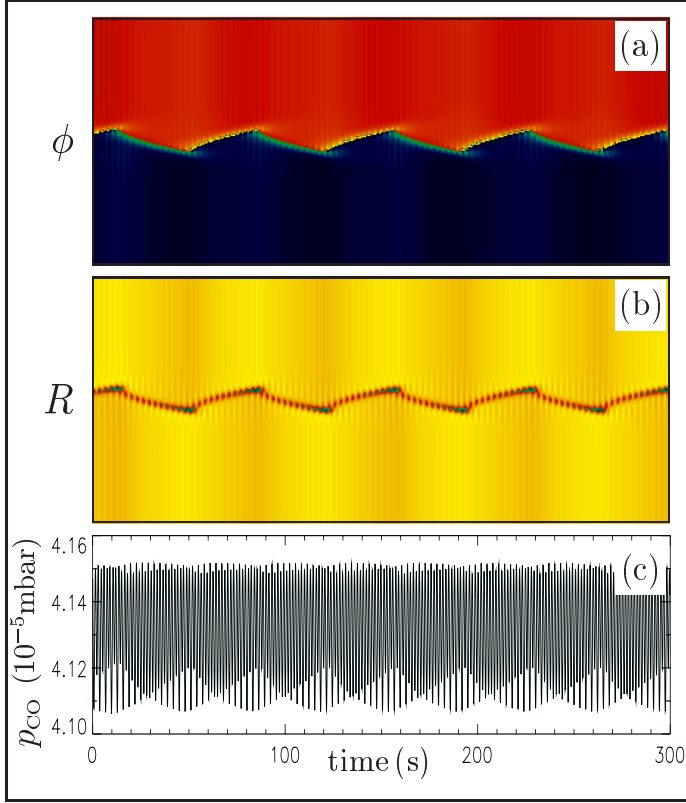


Figure 6.13: Space-time plot of front oscillations in a cluster pattern with no-flux boundaries. (a) Oscillation amplitude  $R$  and (b) phase  $\phi$  in a time interval of 500 s. The phase distribution is displayed in a coordinate frame rotating with the period of the reference limit cycle. The corresponding quasiperiodic feedback signal is shown in frame (c). The feedback parameters are  $\tau/T_0 = 0.105$  and  $\mu/p_0 = 0.096$ .

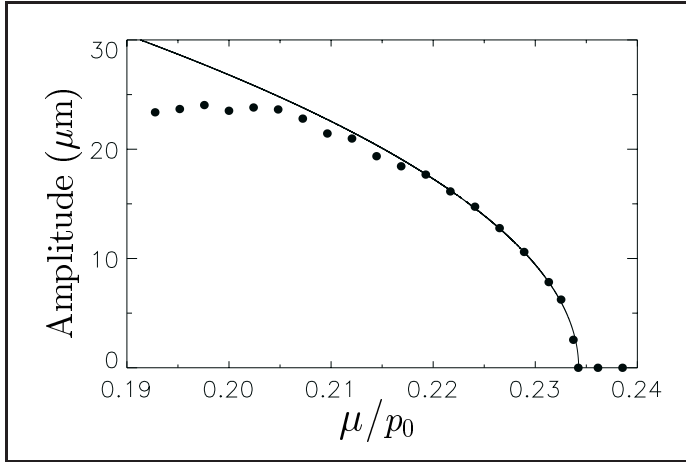


Figure 6.14: Oscillation amplitude of a cluster front as a function of the feedback intensity. The data points are obtained numerically for a system size equal to 0.4 mm and no-flux boundary conditions. The solid line is a parabolic fit of the data points close to the bifurcation point. The delay time is kept constant,  $\tau/T_0 = 0.105$ .

$R$  drops down and nearly vanishes. The control signal generated by two oscillating clusters becomes quasiperiodic after the Hopf bifurcation, see Fig. 6.13(c). The turning points of the phase front correspond to the points of maximal amplitude in the feedback oscillations. The change in the control signal provides a feedback on the phase front and hence is responsible for its turnaround. Note that the local oscillations in Fig. 6.13(a) are also slightly quasiperiodic due to the quasiperiodicity of the driving feedback signal. Though the local amplitude differs slightly in the two oscillating cluster states, they here still are classified as phase clusters because they smoothly originate from stationary phase clusters and their phase and



amplitude properties are similar. Oscillating phase clusters have previously also been found in the periodically forced CGLE [82].

### Cluster turbulence

Starting from strongly anharmonic front oscillations, a suitable change of the feedback parameters leads to turbulent phase front behavior. An example of such irregular front behavior is shown in Fig. 6.15, where a front separating two  $\pi$ -shifted clusters branches out in a cascade of reproductions. The cluster turbulence does not spontaneously develop from a completely uniform oscillating state, i.e., a sufficiently strong local perturbation is needed to initiate the cascade. The fronts not only reproduce, but also can die out. Once initiated, the cluster turbulence can thus either spread over the whole medium, or die out after some time.

The velocities of traveling fronts in this turbulent regime are almost constant. A front travels for some time, until an amplitude defect with vanishing amplitude  $R$  develops inside it. As a result, the front may split or die out. Phase fronts also sometimes emerge from smaller heterogeneities in the amplitude and the phase without directly originating from an amplitude defect. The irregular front behavior leads to turbulent deviations from the cluster states. Hence, the local oscillations are synchronous only inside cluster regions that were not

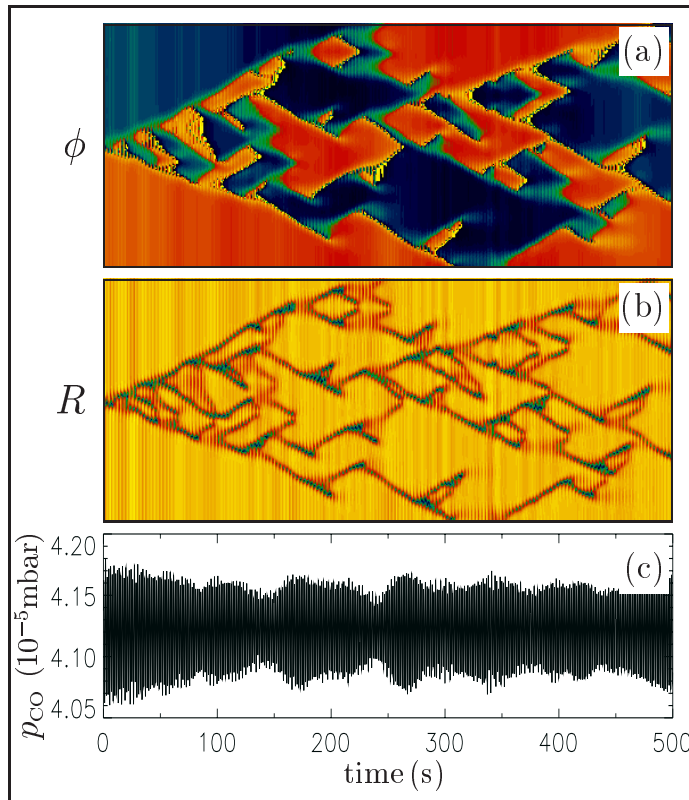


Figure 6.15: *Space-time plots of the reproduction cascade in a turbulent cluster pattern with no-flux boundaries. (a) Oscillation amplitude  $R$  and (b) phase  $\phi$  in a time interval of 500 s. The phase distribution is displayed in a coordinate frame rotating with the period of the reference limit cycle. The corresponding chaotic feedback signal is shown in frame (c). The feedback parameters are  $\tau/T_0 = 0.126$  and  $\mu/p_0 = 0.193$ .*



visited by a front for several oscillation cycles. The global oscillations are chaotic in this regime, see Fig. 6.15(c).

Figure 6.16 shows the existence regions of different cluster patterns at small delays. It has been found that the type of the developing cluster pattern strongly depends on the initial and boundary conditions. The dashed line in Fig. 6.16 indicates the stability boundary of uniform oscillations with respect to small perturbations. On the right side from the dashed line both cluster patterns and uniform oscillations are possible, depending on the initial conditions. Note that cluster turbulence always coexists with uniform oscillations. The boundary conditions are important. For instance, in the region in the diagram where amplitude clusters are present, they were typically found for no-flux boundary conditions. For periodic boundary conditions, special initial conditions were needed here to obtain amplitude clusters, and traveling phase clusters are usually instead found. In the phase cluster region, for most parameter values the front behavior strongly depends on both the initial and the boundary conditions. Stationary phase clusters are only found above the dotted line in the diagram.

As already mentioned, traveling clusters require periodic boundary conditions that maintain the phase balance. For the same parameter values, no-flux boundaries either lead to the

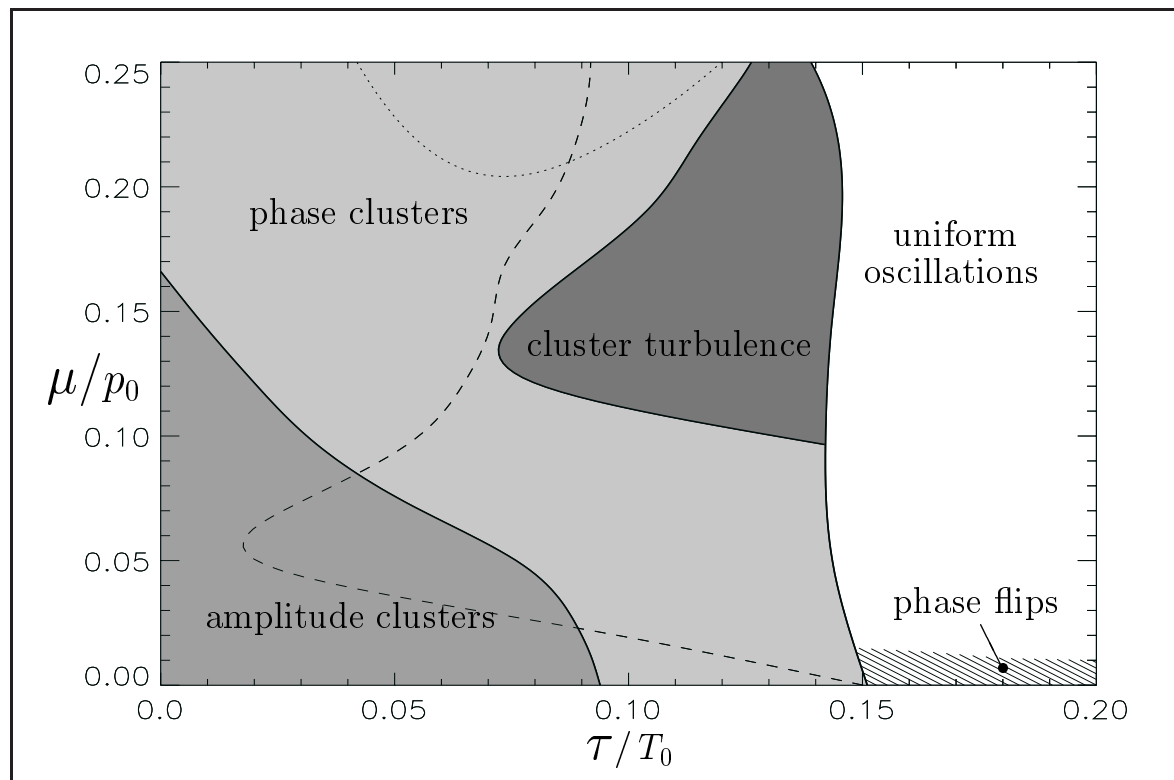


Figure 6.16: Approximate existence regions of different cluster patterns at small delay times.

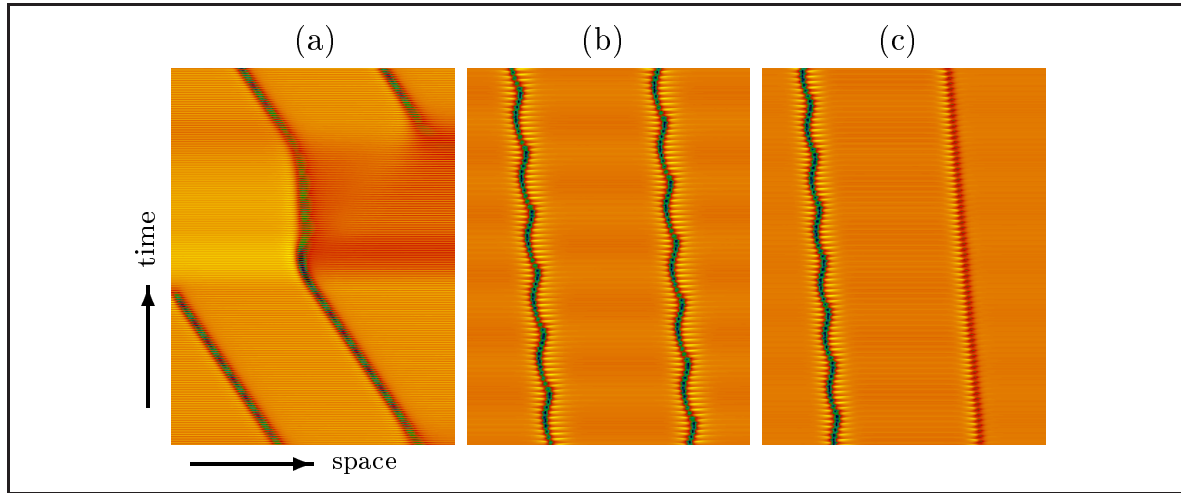


Figure 6.17: Space-time plots of the amplitude in different cluster patterns. Traveling phase clusters (a) under no-flux boundary conditions, the time interval is 500 s. Drifting breathing clusters (b) and clusters with different behavior of the two fronts (c) in a system with periodic boundary conditions, each within the time interval of 200 s. The values of the parameters  $\tau/T_0$  and  $\mu/p_0$  are, respectively, (a) 0.114, 0.072, (b) 0.030, 0.193, and (c) 0.039, 0.193.

formation of stationary amplitude clusters, or to the front behavior shown in Fig. 6.17(a). When the first front collides with the left boundary, further movement of the second front would lead to phase imbalance. Instead, during a transient process, where in a part of the medium the oscillations strongly deviate from the former cluster states, a new cluster front is created. Again, both clusters travel with constant velocity until the behavior repeats at the next front collision with the boundary. Figure 6.17(b) shows an example of breathing traveling clusters – this pattern develops when a traveling cluster undergoes a secondary Hopf bifurcation. As shown in Fig. 6.17(c), even more complex situations, where one of the fronts is steadily traveling and the other front is oscillating while traveling, are possible. The global oscillations of all three patterns in Fig. 6.17 are quasiperiodic.

### 6.1.5 Patterns in two space dimensions

Feedback-induced pattern formation in equations (5.1)–(5.4) has also been numerically explored in two space dimensions. For the two-dimensional simulations, a slightly different CO base pressure has been chosen,  $p_0 = 4.19 \times 10^{-5}$  mbar, in order to avoid a feedback-caused pressure drift into the regime of diffusion-induced turbulence, which in two dimensions occurs below  $p_0 \approx 4.15 \times 10^{-5}$  mbar. The other parameters are the same as in the one-dimensional case, except for  $u_{\text{ref}} = 0.4484$  which again corresponds to the unstable steady state. Unless stated otherwise, the system size is  $0.8 \times 0.8 \text{ mm}^2$  and no-flux boundary

conditions are imposed at all boundaries.

Figure 6.18 shows four examples of different two-dimensional patterns. In the upper and lower row, the spatial distributions of the oscillation phase and amplitude are displayed, respectively. In absence of feedback, uniform oscillations are stable, but a rotating spiral wave can be produced by an appropriate choice of the initial conditions, see Fig. 6.18(a). The oscillation amplitude vanishes in the spiral core and the phase changes continuously when traversing the spiral arms. By application of feedback and variation of its parameters, the spiral wave can be suppressed and uniform oscillations recovered (not shown in Fig. 6.18). Phase-flip waves [Fig. 6.18(b)], asynchronous oscillation patterns [Fig. 6.18(c)], or (quasi) stationary cluster patterns [Fig. 6.18(d)] could also be induced by appropriate feedbacks. The properties of uniform oscillations, phase flips, and desynchronized oscillations are similar to those of their one-dimensional counterparts.

The development of the asynchronous pattern in Fig. 6.18(c) from slightly perturbed uniform initial conditions leads to the breakdown of global oscillations. As in the one-dimensional case, the final asynchronous pattern is characterized by a constant amplitude

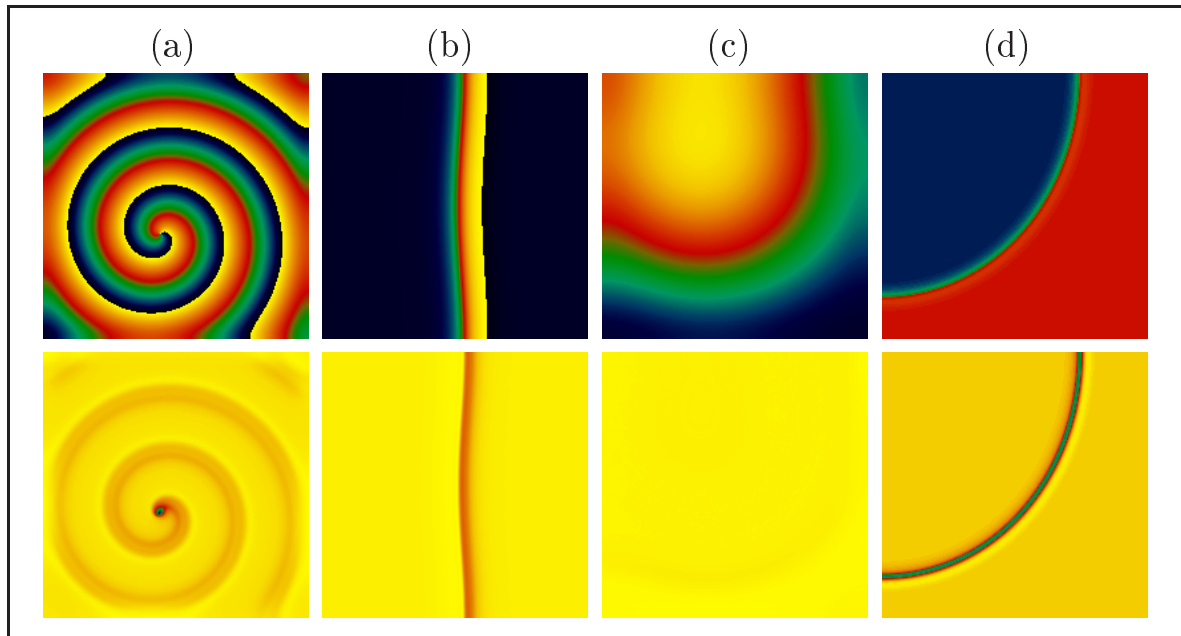


Figure 6.18: Two-dimensional patterns: (a) a spiral wave in absence of feedback, (b) a phase flip, (c) asynchronous oscillations, and (d) a cluster pattern. Snapshots of the oscillation phase (top row) and amplitude (bottom row) distributions are displayed. The system size is  $0.8 \times 0.8 \text{ mm}^2$  for each pattern, except for the pattern (b) where it is  $1.6 \times 1.6 \text{ mm}^2$ . The values of the parameters  $\tau/T_0$  and  $\mu/p_0$  are, respectively, (a) 0, 0, (b) 0.192, 0.010, (c) 0.768, 0.024, and (d) 0.067, 0.119.

and slow phase gradients. In the desynchronization regime, the feedback cannot destroy spiral waves and they continue to represent a stable solution.

The phase cluster pattern in Fig. 6.18(d) consists of two  $\pi$ -shifted phase states separated by an almost stationary phase front. The clusters evolved from a nonuniform initial distribution. After the quick formation of the clusters, a slow drift of the front occurs, tending to minimize the front curvature while preserving the phase balance. The effect of the front curvature is the only essential difference compared to the corresponding one-dimensional stationary phase cluster pattern shown in Fig. 6.10(a). Stationary amplitude clusters were also observed in two-dimensional simulations and exhibited similar behavior as in the one-dimensional case.

After a bifurcation to traveling phase fronts, counter-propagating front parts can develop in a two-dimensional pattern (as previously noticed in externally forced oscillatory media [32], see Section 3.1.2). The pattern developing under such conditions is shown in Fig. 6.19. The initial conditions in the upper and lower half of the originally straight front were chosen to correspond to the two branches of the pitchfork bifurcation, see Fig. 6.19(a). Because the two ends of the front propagate in opposite directions, a spiral wave develops in the central part [Fig. 6.19(b)-(f)], and later spreads out over the whole medium. This process is accompanied by the breakdown of the global oscillations, see Fig. 6.19(g). As the spiral grows, the fraction of the medium occupied by the fronts with rapid phase variation

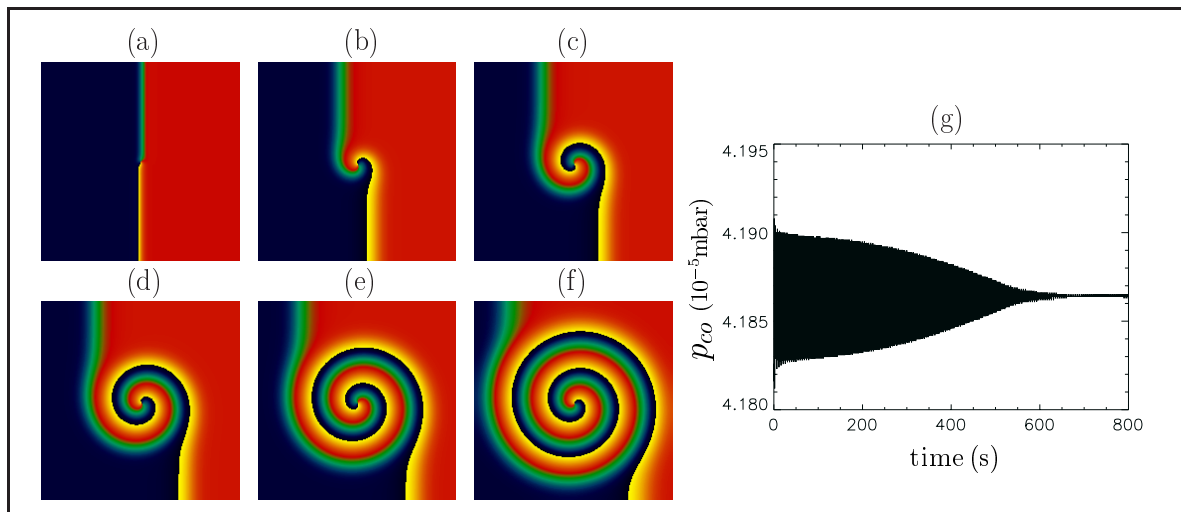


Figure 6.19: (a)-(f) Formation of a spiral wave from a cluster pattern with counter-propagating front parts. Consecutive snapshots of the oscillation phase  $\phi$  are shown at equal time intervals of 96 s. (g) Breakdown of the control signal during the pattern evolution. The parameter values are  $\tau/T_0 = 0.067$  and  $\mu/p_0 = 0.024$ .

slowly increases at the expense of the areas occupied by the two uniform phase states. Eventually, they become too small to generate a feedback signal sufficient to maintain the clusters. Therefore, the nonequilibrium Ising-Bloch bifurcation provides an additional scenario for the breakdown of the global feedback. The final state is characterized by a spiral wave with continuous phase distribution and nearly vanishing global oscillations, as in absence of global feedback.

The pattern displayed in Fig. 6.20 was obtained with feedback parameters corresponding to the case of cluster front oscillations in one space dimension. A nonuniform phase and amplitude distribution was taken as initial condition. The frames (a) and (b) show the phase (top row) and amplitude (bottom row) distributions at time moments separated by half the oscillation period. Instead of front oscillations, which are seen in this case in the one-dimensional system and are accompanied by quasiperiodic variations of the global control signal, a different kind of pattern is observed in two dimensions. The area occupied by each of the clusters in Fig. 6.20 is almost balanced and no significant oscillations of the fronts take place. The global oscillations are almost periodic here. The front separating the two clusters is broken into parts (see the bottom row in Fig. 6.20). As time goes on, the amplitudes in different front parts periodically drop down at opposite oscillation phases. On a large timescale of several hundred oscillation periods, weak drift of the clusters and slow gradual variation of their shapes are observed. The splitting of the front into different parts is a two-dimensional

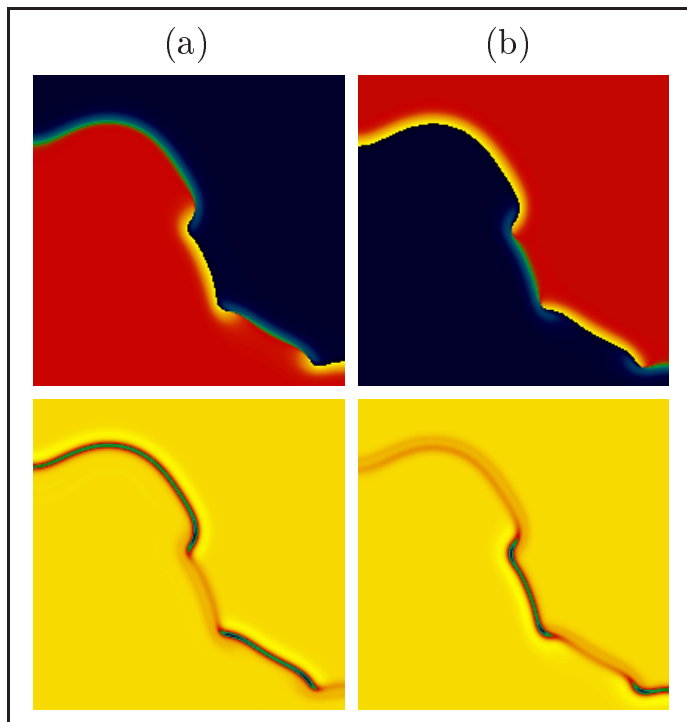


Figure 6.20: Snapshots of the oscillation phase (top row) and amplitude (bottom row) distribution in a cluster pattern with time-dependent front profile. The time interval between the snapshots (a) and (b) is half of the oscillation period in the clusters. The parameter values are  $\tau/T_0 = 0.067$  and  $\mu/p_0 = 0.072$ .

phenomenon which is typically observed starting from nonuniform initial conditions. However, if a simulation is started with a straight front, it remains stable with respect to small perturbations and shows periodic oscillations, as in the corresponding one-dimensional case.

When cluster fronts show irregular motion in one space dimension, the respective two-dimensional clusters also exhibit complex turbulent evolution. As an example, two subsequent snapshots of a turbulent cluster pattern are shown in Fig. 6.21 (top and bottom rows again correspond to the phase and amplitude distributions). Each cluster consists of different patches that continuously vary their shape while the separating fronts propagate through the medium. The front propagation occurs at an almost constant velocity in the planar front parts. Turbulence is maintained in this system through repeated emergence of bubble-like domains with the opposite phase inside a cluster region. These bubbles grow for a few oscillation cycles and eventually merge with the larger cluster patches. On the other hand, cluster patches can also shrink and disappear. New cluster spots usually originate at locations that were previously visited by the fronts, where amplitude and phase heterogeneities were left. Uniform oscillations are stable in this parameter region. To initiate a turbulent cascade, sufficiently strong local perturbations must be applied to the uniform state. The turbulent formation of cluster spots is different from the birth of spots through self-replication that was previously reported in bistable systems [156].

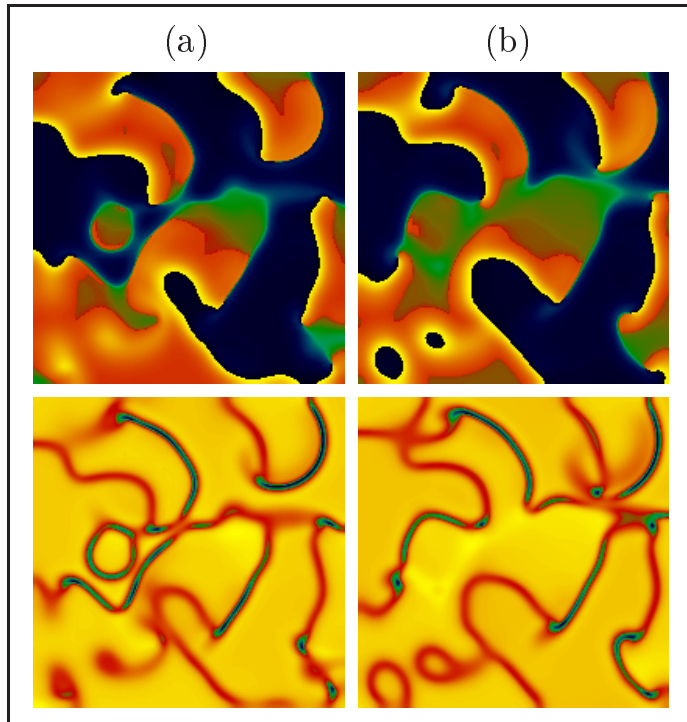


Figure 6.21: *Turbulent cluster pattern. The two consecutive snapshots of the oscillation phase (top row) and amplitude (bottom row) distributions are separated by a time interval of two oscillation periods. The parameter values are  $\tau/T_0 = 0.067$  and  $\mu/p_0 = 0.024$ .*



In summary, by means of numerical simulations it was found that pattern formation in the realistic model of CO oxidation on Pt(110) could be efficiently manipulated by implementation of a global delayed feedback. In the case studied so far, when uniform oscillations were stable in absence of feedback, variation of the feedback intensity and the time delay allowed to produce various structures, including phase flips, asynchronous oscillations, amplitude clusters, and phase clusters with complex front properties.

### 6.1.6 Comparison with the normal form approach

The amplitude and phase description of the observed feedback-induced patterns provides a link to the previous studies [36, 37, 112–114] performed in the framework of the complex Ginzburg-Landau equation with global feedback. This general model is strictly valid only near the soft onset of oscillations at a supercritical Hopf bifurcation and when the delay in the feedback loop is not too large. The simulations of the realistic model of CO oxidation have been performed at parameter values not close to a supercritical Hopf bifurcation and therefore, it is interesting to compare the behavior in both systems to see whether the predictions of the CGLE still qualitatively hold.

For comparison, additional simulations have been conducted using the CGLE with global feedback [equation (3.7)]. One-dimensional patterns resulting from such simulations are displayed in Fig. 6.22. The used parameter values of  $\beta$  and  $\varepsilon$  have been derived from the CO oxidation model with the help of M. Ipsen. They were numerically determined from equations (5.1)–(5.3) at a CO partial pressure of  $p_{\text{CO}} = 4.1996 \times 10^{-5}$ , which corresponds to the critical value associated with the nearest supercritical Hopf bifurcation.

By using these parameters and additionally including global feedback according to equation (3.7), the patterns shown in Figs. 6.22(a) and 6.22(b), representing a phase flip and asynchronous oscillations, respectively, have been generated. Note that the amplitude and phase plots obtained by the variable transformation in the CO oxidation model with non-harmonic oscillations are quite similar to the respective plots for the CGLE with global feedback [compare Fig. 6.22(a) with Fig. 6.4, and Fig. 6.22(b) with Fig. 6.7]. The amplitude clusters observed in the CO oxidation model also resemble the cluster solutions in the amplitude equation [114] (not shown in Fig. 6.22).

Phase clusters could only be observed in the CGLE with global feedback when the feedback term  $\mu e^{i\chi} \bar{A}$  was replaced by a term accounting for higher-order self-resonance, such

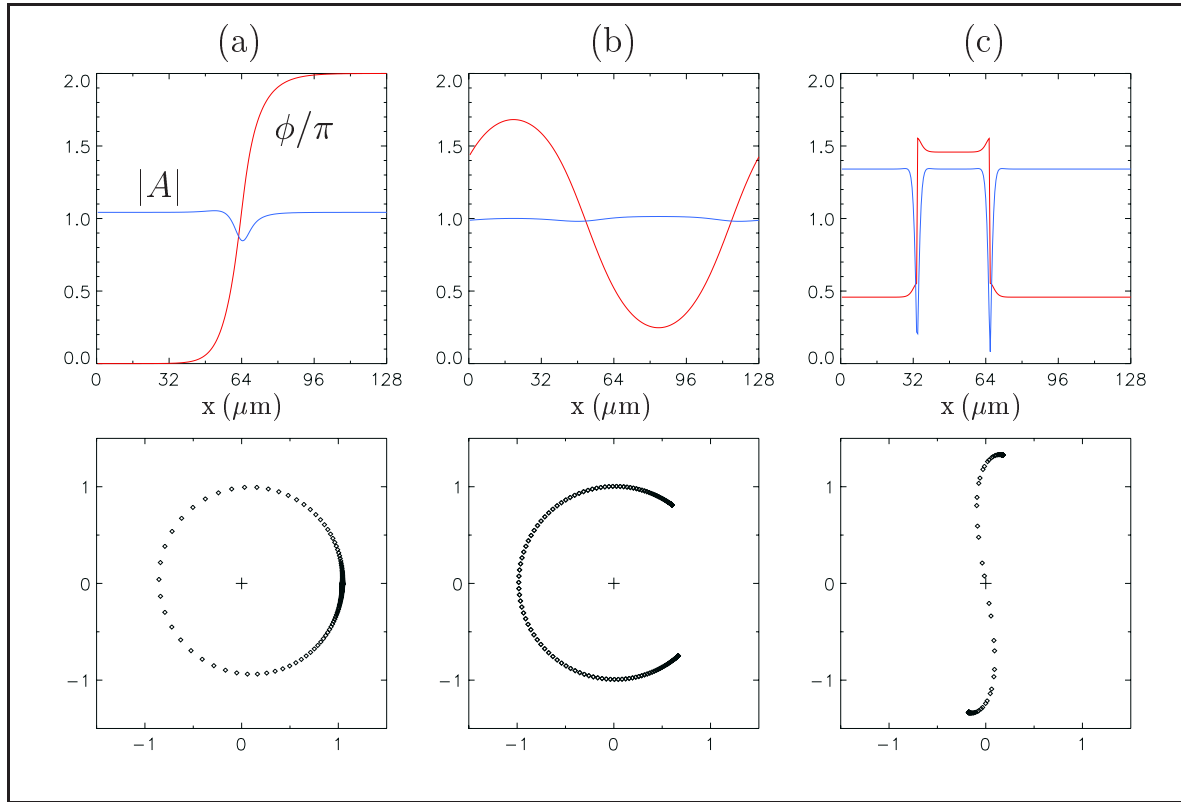


Figure 6.22: One-dimensional patterns in the CGLE with global feedback. In the top row, for each pattern the profiles of the amplitude modulus  $|A|$  (blue lines) and the phase  $\phi = \arg(A)$  (red lines) are displayed. The bottom row shows the corresponding phase portraits. Patterns (a) and (b) result from numerical simulation of equation (3.7), while for pattern (c) equation (6.1) was used. The parameters are  $\beta = -0.76$  and  $\varepsilon = -2.62$  (and hence correspond to the Benjamin-Feir stable case  $1 + \varepsilon\beta > 0$ ), and (a)  $\mu = 0.1, \chi = 0$ ; (b)  $\mu = 2.0, \chi = 1.0$ ; and (c)  $\mu_2 = 2.0, \chi_2 = 1.85$ .

that the equation read

$$\frac{\partial A}{\partial t} = A - (1 + i\beta)|A|^2 A + (1 + i\varepsilon)\nabla^2 A + \mu_2 e^{i\chi_2} \bar{A}^2 A^*. \quad (6.1)$$

Here,  $A^*$  denotes the complex conjugate of  $A$ . A phase cluster solution obtained with equation (6.1) is displayed in Fig. 6.22(c). Depending on the feedback parameters, stationary or traveling phase clusters were seen in numerical simulations. However, phase balance was absent in such patterns, and they transformed into amplitude clusters when both feedback terms were included. Thus, with the exception of phase clusters, the principle effects of global delayed feedback on stable uniform oscillations in the model of CO oxidation are in good agreement with the behavior found in the CGLE with global feedback, even though oscillations were not harmonic in the realistic model.



## 6.2 Controlling chemical turbulence

In the following, the effects of global delayed feedback are further studied in a case where the system shows chemical turbulence in absence of feedback. As it is shown below, this leads to the appearance of several new phenomena.

In the model of CO oxidation, chemical turbulence is found in a wide range of control parameters [151]. To obtain such turbulence, in the following the values of the oxygen partial pressure ( $p_{\text{O}_2} = 1.30 \times 10^{-5}$  mbar) and the CO partial pressure ( $p_0 = 4.81 \times 10^{-5}$  mbar) are changed with respect to the parameters used in Section 6.1. The steady state value of the CO coverage is also adjusted,  $u_{\text{ref}} = 0.3358$ . All other model parameters, given in Table 5.1, are left unchanged. Unless stated otherwise, the system size is 0.8 mm for one-dimensional and  $0.4 \times 0.4 \text{ mm}^2$  for two-dimensional media, and periodic (no-flux) boundary conditions are imposed on one-dimensional (two-dimensional) systems.

### 6.2.1 Amplitude turbulence

At first, the behavior exhibited by model (5.1)–(5.4) in absence of feedback ( $\mu = 0$ ) is considered. At the above specified parameters, an isolated system element performs non-harmonic limit cycle oscillations of period  $T_0 = 2.73$  s. However, due to a destabilizing effect of the diffusive coupling between the elements, uniform oscillations are now unstable with respect to small perturbations and chemical turbulence spontaneously develops.

A space-time diagram showing the evolution of the variable  $u$  during the transition from nearly uniform oscillations to turbulence is displayed in Fig. 6.23(a). The initially small perturbations of the uniform state quickly grow, thereby destroying spatial correlations between distant system elements. In the fully developed turbulent state, the spatially averaged values of all model variables are almost constant and show only small random fluctuations.

To further characterize the observed turbulent state, the variable transformation described in Section 6.1 is employed. A space-time diagram of the amplitude field during the transition to turbulence is shown in Fig. 6.23(b). It is seen that in the state of developed turbulence, multiple defects are present in the medium. Such objects appear as dark blue regions in Fig. 6.23(b) and are characterized by a significantly decreased oscillation amplitude. This state is reminiscent of what has been called *amplitude turbulence* in the complex Ginzburg-Landau equation (cf. Section 2.3), and so this term shall also be used here.

At the same parameter values, uniform oscillations are also unstable in two-dimensional systems. Snapshots of the resulting spatial distributions of CO coverage, phase, and am-

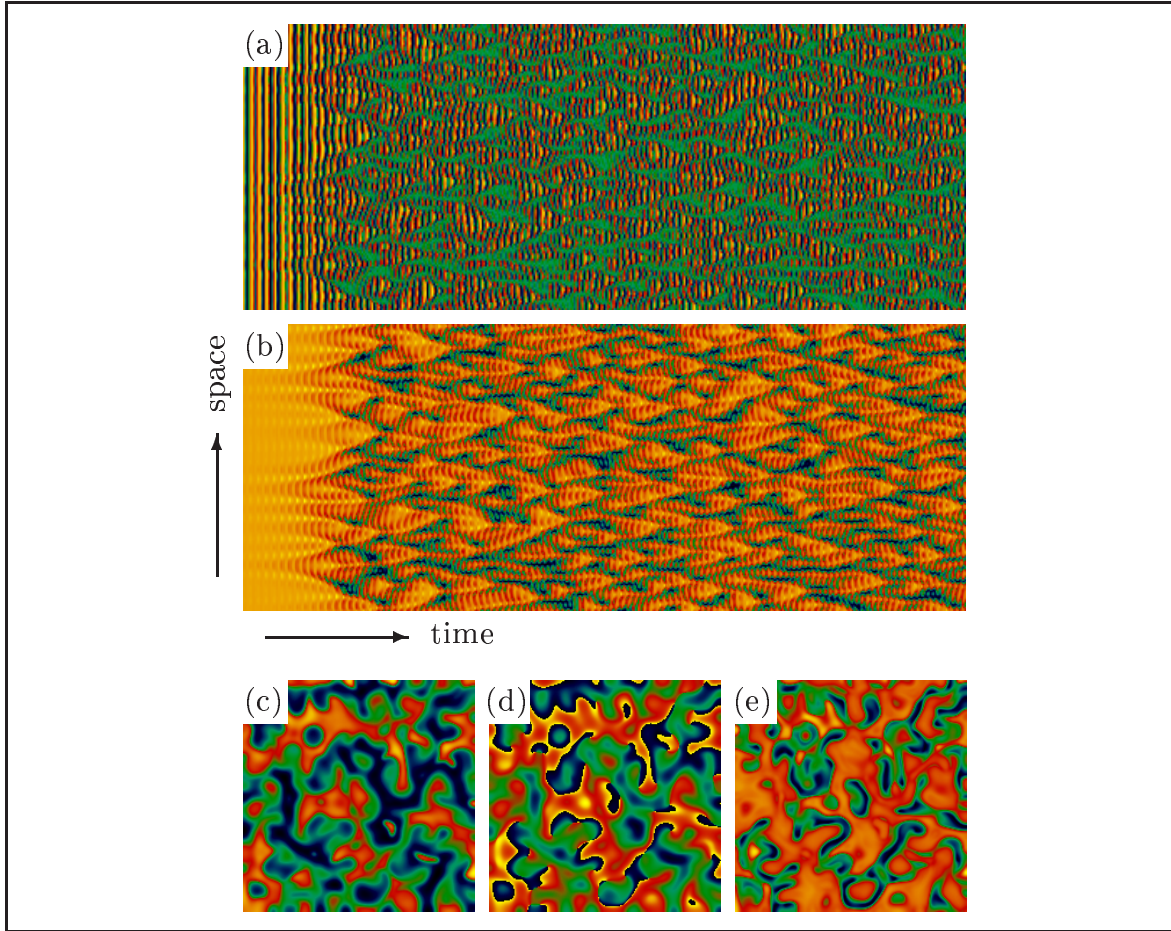


Figure 6.23: Amplitude turbulence in model (5.1)–(5.4) in absence of feedback ( $\mu = 0$ ). In frames (a) and (b), space-time diagrams of the CO coverage  $u$  and the oscillation amplitude  $R$ , respectively, are shown for a one-dimensional system. The shown time interval is 150s. Frames (c), (d), and (e) display snapshots of  $u$ , phase  $\phi$ , and amplitude  $R$ , respectively, in a two-dimensional system. The parameter values are  $p_{\text{O}_2} = 1.30 \times 10^{-5}$  mbar and  $p_0 = 4.81 \times 10^{-5}$  mbar. Other parameters are given in Table 5.1.

plitude are displayed in Figs. 6.23(c), (d), and (e), respectively. The two-dimensional spatiotemporally chaotic state is characterized by the presence of extended regions of decreased oscillation amplitude (*strings*). Perpendicular to such objects, the oscillation phase strongly varies in space. The two ends of a string usually correspond to topological defects in the phase field. Fragments of spiral waves are only rarely visible in such a state of developed amplitude turbulence. The shown behavior represents a typical example of the turbulent state found in a wide range of model parameters. At different parameter values, spiral-wave turbulence similar to the state shown in Fig. 2.5(b) is also possible.

### 6.2.2 Overview of feedback effects

In a first series of numerical simulations, global delayed feedback has been switched on only after amplitude turbulence had fully developed in the system. The results of such simulations, performed on one-dimensional systems, are summarized in Fig. 6.24(a). Different types of stable regimes, represented by different shading, are reached after transients.

Fig. 6.24(a) shows that, if the feedback intensity is sufficiently large, global delayed feedback allows to suppress amplitude turbulence and induces uniform oscillations in a wide range of delays (light gray-shaded regions). The minimal value of  $\mu$  needed to stabilize uniform oscillations, and therefore the efficiency of the feedback, strongly depend on the choice of  $\tau$ . When the feedback intensity is fixed at an intermediate level, several synchronization windows alternate with turbulent zones upon variation of the delay. Note that at small delays in the approximate range  $0.03 < \tau/T_0 < 0.10$ , turbulence can be suppressed at relatively low values of the feedback intensity, but the feedback fails to stabilize uniform oscillations at higher values of  $\mu$ . It is further seen in Fig. 6.24(a) that in case of even smaller delays,  $\tau/T_0 < 0.03$ , the suppression of turbulence is impossible for realistic values of  $\mu$ . The latter observation, however, is a result of the specific implementation of global delayed feedback according to equation (5.4). Additional numerical simulations have shown that suppression of turbulence is also possible at arbitrarily small values of  $\tau$  when, for instance, the generated control signal acts on the oxygen partial pressure  $p_{\text{O}_2}$  instead on the CO partial pressure.

Even if global delayed feedback is too weak to completely suppress turbulence, it still can alter the properties of the turbulent state. An interesting state is observed close to the synchronization border [the boundary between the white and the gray-shaded regions in Fig. 6.24(a)]. Here, usually a large part of the system is already in the state of uniform oscillations, but a few localized amplitude defects persist. Individual defects either die out in the further evolution of the system, or they initiate a cascade of defect reproduction. The resulting state is reminiscent of *intermittent turbulence* in the CGLE (cf. Section 2.3) and is investigated more closely below.

At feedback parameters corresponding to the dark gray regions in Fig. 6.24, the turbulent state is suppressed via the formation of cluster patterns. As it is also shown later, two different types of stable clusters are observed: phase clusters with period-doubled anti-phase oscillations and amplitude clusters with coexistent limit cycles.

A different synchronization diagram is obtained when a uniform state with small superimposed random perturbations is taken as initial condition in the simulations, see

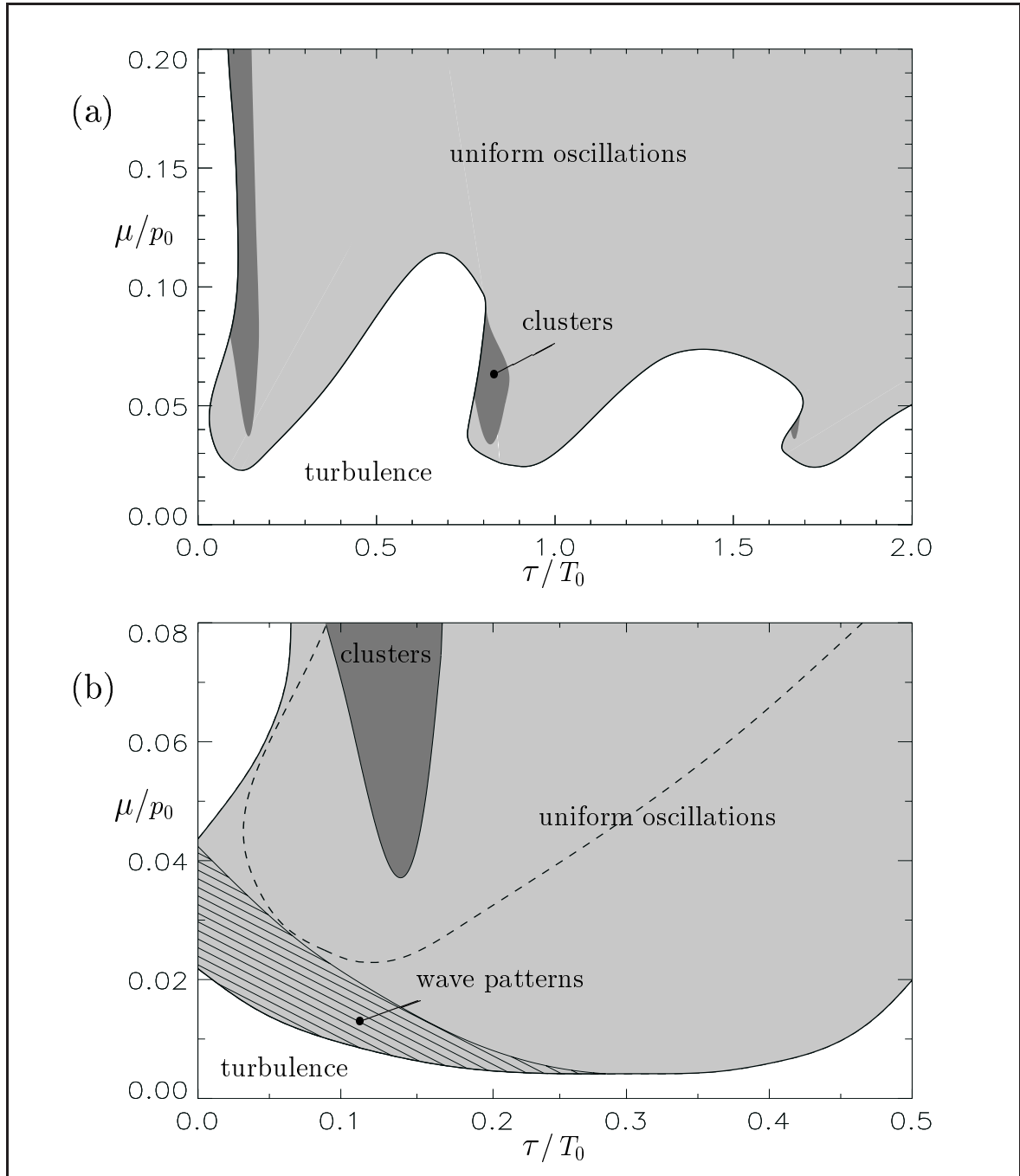


Figure 6.24: Synchronization diagrams for one-dimensional systems in presence of global delayed feedback, showing the approximate boundaries of different dynamical regimes reached after transients. The diagrams are based on numerical simulations that started with (a) developed turbulence and (b) a slightly perturbed uniform state as initial conditions. For comparison, the synchronization border in frame (a) is additionally shown in frame (b) as dashed line. The delay time is measured in multiples of the oscillation period of the system in absence of diffusion and feedback,  $T_0 = 2.73$  s. The feedback intensity is normalized to the base CO partial pressure  $p_0 = 4.81 \times 10^{-5}$  mbar.

Fig. 6.24(b). Note that the displayed range of feedback parameters is different from Fig. 6.24(a). For comparison, the synchronization border in Fig. 6.24(a) is also shown in Fig. 6.24(b) as dashed line.

Examining Fig. 6.24(b), it is found that the stability region of uniform oscillations extends far beyond the former synchronization boundary (dashed line). Thus, in a large range of delays, the uniform state shows strong hysteresis when the feedback intensity is decreased from large values. Turbulence spontaneously develops from almost uniform initial conditions only at feedback parameters outside the shaded regions. However, in the intermediate parameter range inside the shaded regions but below or to the left of the dashed line, a sufficiently strong local perturbation of the uniform state is able to initiate a defect cascade, yielding either intermittent or developed turbulence. The formation of clusters is not noticeably affected by hysteresis effects.

Further types of patterns exist in the hatched region in Fig. 6.24(b). In this region, uniform oscillations are unstable, and *wave patterns* characterized by an intrinsic wavelength develop from small random perturbations. Approximately in the parameter region where wave patterns develop in one-dimensional systems, *cellular structures* are found in two-dimensional systems. Wave patterns, cellular structures, and their transition to turbulence are also further discussed in the following sections.

### 6.2.3 Intermittent turbulence

When global delayed feedback is present but too weak to completely suppress turbulence, it still can alter the properties of the turbulent state. Turbulent bursts then occur on a laminar background, and hence a certain degree of long-range order is retained. An example of such intermittent turbulence is displayed in Fig. 6.25. The chosen parameter values are close to the synchronization border in Fig. 6.24(a). The resulting state is characterized by repeated cascades of amplitude defects on the background of uniform oscillations. The defects reproduce until nearly the entire system is covered by turbulence. Then they simultaneously annihilate in certain parts of the medium. Sometimes only a few defects survive and initiate another reproduction cascade. In this way, the system behavior alternates between strongly turbulent states with only short-scale spatial correlations and nearly uniform states with large-scale spatial correlations. Intermittent turbulence is also observed as a transient above the synchronization border in Fig. 6.24(a); however, all defects finally die out in simulations there. As the feedback intensity is decreased from large values towards the synchronization border, the life time of defects strongly increases.



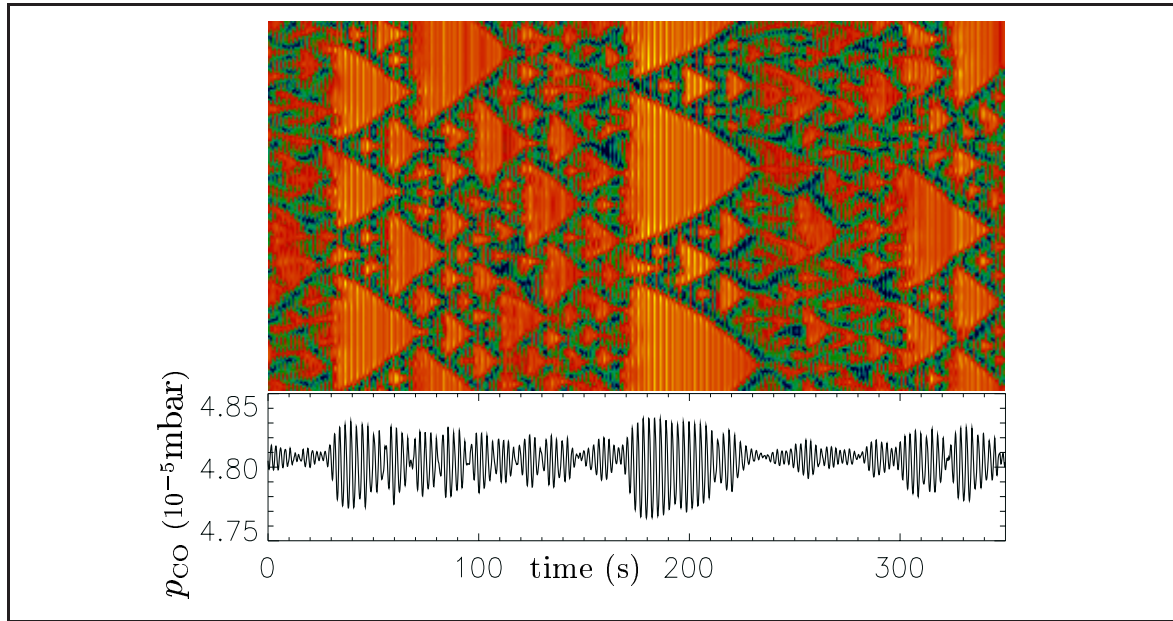


Figure 6.25: *Space-time diagram of intermittent turbulence in a one-dimensional system. The amplitude  $R$  is plotted; dark blue color denotes low amplitude values. Below the space-time diagram, the corresponding chaotic temporal variations of the CO partial pressure are shown. The feedback parameters are  $\tau / T_0 = 0.293$  and  $\mu / p_0 = 0.043$ .*

To quantitatively analyze the properties of intermittent turbulence, a real global amplitude  $\xi(t) = |\bar{\eta}|$  can be defined as the modulus of the spatial average of a complex amplitude  $\eta$ , where  $\eta(\mathbf{x}, t) = R(\mathbf{x}, t) e^{i\phi(\mathbf{x}, t)}$ . For a state of intermittent or developed turbulence, the value of  $\xi(t)$  fluctuates in time with a standard deviation  $\sigma_\xi$  around a time-averaged value  $\langle \xi \rangle$ . The value of  $\langle \xi \rangle$  vanishes in case of completely uncorrelated oscillations and is equal to unity in case of uniform oscillations with amplitude  $R = 1$ . Thus, the time-averaged global oscillation amplitude  $\langle \xi \rangle$  can be interpreted as a measure of the degree of synchrony in a spatiotemporal pattern.

Fig. 6.26(a) shows the dependence of the values of  $\langle \xi \rangle$  and  $\sigma_\xi$  on the feedback intensity for a constant delay. The state of developed turbulence has been taken as initial condition for the simulations underlying Fig. 6.26. Starting from small values of  $\mu$ , both quantities continuously increase with increasing feedback intensity. In the resulting patterns, this behavior is reflected by an increasing number and average size of the laminar regions. Thus, the quantitative analysis yields that the transition from amplitude turbulence to intermittent turbulence is smooth. At a critical value of  $\mu$ , where the value of  $\langle \xi \rangle$  makes a jump, all defects have died out after transients and the oscillations are uniform. This corresponds to the crossing of the synchronization border in Fig. 6.24(a). In small systems, the values of  $\langle \xi \rangle$  and  $\sigma_\xi$

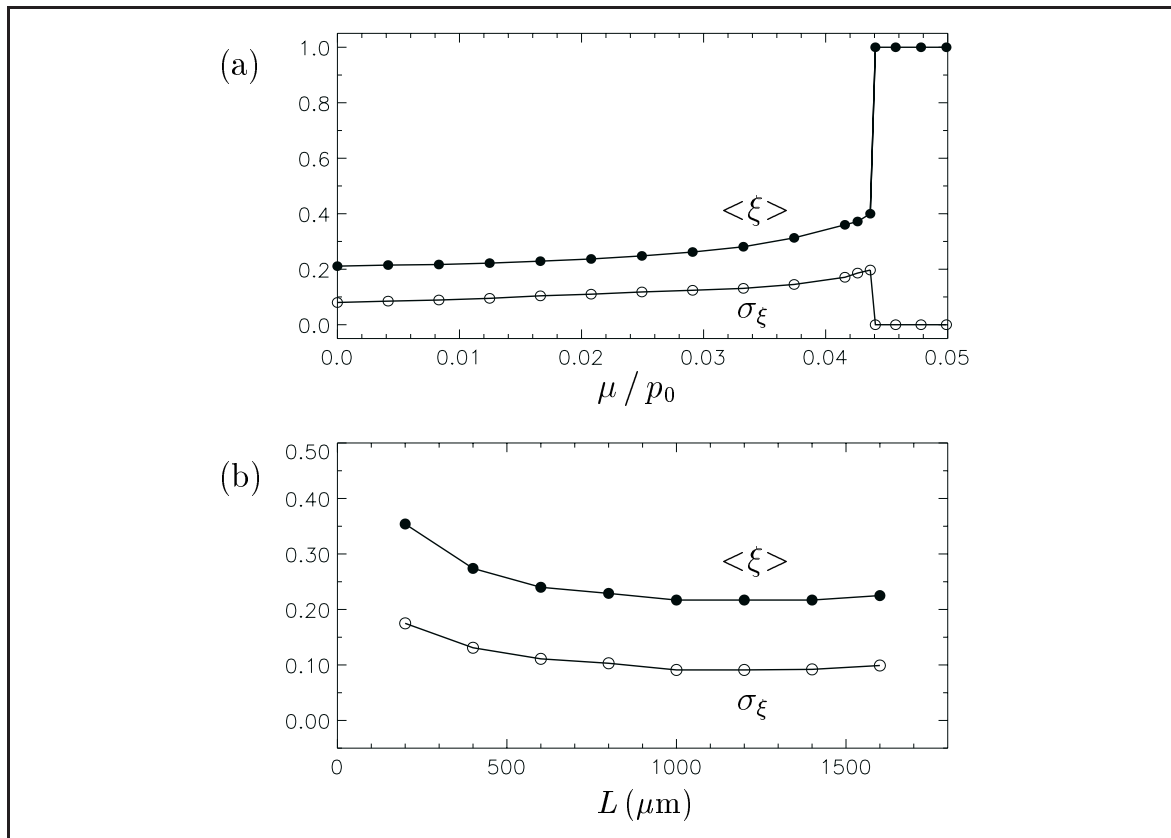


Figure 6.26: (a) Dependence of the time-averaged global oscillation amplitude  $\langle \xi \rangle$  (black circles) and the standard deviation  $\sigma_\xi$  (white circles) on the feedback intensity for a constant delay,  $\tau / T_0 = 0.293$ . The system size is  $L = 0.8$  mm. The lines are drawn to guide the eye. The averaging interval is  $\Delta t = 1000$  s. (b) Dependence of  $\langle \xi \rangle$  and  $\sigma_\xi$  on the system size at constant feedback parameters,  $\tau / T_0 = 0.293$  and  $\mu / p_0 = 0.017$ .

depend on the system size, see Fig. 6.26(b). This dependence saturates for larger systems.

In two space dimensions, intermittent turbulence is characterized by irregular cascades of nearly circular structures on the background of uniform oscillations. Figure 6.27 displays subsequent snapshots of the spatial distributions of phase and amplitude in such a pattern. Additionally, phase portraits are shown in the bottom of Fig. 6.27, obtained by plotting the amplitudes and phases for all resolving pixels in polar coordinates. At constant feedback parameters, the pattern evolution is as follows: at a certain point in time, individual bubbles and ring-shaped structures are present on an almost laminar background, see Fig. 6.27(a). Inside the localized objects, the oscillation amplitude is strongly decreased. A distinct structure is then found in the phase portrait, where the uniform background corresponds to the end of the tail. As time goes on, the bubbles break, reproduce and transform into expanding rings, see Figs. 6.27(b) and 6.27(c). During this process, the structure in the phase portrait slowly

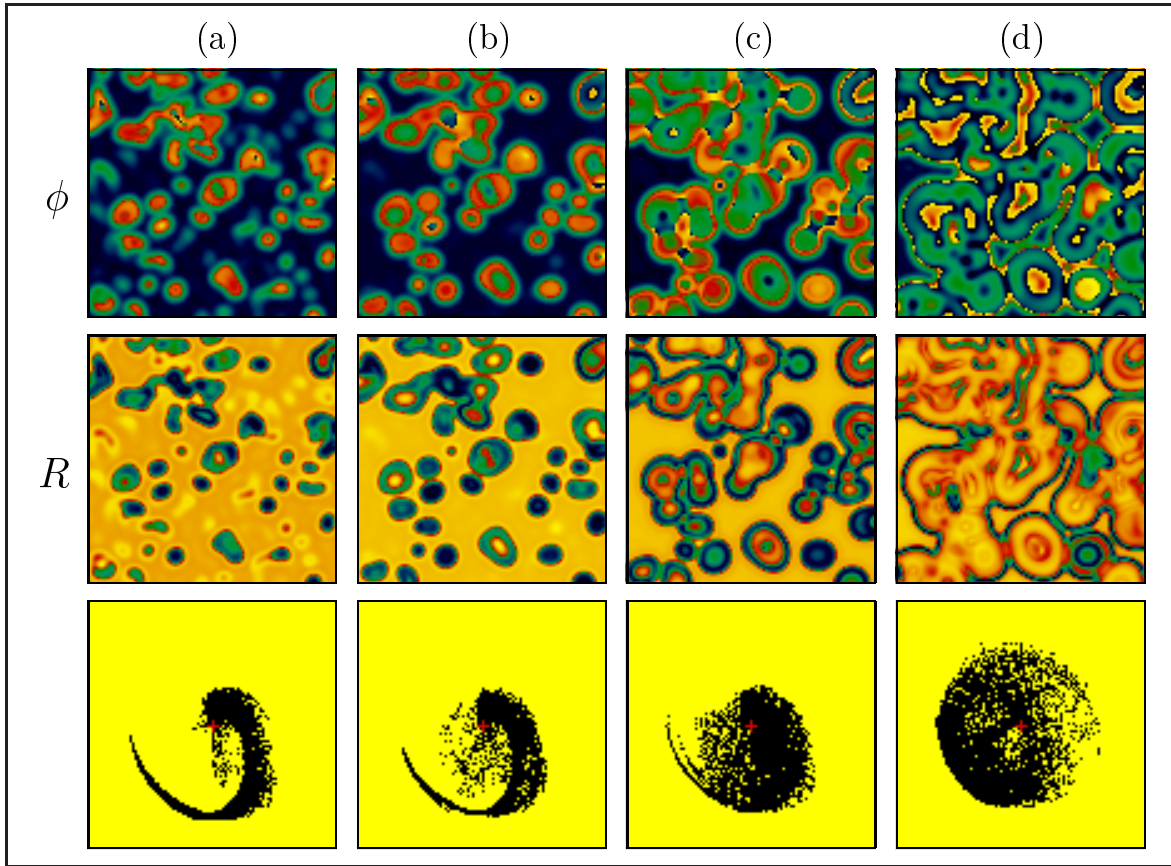


Figure 6.27: Snapshots of the phase (top), amplitude (middle row), and phase portraits (bottom) for intermittent turbulence in two space dimensions. The time interval between the subsequent images shown in each row is  $\Delta t = 5.2$  s and approximately corresponds to two periods of the oscillating background. The system size is  $0.6 \times 0.6 \text{ mm}^2$ . The parameter values are  $\tau / T_0 = 0.293$  and  $\mu / p_0 = 0.056$ .

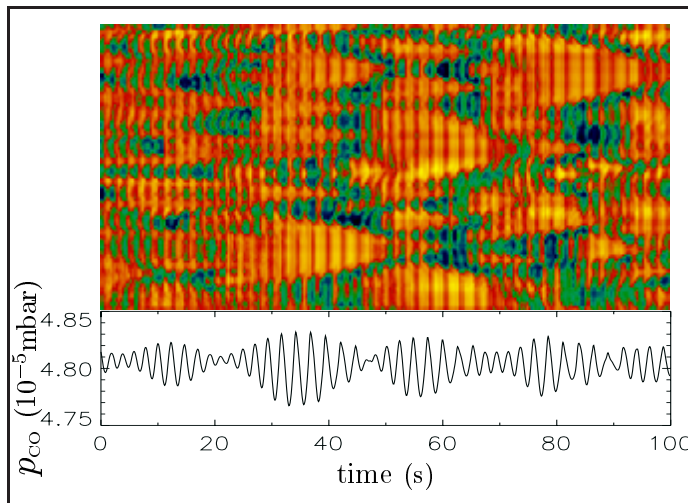


Figure 6.28: Pattern evolution along a cross-section through a two-dimensional pattern representing intermittent turbulence. A space-time diagram of the amplitude and the variation of CO partial pressure are displayed. The same parameters as in Fig. 6.27.



scatters. A few oscillation periods later, the turbulent objects have merged and only small laminar regions are left, as displayed in Fig. 6.27(d). Extended line defects separate the laminar regions from the parts that were invaded by turbulence. Another such cycle is initiated some time later, when again large parts of the turbulent regions spontaneously synchronize and only a few localized defects survive. Note that the pattern evolution along a cross section through the two-dimensional system is characterized by irregular defect cascades similar to the one-dimensional case, see Fig. 6.28.

### 6.2.4 Cluster patterns

In the cluster regions in Fig. 6.24, two different types of stable clusters, namely phase clusters and amplitude clusters, have been observed. Similar patterns were already encountered in Section 6.1.4, and therefore the following description focuses on the differences to the previously observed structures.

At most feedback parameters inside the cluster regions in Fig. 6.24, two-phase clusters develop. Starting from amplitude turbulence, consecutive snapshots during the development of such a pattern are displayed in Fig. 6.29. On the time scale of a few seconds, amplitude turbulence is gradually suppressed and synchronized domains with anti-phase oscillations

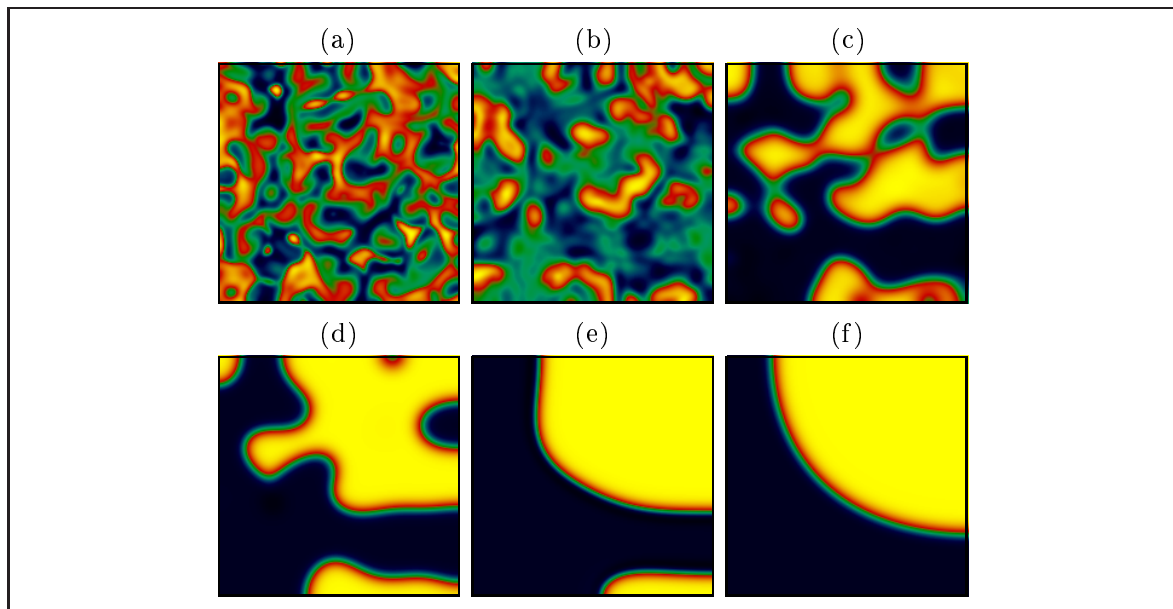


Figure 6.29: Development of phase clusters from amplitude turbulence in two space dimensions. The variable  $u$  is displayed at different points in time after global feedback has been switched on: (a)  $t = 0$  s, (b)  $t = 8.2$  s, (c)  $t = 16.4$  s, (d)  $t = 28.6$  s, (e)  $t = 98.2$  s, and (f)  $t = 294.5$  s. The parameter values are  $\tau / T_0 = 0.147$  and  $\mu / p_0 = 0.083$ .

develop [Figs. 6.29(a)–6.29(c)]. The initial spatial distribution of such domains is random. During the further evolution, individual cluster domains of equal phase merge and smaller domains die out [Fig. 6.29(c)–6.29(e)]. A further slow drift of the phase fronts is then still observed, with a tendency to minimize the front curvature. Finally, a stable stationary distribution is reached [Fig. 6.29(f)]. As it was also observed when uniform oscillations were stable in absence of feedback (see Section 6.1.4), in the final state the phase clusters show the property of phase balance, i.e., the total areas occupied by the different phase domains are equal.

A difference to the previously observed phase clusters is seen in the space time-diagram of a one-dimensional pattern displayed in Fig. 6.30. Examining this diagram, it is found that local oscillations now are characterized by an alternating magnitude of subsequent oscillation maxima. This phenomenon, which arises from a period doubling of local oscillations, significantly affects the properties of the phase fronts. While within the synchronous phase domains, consecutive local oscillation maxima have a large difference, this difference continuously decreases towards the center of a phase front. In the middle of the front, there is a point where the oscillations are simple periodic and almost coincide with the global oscillations in the pattern (black line in Fig. 6.30). Thus, an oscillation node is absent inside such fronts, in contrast to the previously analyzed domain interfaces in stationary phase clusters (cf. Section 6.1.4).

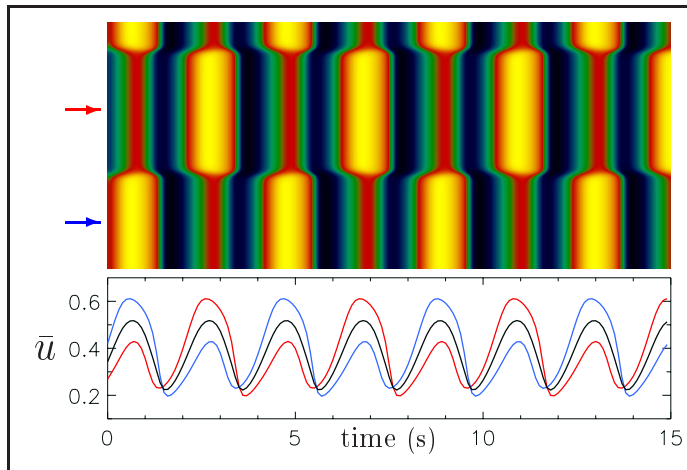


Figure 6.30: Space-time diagram of phase clusters in a one-dimensional system. The variable  $u$  is displayed. The curves in the bottom show the variation of  $u$  within the different cluster domains (blue and red lines) and the variation of  $\bar{u}$  (black line). The same parameters as in Fig. 6.29.

Additionally, stable amplitude clusters exist in the large cluster region in Fig. 6.24(a) (the region at  $\tau / T_0 \approx 0.15$ ) at high feedback intensities,  $\mu / p_0 > 0.17$ . A space-time diagram of such clusters, which are due to the coexistence of two limit cycles, is shown in Fig. 6.31. Inside the small domain, oscillations are simple periodic and have a large amplitude, while the other domains of the pattern show period-two oscillations with much smaller amplitude.

The domain interfaces are stationary and phase balance is absent in such a pattern. Similar amplitude clusters have also been observed as effect of global delayed feedback on stable uniform oscillations, see Section 6.1.4. The main difference is that there, oscillations in both different domain types were simple periodic.

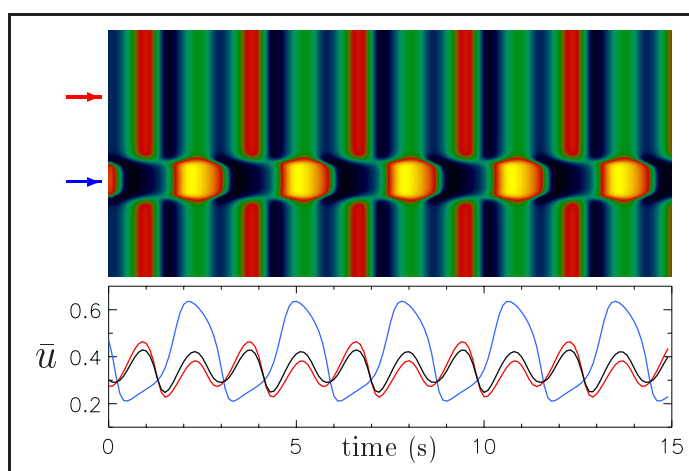


Figure 6.31: *Space-time diagram of clusters with coexistent limit cycles in a one-dimensional system. The representation is the same as in Fig. 6.30. The parameter values are  $\tau / T_0 = 0.088$  and  $\mu / p_0 = 0.200$ .*

### 6.2.5 Wave patterns and phase turbulence

In the following, the types of patterns found in the region in Fig. 6.24(b) denoted by ‘wave patterns’ are described. All such structures are stable with respect to small perturbations, but transform into intermittent or developed turbulence when a sufficiently strong local perturbation is applied.

Close to the upper boundary of this region, oscillatory *standing waves* with an intrinsic wavelength are found in one space dimension, see Fig. 6.32 for an example. Such patterns represent spatially periodic variations of the state of uniform oscillations. Both the spatial distributions of the oscillation phase and amplitude are periodically modulated, see Fig. 6.32(b). A local increase of  $R$  corresponds to a decrease of  $\phi$ . These modulations are stationary, so that all system elements show periodic oscillations, see Fig. 6.32(a). The phase and amplitude variations are small for feedback parameters close to the border to uniform oscillations, and continuously grow as the feedback intensity is decreased at a constant delay. Standing waves arising from a finite wavelength instability were previously also observed in the model of CO oxidation under intrinsic gas phase coupling [114, 151].

Upon a decrease of the feedback intensity, standing waves become unstable when the amplitude and phase modulations have reached a certain critical size. Neighbored phase minima then start to weakly oscillate around their mean position, thereby forming

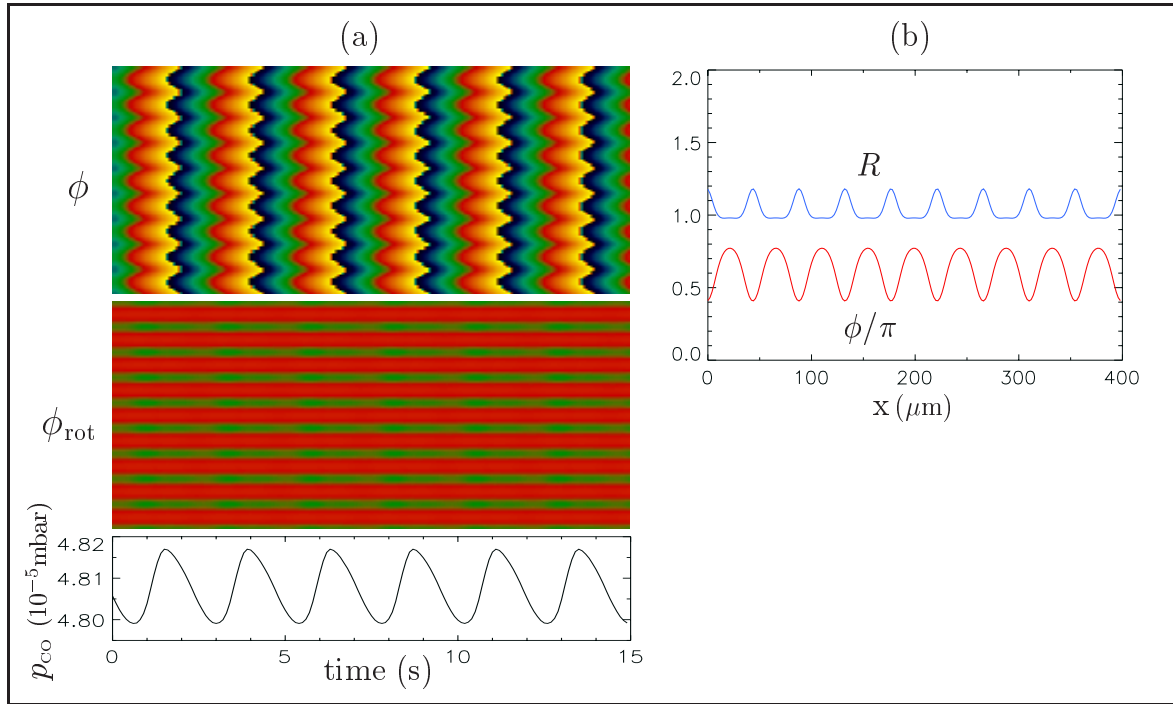


Figure 6.32: Standing waves in a one-dimensional system. (a) Space-time diagrams of the phase in a stationary coordinate frame (top) and in a frame rotating with the period of the reference orbit (middle). The corresponding variations of the CO partial pressure are shown in the bottom. (b) Snapshots of the phase and amplitude profiles. The parameter values are  $\tau/T_0 = 0.110$  and  $\mu/p_0 = 0.012$ .

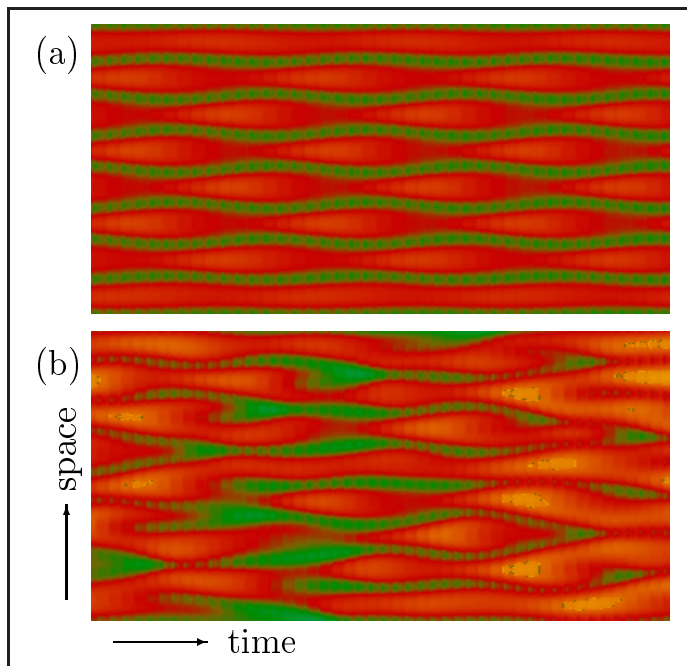


Figure 6.33: Space-time diagrams of (a) breathing waves and (b) phase turbulence in a one-dimensional system. The phase distribution is displayed in a coordinate frame rotating with the period of the reference orbit. The shown time interval is (a) 100s and (b) 200s. The parameter values of  $\tau/T_0$  and  $\mu/p_0$  are, respectively, (a) 0.110, 0.010, and (b) 0.110, 0.008.

a pattern of *breathing waves*, see Fig. 6.33(a). When  $\mu$  is further decreased, the strength of the breathing becomes comparable to the spatial wavelength of the pattern and its regularity breaks down. The resulting state is shown in Fig. 6.33(b). Colliding local phase minima merge and from time to time new such regions are created. However, the phase and amplitude modulations remain comparatively weak, and the global oscillations are still nearly periodic. Such a behavior is reminiscent of *phase turbulence* in the one-dimensional CGLE [compare Fig. 6.33(b) with Fig. 2.4(a)]. Defects are only spontaneously created in the system when the feedback intensity is further decreased below the hatched region in Fig. 6.24(b), where they quickly reproduce to form amplitude turbulence.

### 6.2.6 Cellular structures

About in the region of feedback parameters where wave patterns and phase turbulence are found in one space dimension, oscillatory cellular structures develop in two-dimensional systems. As wave patterns, such structures represent small-amplitude modulations of uniform oscillations and are replaced by intermittent or amplitude turbulence upon a sufficiently large local perturbation. Three different types of cellular structures are encountered. Close to the border to uniform oscillations, the cell arrays are regular and show a hexagonal symmetry, see Fig. 6.34(a). Such patterns are the result of nonlinear interactions between triplets of modes of wave vector  $\mathbf{k}$  with the same wave number  $|\mathbf{k}| = k_0$  [157]. The observed structures are stationary in space, but show time-periodic local oscillations.

When the feedback intensity is decreased, stationary cell arrays become unstable at a certain delay-dependent value of  $\mu$ . Individual cells then periodically shrink and expand, thereby forming an array of breathing cells, see Fig. 6.34(b). In the spatial Fourier spectrum of such a pattern, two independent frequencies are present. As in the one-dimensional system, phase turbulence develops upon further decrease of the feedback intensity. A snapshot of the resulting state, characterized by the mobility of cells, is shown in Fig. 6.34(c). Individual cells shrink and expand aperiodically while they slowly travel through the medium. Occasionally, some of the cells die out or, following an expansion, reproduce through cell splitting, see Fig. 6.35 for such an event. Phase turbulence is replaced by amplitude turbulence when the feedback intensity is further decreased.



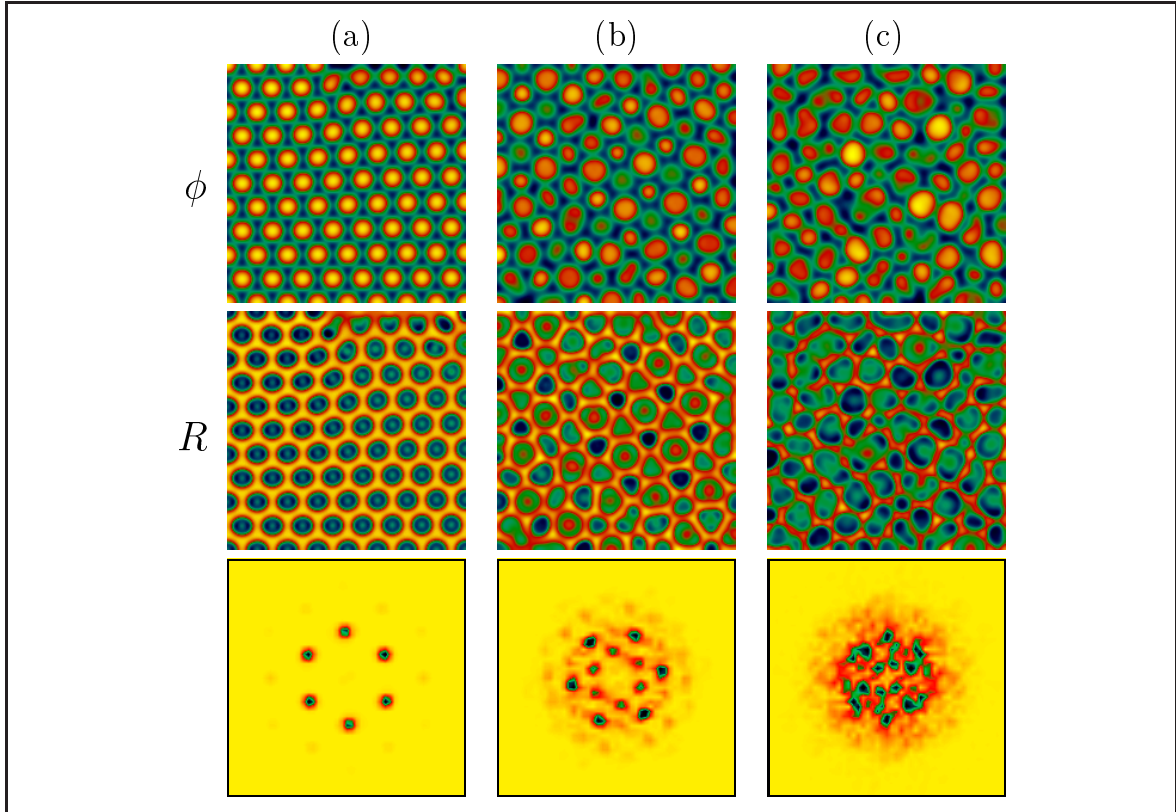


Figure 6.34: Different types of cellular structures in two space dimensions. Displayed are distributions of phase (top) and amplitude (middle row), and spatial Fourier spectra of the amplitude images (bottom). For the amplitude and phase patterns, the range of the color map has been adapted to the variations in the images in order to increase the color contrast. The parameter values of  $\tau / T_0$  and  $\mu / p_0$  are, respectively, (a) 0.110, 0.019, (b) 0.110, 0.016, and (c) 0.110, 0.012.

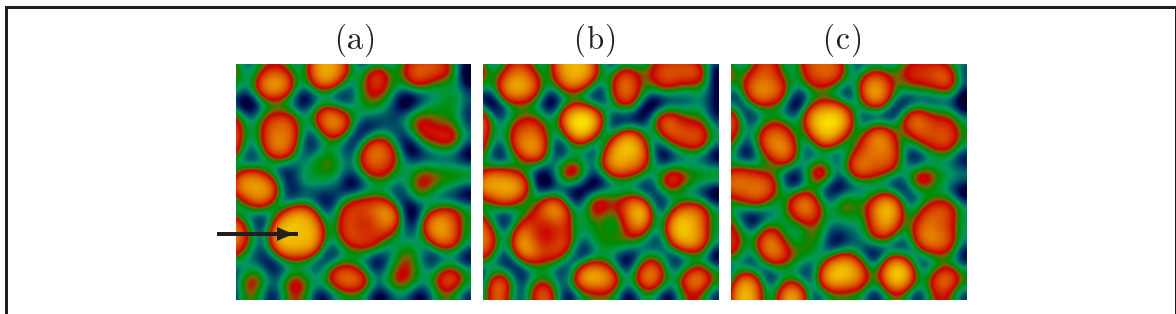


Figure 6.35: Splitting process of a cell. The cell that undergoes splitting is indicated by an arrow. Snapshots of the phase are displayed; only one quarter of the system of size  $0.8 \times 0.8 \text{ mm}^2$  is shown. The time interval between individual frames is  $\Delta t = 4.8 \text{ s}$ . The parameters are as in Fig. 6.34(c).

### 6.2.7 Discussion and comparison with the normal form approach

The above described simulations have shown that amplitude turbulence in the model of CO oxidation can be suppressed by means of global delayed feedback in a wide range of feedback parameters. Moreover, near the edge of chaos, where global delayed feedback is too weak to induce uniform oscillations but strong enough to significantly affect pattern formation, a broad variety of complex patterns was found.

The different observed spatiotemporal structures are summarized in Fig. 6.36. The images in the top row display distributions of the CO coverage  $u$ . Below, the corresponding spatial distributions of the phase (second row) and amplitude (third row) are displayed. Additionally, the bottom row of Fig. 6.36 shows a phase portrait of each pattern.

The unforced turbulent state [Fig. 6.36(a)] is characterized by strong amplitude and phase fluctuations. This state is similar to developed amplitude turbulence in the unforced CGLE (cf. Section 2.3). The patterns shown in Figs. 6.36(b)–6.36(e) represent typical two-dimensional patterns induced by the feedback.

Intermittent turbulence [Fig. 6.36(b)] has been observed close to the synchronization border under increasing feedback intensity. This regime is characterized by irregular cascades of bubbles developing into ring-shaped structures on the background of uniform oscillations. The amplitude is strongly decreased inside such localized objects.

Stationary two-phase clusters [Fig. 6.36(c)] differed from their counterparts in the non-chaotic regime by a period-doubling of local oscillations. This significantly changed the properties of the phase fronts. Note that due to the period-doubling, oscillations within the different cluster domains in Fig. 6.36(c) differ not only in phase, but also in amplitude; nonetheless, they correspond to the same limit cycle. In addition to phase clusters, amplitude clusters with coexistent limit cycles were also observed (not shown in Fig. 6.36).

Hexagonal cell arrays [Fig. 6.36(d)] were found in a range of feedback parameters where standing waves developed in one space dimension. Secondary instabilities led to breathing cellular structures, and to phase turbulence [Fig. 6.36(e)]. As seen in the corresponding phase portraits, both the phase and the amplitude are modulated in such structures, though the amplitude variations are weak.

Similar patterns were also seen in the previous studies [36,37,112–114] of the CGLE with global feedback (some of them have been reproduced in Fig. 3.5). A comparison of the behavior found in the model of CO oxidation and in the general model reveals that intermittent

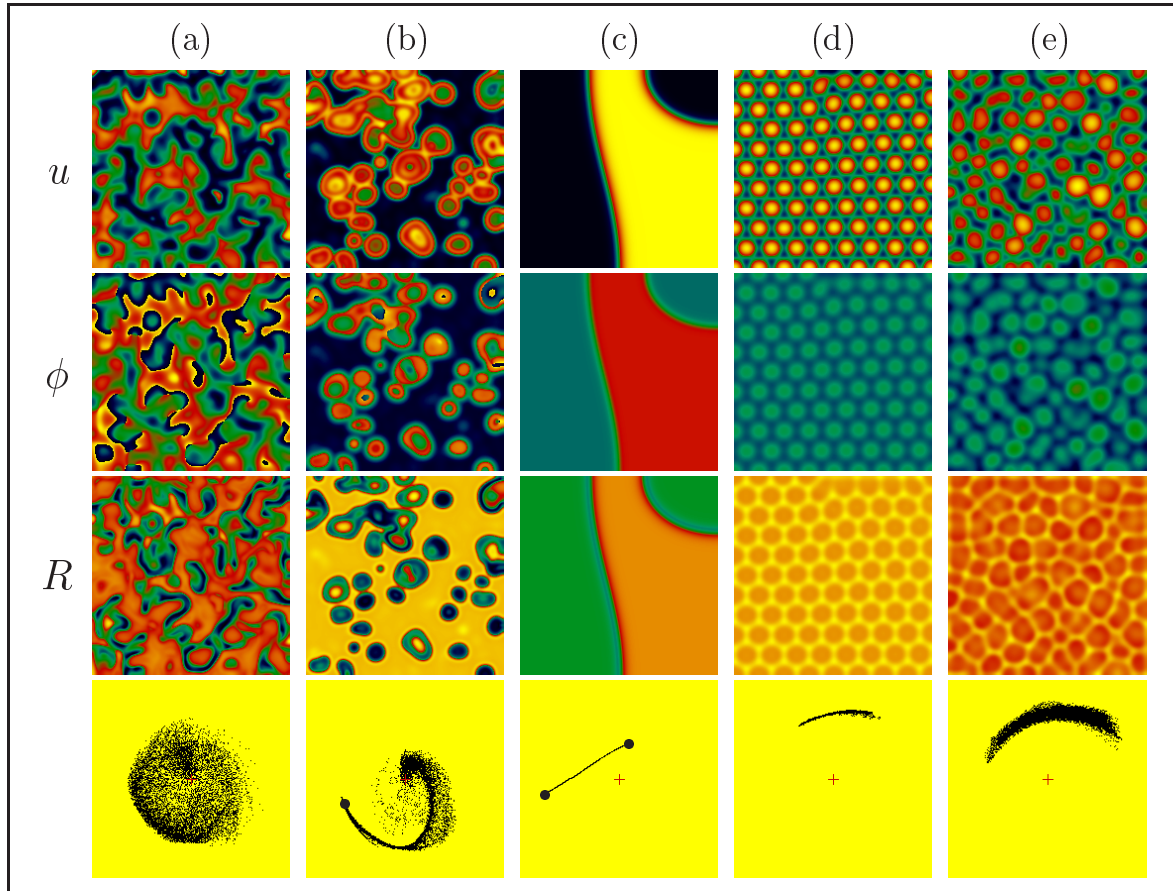


Figure 6.36: Distributions of CO coverage (top), oscillation phase (second row), and oscillation amplitude (third row), and phase portraits (bottom) for several typical two-dimensional patterns. In the phase portraits (b) and (c), bold dots have been added to indicate the uniform states. The side length of the simulated system is 0.4 mm in frames (a), (c)–(e) and 0.6 mm in frame (b). The values of the feedback parameters  $\mu$  ( $10^{-5}$  mbar) and  $\tau$  (s) are: (a) 0, 0; (b) 0.27, 0.8; (c) 0.40, 0.4; (d) 0.09, 0.3; and (e) 0.06, 0.3.

turbulence and hexagonal cells exhibit profoundly similar amplitude and phase properties in these systems [compare Fig. 6.36(b) with Fig. 3.5(c), and Fig. 6.36(d) with Fig. 3.5(b)]. Turbulent bubbles in the amplitude equation have a stronger tendency to aggregate in the shown example. The cascades of reproducing and annihilating amplitude defects found in the model of CO oxidation were also seen in the framework of the CGLE in one space dimension [36, 113]. Note that intermittent regimes have also been observed in the unperturbed CGLE [158] (refer to Fig. 2.4(c) for an example), where they, however, showed somewhat different properties, e.g., no bubble-shaped objects were present in two space dimensions.

Starting from steady hexagonal cells, a decrease of the feedback intensity both in the model of CO oxidation and in the CGLE with global feedback resulted in a similar transition



to oscillating cellular structures. Further decrease of the feedback strength in the amplitude equation led to formation of amplitude turbulence on the background of a cellular structure [Fig. 3.5(a)], while in the CO oxidation model, a sharp transition from phase turbulence [Fig. 6.36(e)] to developed amplitude turbulence was observed.

Phase clusters were not present in simulations of the CGLE with the lowest order term for global feedback, as discussed in Section 6.1.6. Instead, amplitude clusters were observed in certain intervals of the feedback parameters. A typical two-dimensional example of such a pattern is displayed in Fig. 3.5(d). Clusters with similar properties were also found in the CO oxidation model.

In conclusion, it was shown in this chapter that turbulence and pattern formation can be efficiently controlled, and various complex structures can be induced in a model of CO oxidation on Pt(110) by means of global delayed feedback. The model parameters were chosen in such a way that oscillations were not harmonic and the system was not close to a supercritical Hopf bifurcation. Nonetheless, the observed patterns to a wide extent resembled the structures exhibited by the amplitude equation, which is strictly valid only near this bifurcation. It is therefore expected that many of the observed phenomena can be also found in other reaction-diffusion systems of various origins.



**Part III.**  
**Experiments with**  
**CO Oxidation on Pt(110)**



---

## Chapter 7

### Experimental setup

---

The third part of this work is devoted to experiments with CO oxidation on Pt(110) under global delayed feedback and periodic forcing. These experiments have been performed under supervision of H. H. Rotermund. The used experimental setup is described in the following chapter. The ultrahigh-vacuum chamber, its pumping system, and the preparation of the platinum sample are subject of Section 7.1. In Section 7.2, the photoemission electron microscope used for imaging of the sample surface is described. Finally, in Section 7.3, the implementation of periodic forcing and global delayed feedback into the experimental setup is discussed.

#### 7.1 UHV chamber and sample preparation

The ultrahigh-vacuum (UHV) chamber used in surface chemical experiments has been kept at a base pressure of  $10^{-10}$  mbar. The reaction chamber is made of stainless steel and has a volume of about  $60\text{dm}^3$ . The UHV conditions are maintained by the pumping system sketched in Fig. 7.1. The evacuation of the chamber is achieved by two turbomolecular pumps. Their fore vacuum of  $10^{-3}$  mbar is provided by two rotary pumps, and zeolite traps prevent that the chamber is contaminated by hydrocarbon arising from their lubrication oil. The vacuum is further improved by use of a titanium sublimation pump. The overall pressure in the chamber is measured by means of an ionization manometer. A third turbomolecular pump provides differential pumping of the photoemission electron microscope (PEEM) that is used for surface imaging. A differentially pumped quadrupole mass spectrometer (QMS) allows to accurately measure partial pressures under reaction conditions (up to  $10^{-3}$  mbar). The chamber is further equipped with an Ar-ion sputter gun, resistive sample heating, and devices for low-energy electron diffraction (LEED) and Auger electron spectroscopy (AES).

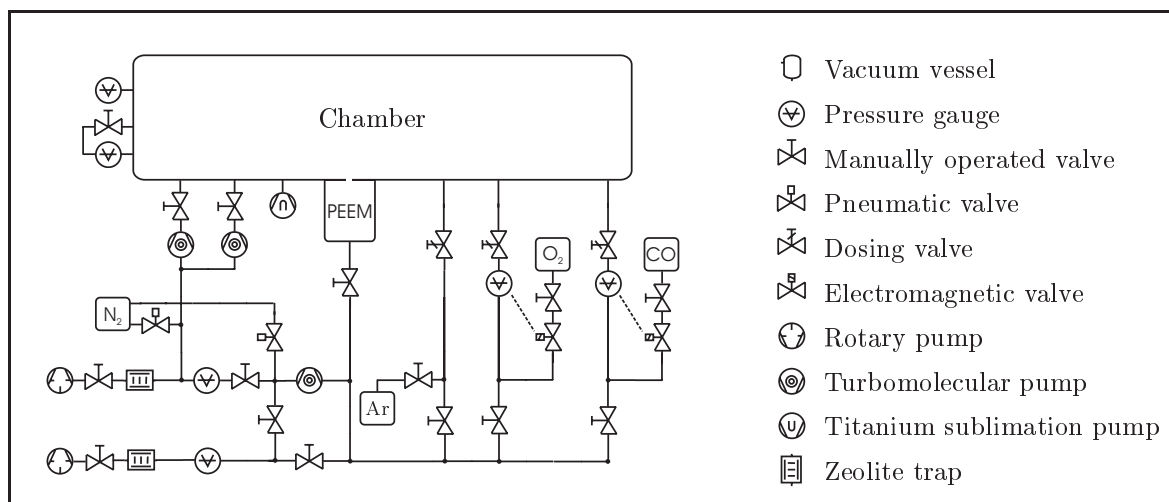


Figure 7.1: Schematic drawing of the pumping system. After Ref. [159].

The supply of reaction gases ( $O_2$  and  $CO$ ) is automatically controlled. A feedback mechanism which acts on an electromagnetic valve allows to keep constant the partial pressures within a maximal variation of 0.1 % (see Ref. [160] for details). Only purified gases ( $CO$  4.7,  $O_2$  5.6, and  $Ar$  5.0) have been used. By continuous supply and pumping of gases, the system is operated as a continuous flow reactor.

Preceding each series of experiments, the sample has been prepared by repeated cycles of  $Ar$  sputtering below 470K and subsequent annealing to 750K. To minimize the effects of internal global gas phase coupling, specially prefabricated single crystals have been used. About 80 % of the  $Pt(110)$  single crystal surface (10mm in diameter) has been covered by microlithographic deposition with  $Ti$ . The microlithographic fabrication of the crystal samples was done at Princeton University with the help of I. G. Kevrekidis. The  $Ti$  layer has been oxidized in the chamber, thereby producing a  $TiO_2$  layer which is not catalytically active for the considered reaction. Only the free  $Pt$  areas remained active. In this way isolated surface reactors of various sizes could be created. For the experiments reactive areas of about  $1\text{ mm}^2$  have been chosen.

## 7.2 Visualization of patterns

The formation of spatiotemporal patterns on the catalytic surface has been imaged by means of photoemission electron microscopy (PEEM) [123, 124]. This method produces real-time images of the lateral distribution of adsorbed species on the catalytic surface. More precisely, the distribution of photoelectron emission from the surface under ultraviolet light irradiation

is displayed. The yield of photoelectrons depends sensitively on the local work function  $\phi$  of the substrate, which is changed due to the presence of adsorbates. As compared with the free Pt(110) surface, a monolayer of oxygen coverage increases the work function by  $\Delta\phi \approx 0.8$  eV, thereby strongly decreasing the brightness of PEEM images. Full CO coverage also increases the work function but produces a smaller effect ( $\Delta\phi \approx 0.3$  eV). When formation of subsurface oxygen occurs, this species is detected by a strong decrease of the work function and thus appears as bright patches in the images.

A schematic drawing of the PEEM instrument is shown in Fig. 7.2. The emission of photoelectrons from the sample is caused by photons that stem from homogeneous illumination by a deuterium discharge lamp. The ultraviolet light has a continuous spectral intensity characteristic (see Ref. [161]). The angle of light incidence is about  $75^\circ$  from the surface normal. In order to capture as many produced photoelectrons as possible, the distance between the sample and the objective is small ( $d = 4$  mm). Within this distance, the electrons are accelerated by a potential difference of about 20 kV. A system of three lenses then magnifies the electron image by a factor of  $10^2$  to  $10^3$ . The lens combination also decelerates the fast electrons to energies for which the channelplate has its highest sensitivity (about 1 keV). The channelplate typically amplifies the electron distribution by a factor of  $10^3$ . Finally, a

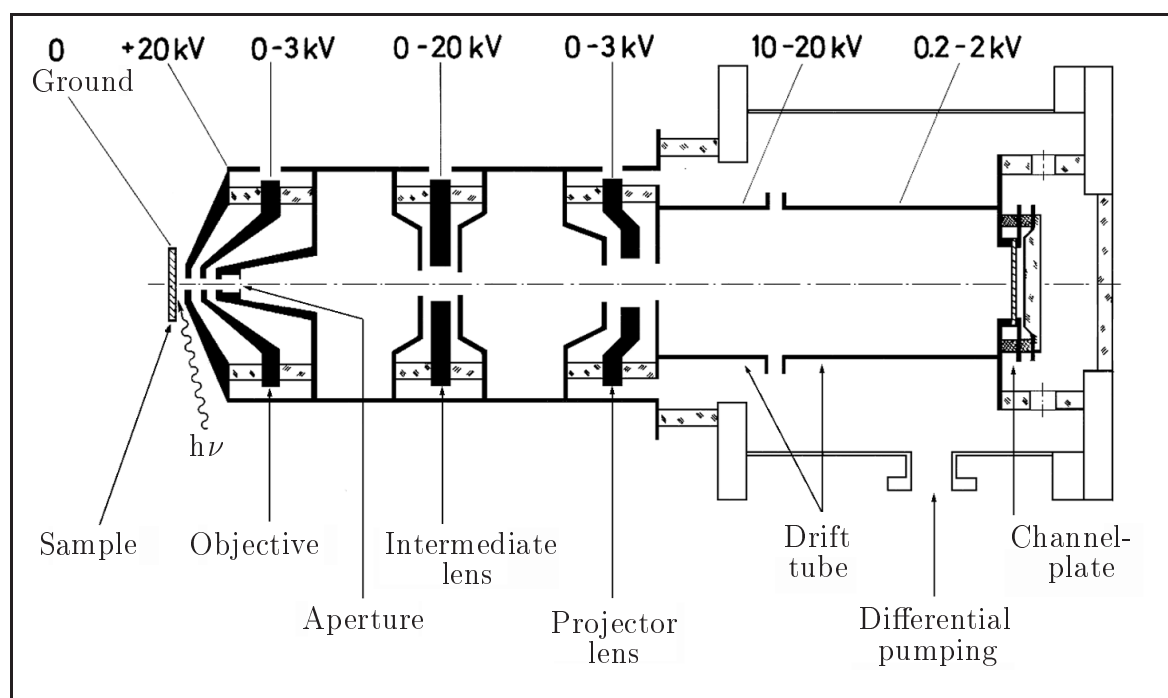


Figure 7.2: Schematic drawing of the photoemission electron microscope, not to scale. After Ref. [124].

phosphor screen converts the electron image into a photon image which then is recorded by a CCD camera. A small aperture of  $300\mu\text{m}$  in diameter and differential pumping allow the operation of the PEEM instrument at pressures up to  $10^{-3}$  mbar in the main chamber.

In the conducted experiments, the spatial resolution of images has been about  $1\mu\text{m}$  with the typically chosen field of view of  $500\mu\text{m}$ . A frame rate of 25 camera images per second guaranteed a sufficiently good temporal resolution of the PEEM recordings. Standard image processing including background subtraction, contrast/brightness adjustments, and image averaging has been performed to improve the signal-to-noise ratio of the images.

### 7.3 Implementation of the control strategies

Periodic forcing and global delayed feedback have been experimentally implemented via the gas phase. Partial pressure variations affect the reaction conditions on the catalytic surface in a uniform way. The automated gas inlet system allowed the controlled modulation of the CO partial pressure in the chamber by changing the dosing rate of CO molecules. The CO partial pressure followed the externally applied temporal modulation with a delay  $\tau_0 \approx 0.8\text{ s}$  determined by the residence time of gases in the pumped chamber. Well controlled CO partial pressure variations could be introduced with frequencies up to  $0.5\text{ Hz}$  at typical relative amplitudes of about  $10\%$ . The applied partial pressure variations were large in comparison to the internal pressure variations due to global gas phase coupling. During the experiments, the CO partial pressure was measured with the differentially pumped QMS and therefore its correspondence with the applied signal could be directly checked.

Periodic external forcing has been implemented by using a frequency generator to control the dosing rate of CO molecules. In this way, the CO partial pressure in the reaction chamber could be periodically modulated with a nearly harmonic signal of amplitude  $\gamma$  and frequency  $\omega_f$ , while its temporal average  $p_0$  was kept constant.

In order to introduce global delayed feedback, the instantaneous dosing rate of CO molecules was made dependent on real-time properties of the developing patterns. The experimental setup with the applied feedback loop is sketched in Fig. 7.3. While monitoring the patterns on the surface, the PEEM intensity was simultaneously averaged over the entire observation window by means of an electronic integrating device. The level of intensity was scaled such that a CO (oxygen) saturated surface corresponded to a value of 1 (0). From the resulting global signal  $I(t)$ , a reference value  $I_{\text{ref}}$  was then subtracted using a pre-set potentiometer. The reference value has been determined in the beginning of each series of



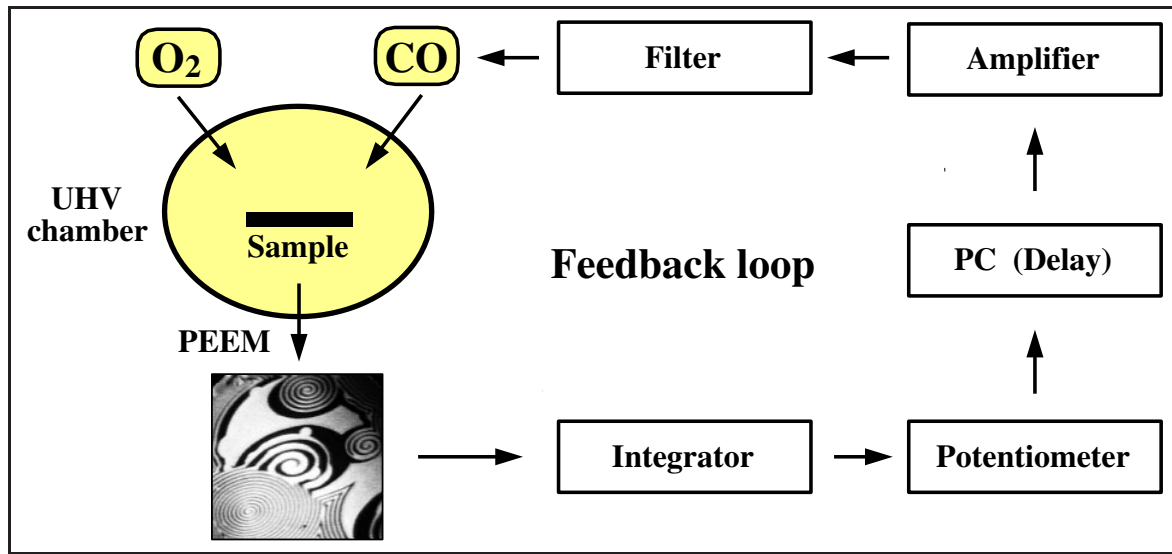


Figure 7.3: Schematic drawing of the experimental setup with global delayed feedback.

experiments, before global delayed feedback was applied. It was chosen as the time-average of the global PEEM intensity  $I(t)$  in the initially developing state, i.e., chemical turbulence or stable spiral waves. In the following step, the signal was delayed by a certain time  $\tau_d$  using a computer. Afterwards, the delayed signal was electronically amplified by a factor determining the feedback intensity. A high-frequency filter was used to reduce electric noise and to invert the signal. Finally, the control signal was applied back to the reaction by controlling the automated inlet system for CO gas.

Thus, a global delayed feedback could be artificially introduced, such that

$$p_{\text{co}}(t) = p_0 - \mu[I(t - \tau) - I_{\text{ref}}], \quad (7.1)$$

where  $p_{\text{co}}$  is the CO partial pressure in the reaction chamber,  $I(t)$  denotes the total PEEM intensity at time  $t$ ,  $\tau = \tau_0 + \tau_d$  is the effective time delay, the parameter  $\mu$  specifies the feedback intensity, and  $p_0$  and  $I_{\text{ref}}$  are the CO partial pressure and the mean base level of the integral PEEM intensity in absence of feedback, respectively. Note that the above specified feedback loop is of the same form as the feedback implemented in the model of CO oxidation [cf. equation (5.4)], except that in the model, a simplification was made by using the average CO coverage  $\bar{u}$  to generate the control signal.



---

## Chapter 8

# Pattern formation under global delayed feedback

---

In this chapter, CO oxidation experiments with artificial global delayed feedback are presented. They provide the experimental counterpart of the theoretical investigations described in Chapter 6.

In Section 8.1, the influence of global delayed feedback on pattern formation is studied in a non-chaotic parameter regime, characterized by the existence of stable spiral waves. Three different types of behavior are observed: synchronization and desynchronization of local oscillations, and the formation of phase clusters. The effects of global delayed feedback on chemical turbulence are investigated in Section 8.2. It is shown that chemical turbulence can be suppressed by this method, and a rich variety of spatiotemporal patterns is found at the transition from turbulence to uniform oscillations. To characterize the observed patterns, they are transformed in Section 8.3 into the spatial distributions of phase and amplitude variables. This is achieved by using a variant of the analytic signal approach.

### 8.1 Manipulating non-chaotic patterns

The experiments described in the following section have been performed in collaboration with M. Pollmann to test the theoretical predictions presented in Section 6.1. In these experiments, the parameter values of temperature and partial pressures have been chosen in such a way that the system was in an oscillatory state and chemical turbulence was absent. The sample first showed anharmonic uniform oscillations of a period of about 3.5 s, which then were successively replaced by stable rotating spiral waves or target patterns formed around small surface defects.

### 8.1.1 Synchronization and desynchronization of oscillations

When global delayed feedback according to equation (7.1) was applied, it exerted significant influence on the asymptotic behavior of the system. First the results of experiments are reported where the feedback intensity was kept constant at  $\mu = 0.4 \times 10^{-5}$  mbar and only the time delay was varied. Figure 8.1 summarizes the results of experiments in which the uniformly oxygen covered surface was taken as initial condition. After setting a certain delay, also the CO valve was opened, and global delayed feedback was applied to the uniformly oscillating state. Different types of behavior were found after transients, denoted by different shading in Fig. 8.1.

For delays corresponding to the white regions in Fig. 8.1, the system maintains uniform oscillations. Due to a synchronizing effect of the feedback, in this parameter region the uniform state is not replaced by spiral waves or target patterns even in presence of structural surface defects. In these intervals of the delay, a process of synchronization can be observed when the feedback is switched on after spiral waves or target patterns have already developed in the system. This situation is illustrated in Fig. 8.2. In the shown example, global oscillations initially are absent due to the presence of traveling wave patterns. During a transient time between a few seconds and several minutes, the feedback becomes more and more efficient and the nonuniform patterns are gradually suppressed. Finally, the state of periodic uniform oscillations is stabilized by the oscillating feedback. The suppression of nonuniform patterns requires a minimal feedback intensity of  $\mu \approx 0.4 \times 10^{-5}$  mbar.

A different situation is encountered for delays corresponding to the black regions in Fig. 8.1. At such delay settings, the feedback is unable to synchronize local oscillations, and even cannot maintain uniform oscillations. Starting from a uniformly covered surface, after some time local oscillations gradually desynchronize, and different patterns (spiral waves or

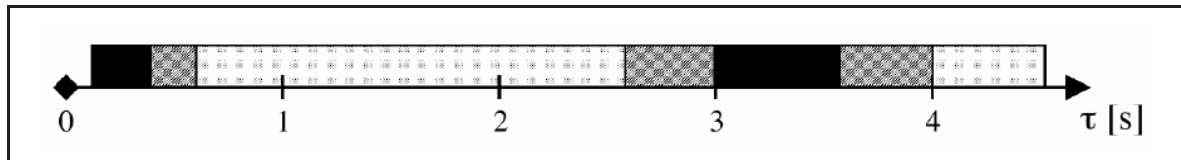


Figure 8.1: *Dependence of the system behavior on the time delay at constant feedback intensity,  $\mu = 0.4 \times 10^{-5}$  mbar. White areas denote synchronization regimes, the black regions correspond to nonuniform patterns, and in gray shaded regions both types of behavior are possible (the diagram summarizes the results of several series of experiments). The parameter values of temperature, oxygen partial pressure, and base CO pressure are, respectively:  $T = 514$  K,  $p_{O_2} = 40.0 \times 10^{-5}$  mbar, and  $p_0 = 3.0 \times 10^{-5}$  mbar. From Ref. [162].*

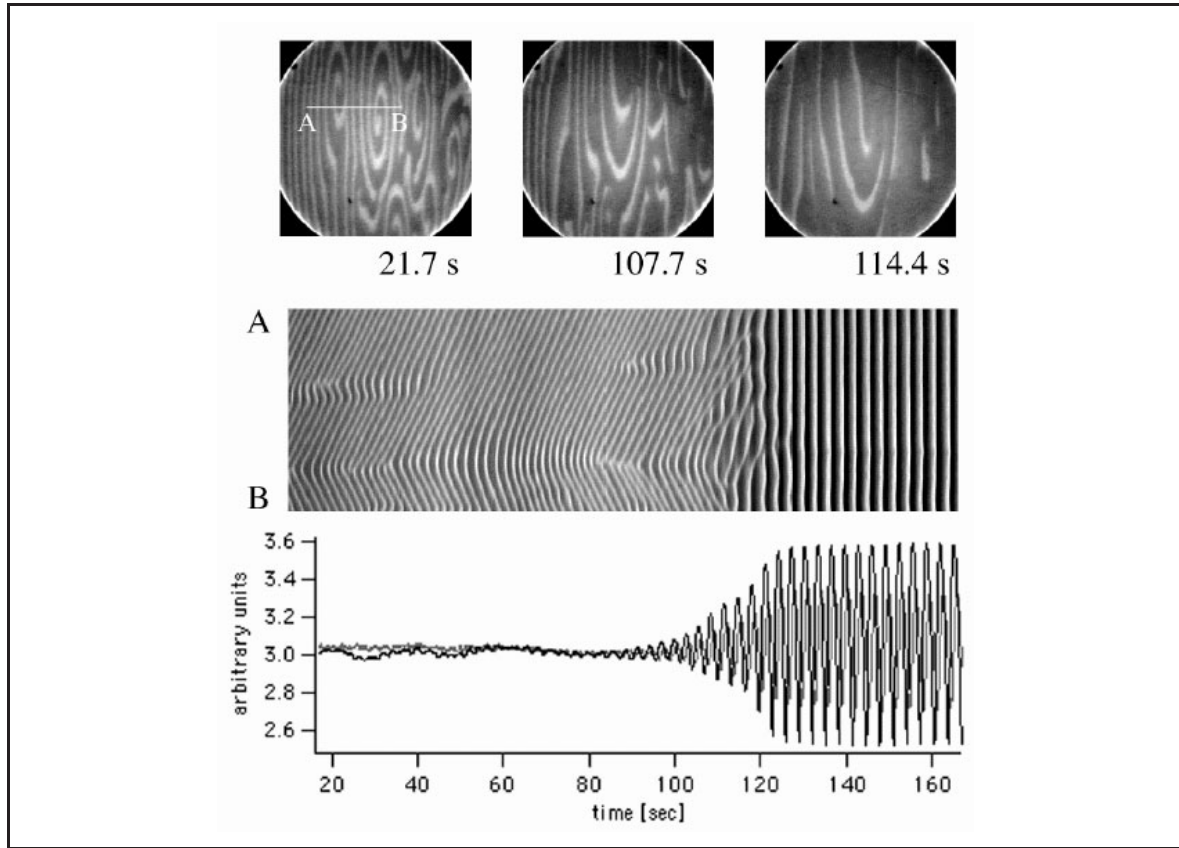


Figure 8.2: *Example of a synchronization process. Top row: PEEM images at different time moments with a field-of-view of  $350\mu\text{m}$  in diameter. Middle row: space-time diagrams along the line AB indicated in the first image. Bottom row: temporal variations of the negative integral PEEM signal  $-I$  (black line) and the CO partial pressure (gray line); the time scale is the same as in the space-time diagram. The feedback parameters are  $\mu = 0.4 \times 10^{-5}$  mbar and  $\tau = 0.7$  s. The other parameters are as in Fig. 8.1. From Ref. [162].*

islands) form. A typical example of such a desynchronization process is displayed in Fig. 8.3. During the transient, the global oscillations in the pattern almost completely break down while patterns with asynchronous oscillations evolve. Usually the developing structures are different as compared to the non-perturbed system (e.g., freely rotating spirals instead of target patterns pinned to defects). The desynchronization windows shrink at higher feedback intensities and eventually completely disappear. In the gray shaded regions in Fig. 8.1, in different series of experiments both stable uniform oscillations and a desynchronization process have been observed due to a small drift of experimental parameters.

It should be noted that the period of global oscillations in the uniform system is strongly dependent on the applied time delay, see Fig. 8.4 for the result of a typical series of experiments. In case of desynchronization, the period has been extracted from the data shortly

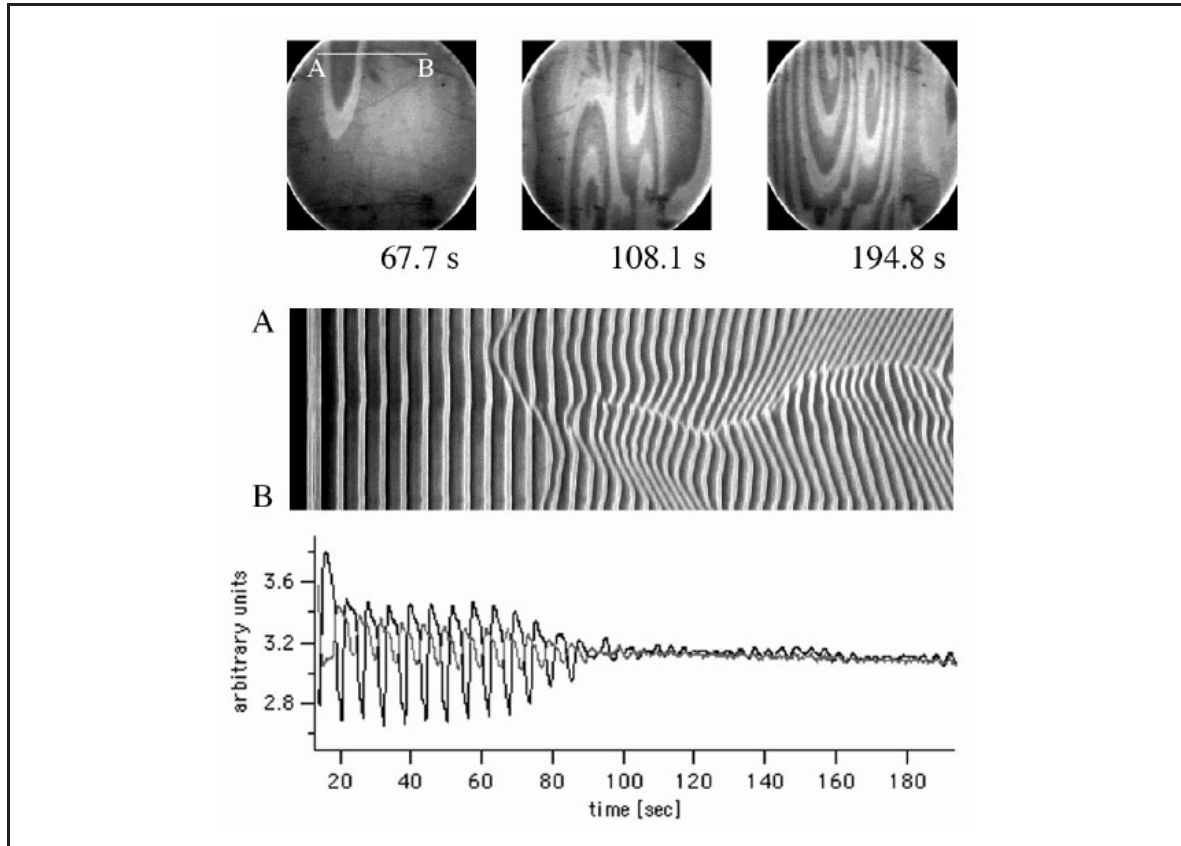


Figure 8.3: *Example of a desynchronization process. The representation is the same as in Fig. 8.2. The feedback parameters are  $\mu = 0.4 \times 10^{-5}$  mbar and  $\tau = 3.8$  s. From Ref. [162].*

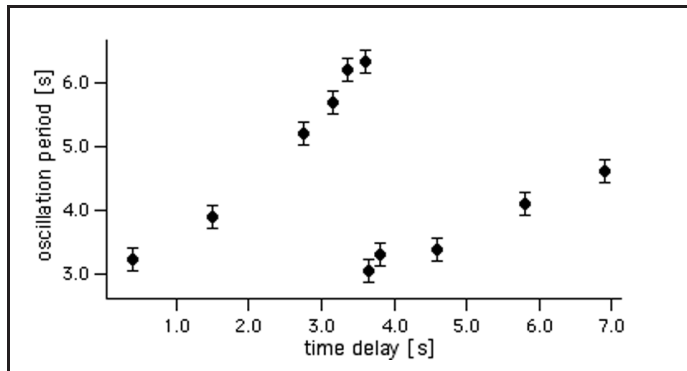


Figure 8.4: *Global oscillation period of the system for different time delays. The feedback intensity is fixed,  $\mu = 0.4 \times 10^{-5}$  mbar. From Ref. [162].*

before the breakdown of global oscillations occurred. As the delay is increased, at first the period also increases. At the transition from desynchronization to synchronization taking place at  $\tau = 3.7$  s, a jump of the period to one half of its previous value occurs, which abruptly changes the phase relation between the global oscillations and the feedback signal. The change of the phase relation is thus responsible for the transition between nonuniform and uniform spatial patterns.

### 8.1.2 Cluster patterns

In further series of experiments, the delay was kept constant and only the feedback intensity has been changed. Such measurements investigated the behavior starting from the desynchronization regime at  $\tau < 0.5$  s. Significant hysteresis effects occurred upon change of the feedback intensity. When  $\mu$  was increased from low values, the system showed at first nonuniform traveling wave patterns. Upon further increase, the desynchronizing effect disappeared and uniform oscillations were observed. However, when  $\mu$  was again decreased from the uniform state, cluster patterns arose in an intermediate range of the feedback intensity ( $\mu \approx 3.5 \times 10^{-5}$  mbar). They transformed into traveling wave patterns when the feedback intensity was further lowered.

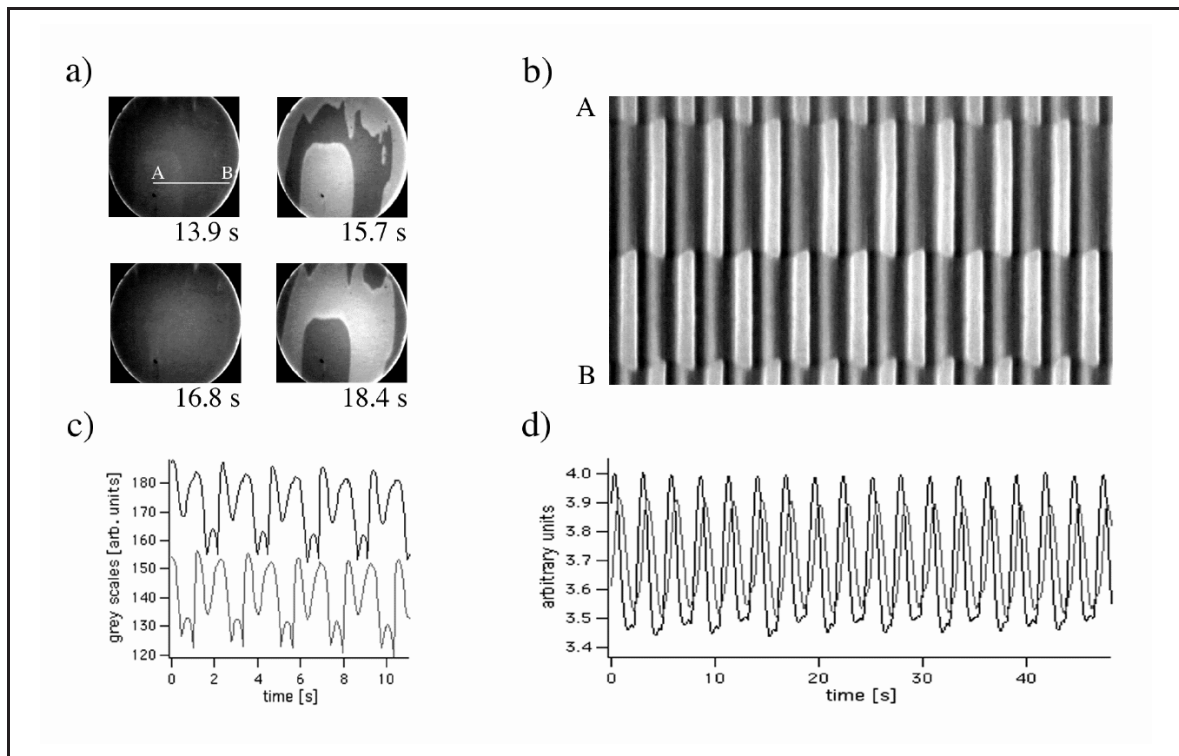


Figure 8.5: Typical example of oscillatory clusters. (a) Four snapshots of PEEM images during one oscillation period. The field-of-view is  $350\mu\text{m}$  in diameter. (b) Space-time plot along the line AB indicated in the first PEEM image. (c) Temporal variations of the local PEEM intensity within the two cluster states. The gray line has been shifted downwards for clarity. (d) Temporal variations of the negative total PEEM signal  $-I$  (black line) and the CO partial pressure (gray line). The time scale is the same as in (b). The parameters are  $T = 506$  K,  $p_{\text{O}_2} = 10.0 \times 10^{-5}$  mbar,  $p_0 = 2.2 \times 10^{-5}$  mbar,  $\mu = 3.5 \times 10^{-5}$  mbar, and  $\tau = 0.45$  s.



A typical example of an experimentally observed cluster pattern is displayed in Fig. 8.5. The surface has split into large regions belonging to either one of two different dynamical states, see Fig. 8.5(a). An intrinsic spatial wavelength is missing in such a pattern. The temporal evolution of the pattern along a cross section is shown in the space-time diagram in Fig. 8.5(b). It is seen that the clusters are stable and that the interfaces between the different domains are stationary. The local oscillations within the different domains have the same shape and are shifted in phase by half an oscillation period. Thus, the observed cluster patterns are identified as phase clusters (cf. Section 6.1.4). Note that the shape of the local oscillations is complex; due to a period doubling of oscillations, subsequent oscillation maxima show an alternating magnitude, see Fig. 8.5(c).

During the formation of phase clusters, a slow movement of the interfaces between different cluster areas occurs on a time scale of several oscillation cycles. After this transient, when the interfaces have stopped their motion and the final spatial distribution of the cluster regions is reached, the total areas occupied by the anti-phase domains are almost equal or, in other words, the clusters show the state of phase balance. The phase balance becomes evident from the global oscillations of the pattern shown in Fig. 8.5(d): the evenly weighted contributions of the local anti-phase oscillations sum up to a periodic global signal of twice the frequency of local oscillations. Cluster patterns are further studied in Section 8.2.4, where similar structures are observed in feedback experiments starting from a turbulent initial reaction state.

### 8.1.3 Discussion

The above described experiments have explored the effects of global delayed feedback in a non-chaotic parameter regime of the unforced reaction. Well defined alternating synchronization and desynchronization windows occurred upon variation of the time delay in the feedback loop. While synchronous oscillations were accompanied by a periodically oscillating control signal, the process of desynchronization led to the breakdown of global oscillations. The observations qualitatively agree with the theoretical investigations presented in Section 6.1, where similar regimes of synchronization and desynchronization in dependence of the delay were seen. The experimentally observed disappearance of the desynchronization windows above a certain feedback intensity was also found in the simulations of the CO oxidation model.

An additional feedback effect was the production of phase clusters at low time delays. In experiments with CO oxidation, phase clusters represent a novel type of pattern. They were



characterized by stationary domain interfaces and period-doubled local oscillations. The total areas of the anti-phase domains were equal. Phase clusters with partly similar properties were recently observed in experiments with the light-sensitive Belousov-Zhabotinsky reaction under global feedback [41, 104] and under periodic forcing [39, 40, 42] [see also Fig. 3.3(g)]. In the model of CO oxidation, not only phase clusters, but also other types of feedback-induced clusters have been identified (cf. Section 6.1.4). Among these patterns, phase clusters formed in a relatively large region in the plane of feedback parameters. The simulated stationary phase clusters showed the experimentally observed property of phase balance. Period doubling of the local oscillations was however only observed when the simulations started from a turbulent parameter regime.

Thus, it can be concluded that except for phase flips, the experiments have shown all principle phenomena of pattern formation predicted by the model, namely synchronous oscillations, desynchronization, and clustering of oscillations. The fact that phase flips were not seen in the experiments is probably due to the existence of structural surface defects, whose activity was not yet suppressed at low feedback intensities where the formation of phase flips is expected.

## 8.2 Controlling chemical turbulence

In further experiments, the reaction parameters have been chosen in such a way that in absence of feedback, uniform oscillations were unstable and chemical turbulence spontaneously developed. To this state, global delayed feedback according to equation (7.1) was then applied. The first series of such experiments, performed at a constant value of the time delay, has been conducted by M. Kim [163]. The data evaluation and analysis of these initial experiments, and all further experimental investigations reported below have been done by myself.

### 8.2.1 Spiral-wave turbulence

Before considering the effects of global delayed feedback on chemical turbulence, the properties of this spatiotemporally chaotic state are briefly discussed. Chemical turbulence in CO oxidation on Pt(110) was first observed by Jakubith *et al.* [46] in 1990. It is found in a wide range of temperatures for an appropriate choice of the partial pressures of gases in the chamber. A characteristic property of such turbulence is the spontaneous creation of irregular wave fronts and multiple rotating spiral waves. The spiral waves repeatedly undergo

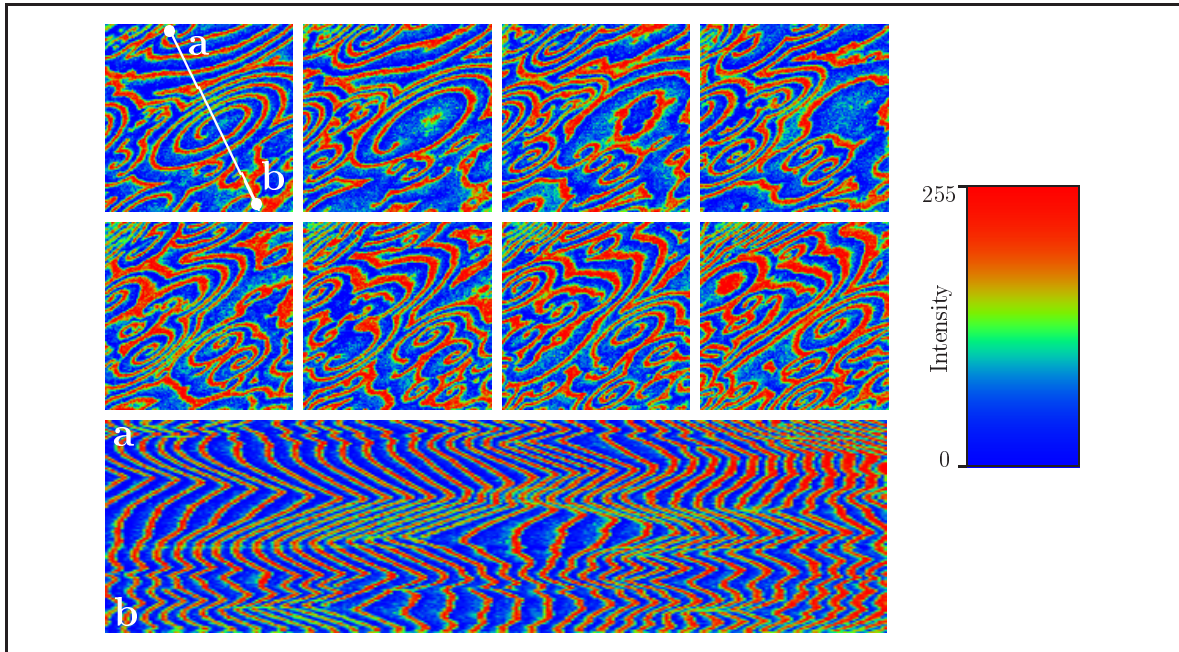


Figure 8.6: *Spiral-wave turbulence in CO oxidation experiments in absence of feedback. Displayed are eight subsequent PEEM images of size  $330 \times 330 \mu\text{m}^2$ , and the space-time diagram along the line  $ab$  indicated in the first image. The space-time diagram covers a range of 30 s; the first PEEM image is at time  $t = 13.2$  s and the time interval between subsequent images is  $\Delta t = 2.04$  s. The parameter values of temperature, oxygen partial pressure, and CO partial pressure are  $T = 509$  K,  $p_{\text{O}_2} = 40.0 \times 10^{-5}$  mbar, and  $p_{\text{CO}} = 9.1 \times 10^{-5}$  mbar.*

breakups, leading to the formation of new spiral fragments at different locations.

A typical example of the resulting state is displayed in Fig. 8.6. The PEEM images are displayed with a resolution of 256 intensity levels using the color map shown on the right in Fig. 8.6. Blue color corresponds to low local PEEM intensity and red color denotes high PEEM brightness. Green color represents intermediate intensity levels. In the top and middle rows in Fig. 8.6, eight PEEM images of the turbulent pattern are shown at equidistant time intervals. The space-time diagram below displays the temporal evolution of the pattern in the cross section along the line  $ab$  indicated in the first frame. Multiple events of spiral breakup are seen. At higher values of temperature ( $T \approx 540$  K), the turbulent state is even more developed, such that only small fragments of spiral waves are seen [cf. Fig. 4.1(d)].

### 8.2.2 Suppression of turbulence

Starting from the regime of spiral-wave turbulence, global delayed feedback according to equation (7.1) was switched on after some time, and its parameters could be varied. In experiments with a systematic variation of the feedback parameters  $\mu$  and  $\tau$ , it was observed

that turbulence could be suppressed and replaced by stable uniform oscillations for any delay time (delays up to  $\tau = 10$  s have been probed) if the feedback intensity  $\mu$  was sufficiently high (up to  $5 \times 10^{-5}$  mbar, corresponding to CO partial pressure variations of about 20 %). Usually, the synchronization threshold was significantly lower (about 5 % variations in  $p_{\text{CO}}$ ). The period of uniform oscillations was affected by the feedback and varied approximately between 3 s and 10 s, increasing for longer delays and decreasing for stronger feedbacks.

The suppression of chemical turbulence is illustrated in Fig. 8.7. The three frames in the top row present PEEM images taken at three subsequent time moments. The space-time

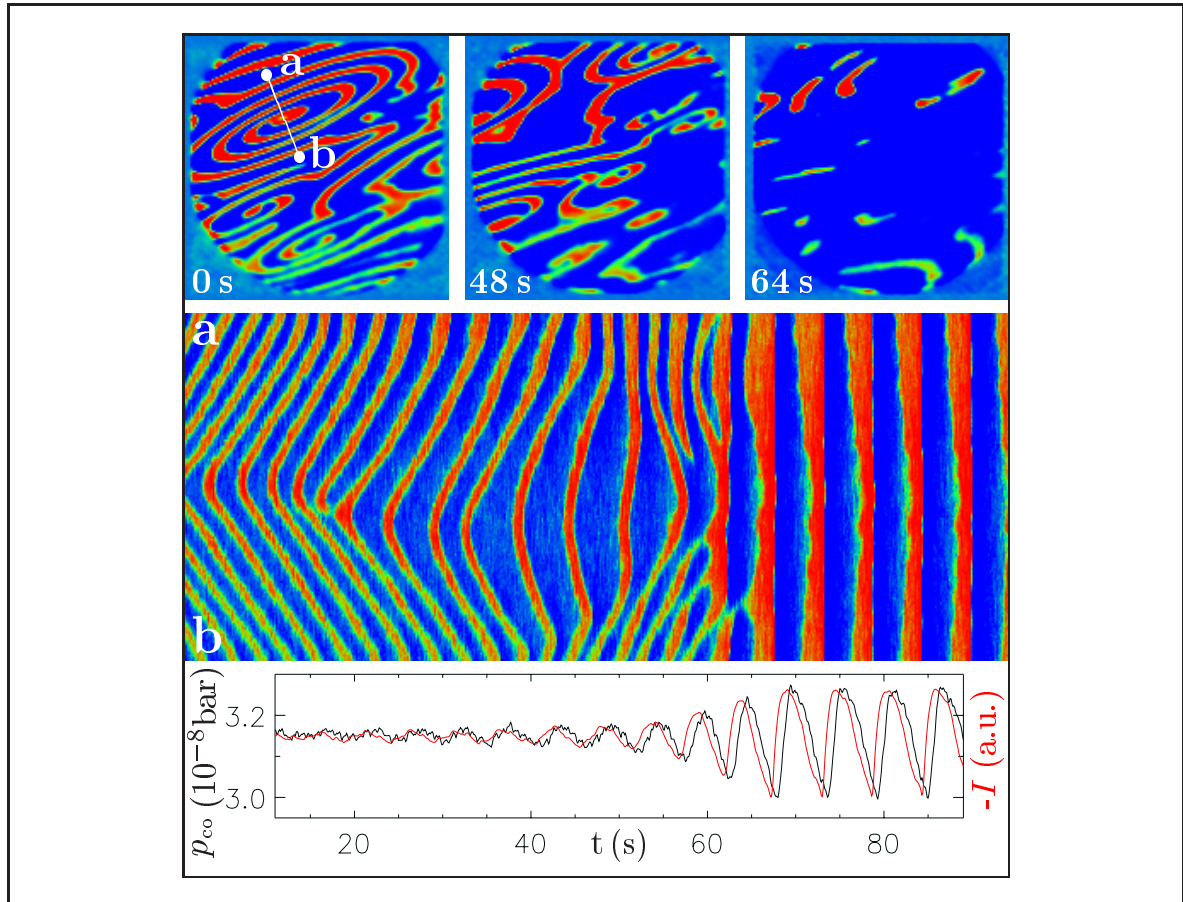


Figure 8.7: Suppression of spiral-wave turbulence. The upper row displays three subsequent PEEM images with a field-of-view of  $500\mu\text{m}$  in diameter, and the space-time diagram in the middle row show the evolution along the line  $ab$  indicated in the first image. The horizontal bar in the bottom displays the temporal variation of the CO partial pressure (black line) and the variation of the negative total PEEM intensity (red line) during the pattern evolution; the time scale is the same as in the space-time diagram. The parameter values of temperature, oxygen partial pressure, base CO pressure, feedback intensity, and delay time are, respectively:  $T = 498$  K,  $p_{\text{O}_2} = 10.0 \times 10^{-5}$  mbar,  $p_0 = 3.15 \times 10^{-5}$  mbar,  $\mu = 0.8 \times 10^{-5}$  mbar, and  $\tau = 0.8$  s. From Ref. [163].

diagram in the middle row displays the temporal pattern evolution along the line  $ab$  indicated in the first image. Below, the horizontal bar displays the variation of the negative total PEEM intensity  $-I$  (red line) and the feedback-induced modulation of the CO partial pressure (black line). The global feedback is switched on at time  $t = 0$  and its parameters are kept constant. In the initial state of spiral-wave turbulence, the integral PEEM intensity is almost constant, but then its variations (and therefore the pressure oscillations) slowly start to grow. As the feedback becomes more and more efficient, local oscillations increasingly synchronize and spiral-wave turbulence is gradually suppressed. Eventually uniform periodic oscillations are seen. The pressure variations in the reaction chamber follow the applied control signal with the delay  $\tau = 0.8$  s and reach an amplitude of about 8%.

### 8.2.3 Intermittent turbulence

Depending on the reaction and feedback parameters, the feedback does not transform spiral-wave turbulence into stable uniform oscillations, but leads to the formation of novel spatiotemporal patterns. As the feedback intensity is increased starting from zero, global oscillations set in, and turbulent spiral waves are first replaced by intermittent turbulence. This state is characterized by turbulent cascades of localized objects on a uniformly oscillating background. Intermittent turbulence is found independent of the time delay when the feedback intensity is increased from low values. Significant hysteresis is present at the transition from intermittent turbulence to uniform oscillations.

Two different types of localized turbulent objects, namely bubble structures and spiral-wave fragments, have been identified in feedback experiments. An example of the first type of intermittent turbulence is displayed in Fig. 8.8. The PEEM images in the top row are taken within one cycle of the pattern evolution. Starting from a dark, uniform state, bright spots develop at different locations. When the growing spots reach a certain size, darker regions develop in the middle of such objects and they transform into ring-shaped structures. After some time, the whole pattern fades away and is replaced by the uniform dark state. Then the entire cycle repeats. The temporal evolution of the pattern is illustrated in the space-time diagram in Fig. 8.8. Expanding bubbles are represented by triangular structures in the cross section. Examining this diagram, it is found that the bubbles can die and reproduce. When the bubbles have reproduced until many of them are found, massive annihilation occurs and only a few of them survive. Thus, an irregular behavior of repeated reproduction cascades is observed. In a sequence of PEEM images taken at subsequent evolution cycles of the pattern, this behavior is reflected by a repeated alternation between system states with large and small



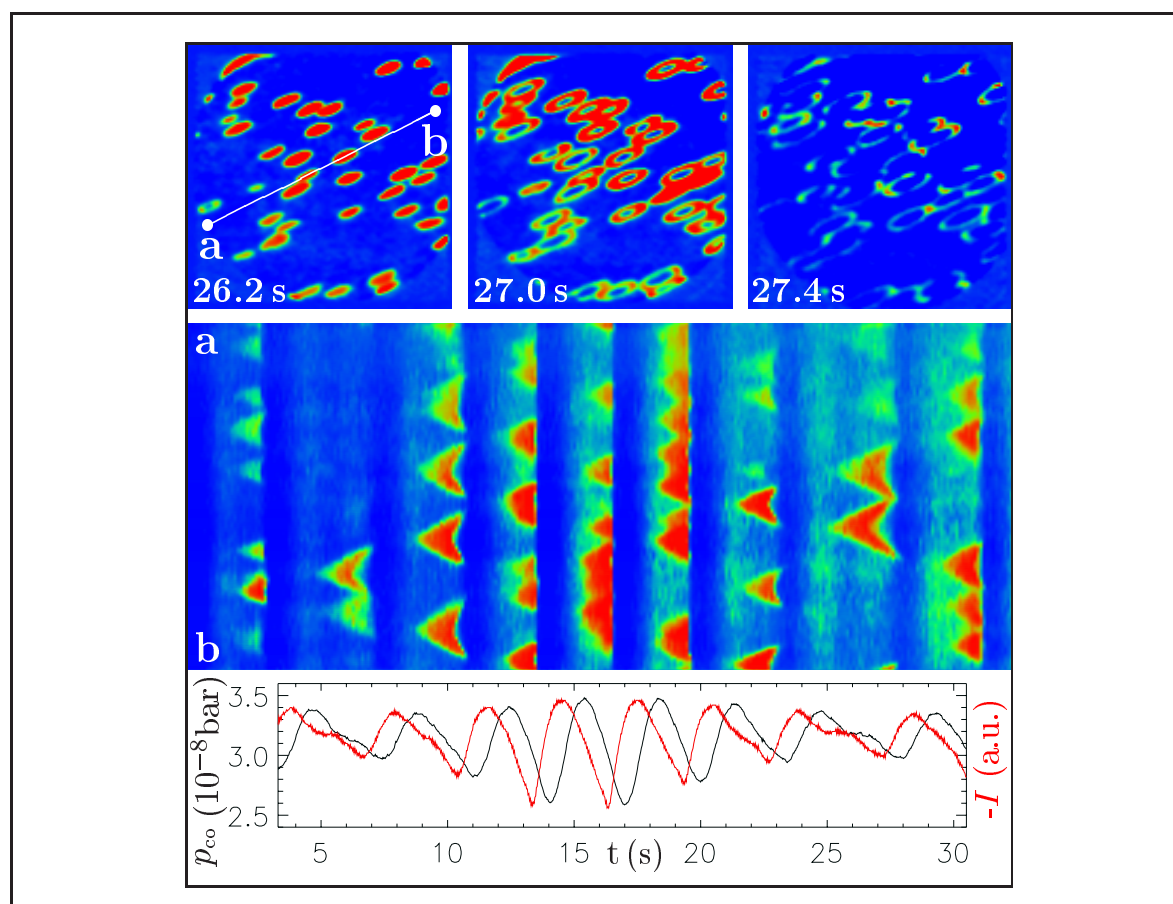


Figure 8.8: Intermittent turbulence represented by reproducing and annihilating turbulent bubbles on the background of uniform oscillations. Displayed are three subsequent PEEM images with a field-of-view of  $500\mu\text{m}$  in diameter (top), the evolution along the line *ab* indicated in the first image (middle), and the corresponding temporal variations of CO partial pressure (black line) and negative integral PEEM intensity (red line). The parameters are  $T = 495\text{ K}$ ,  $p_{\text{O}_2} = 10.0 \times 10^{-5}\text{ mbar}$ ,  $p_0 = 3.15 \times 10^{-5}\text{ mbar}$ ,  $\mu = 2.0 \times 10^{-5}\text{ mbar}$ , and  $\tau = 0.8\text{ s}$ . From Ref. [163].

fractions of the surface occupied by turbulent objects, see Fig. 8.9. In the example shown, the number and size of the turbulent bubbles typically varies on the time scale of about six evolution cycles. During intermittent turbulence, the variations of the CO partial pressure are aperiodic and are rigidly correlated with the evolution cycles of the pattern, see the curves below the space-time diagram in Fig. 8.8. Note the similarity between the intermittent regime described above and the corresponding state found in the model of CO oxidation (cf. Section 6.2.3), where reproduction cascades of turbulent bubbles on a uniformly oscillating background and the mutual annihilation of such objects were also observed.

In addition to the turbulent bubble structures, a similar state of intermittent turbulence characterized by localized fragments of spiral waves has been also observed. The latter state

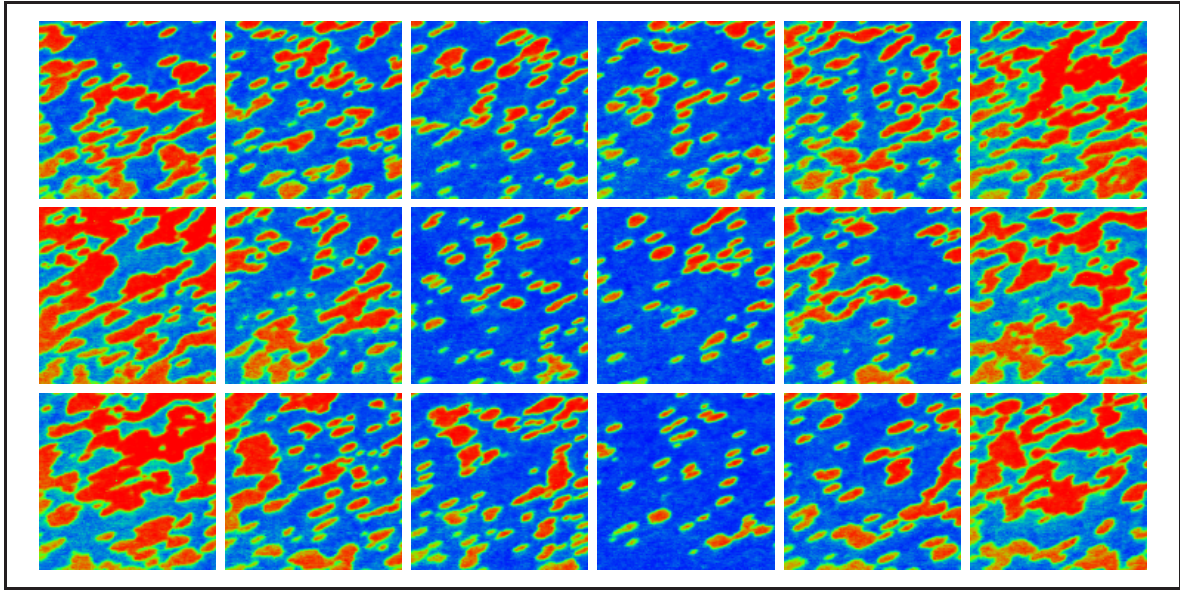


Figure 8.9: Subsequent PEEM images of turbulent bubbles on the background of uniform oscillations (from left to right and top to bottom). A snapshot of size  $360 \times 360 \mu\text{m}^2$  is shown each evolution cycle of the pattern ( $\Delta t \approx 3.5 \text{ s}$ ). The parameters are as in Fig. 8.8.

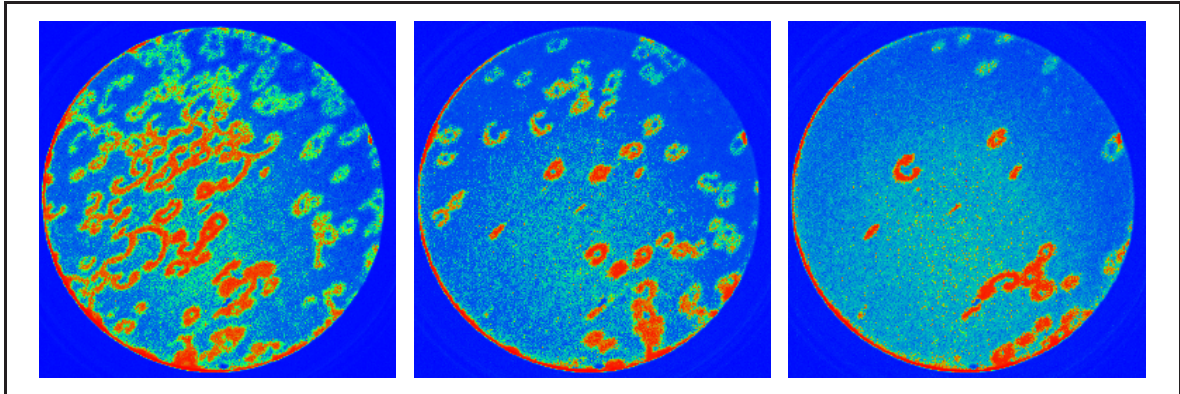


Figure 8.10: Intermittent turbulence represented by small localized spirals on the background of uniform oscillations. The PEEM images are snapshots at different points in time with a field-of-view of  $500 \mu\text{m}$  in diameter. The time interval between the first and the second frame is  $\Delta t = 20.4 \text{ s}$  and the interval between the second and third frame is  $\Delta t = 5.2 \text{ s}$ . The parameters are  $T = 537 \text{ K}$ ,  $p_{\text{O}_2} = 40.0 \times 10^{-5} \text{ mbar}$ ,  $p_0 = 11.4 \times 10^{-5} \text{ mbar}$ ,  $\mu = 3.0 \times 10^{-5} \text{ mbar}$ , and  $\tau = 0.7 \text{ s}$ .

predominantly occurs at higher values of temperature, where chemical turbulence in absence of feedback is more strongly developed and consists of many fragments of small rotating spirals [cf. Fig. 4.1(d)]. During intermittent turbulence, the localized spirals undergo similar evolution cycles as the bubble structures. They also reproduce until they occupy almost the entire monitored surface area, and then annihilate such that only few of them survive. Typical PEEM images of spiral-wave fragments on the background of uniform oscillations are

displayed in Fig. 8.10.

By further increasing the feedback intensity from the states of intermittent turbulence, additional spatiotemporal patterns are observed below the transition to uniform oscillations for delays in the interval  $0.5\text{ s} < \tau < 1.0\text{ s}$ . The precise stability regions of these patterns – two-phase clusters, standing waves, and irregular arrays of cells – strongly depend on the choice of temperature and partial pressures and have not been systematically determined. The different types of observed patterns are discussed below.

### 8.2.4 Cluster patterns

Cluster patterns forced from turbulence are similar to those induced by the feedback in the non-chaotic regime. The surface divides into large domains in which oscillations are shifted

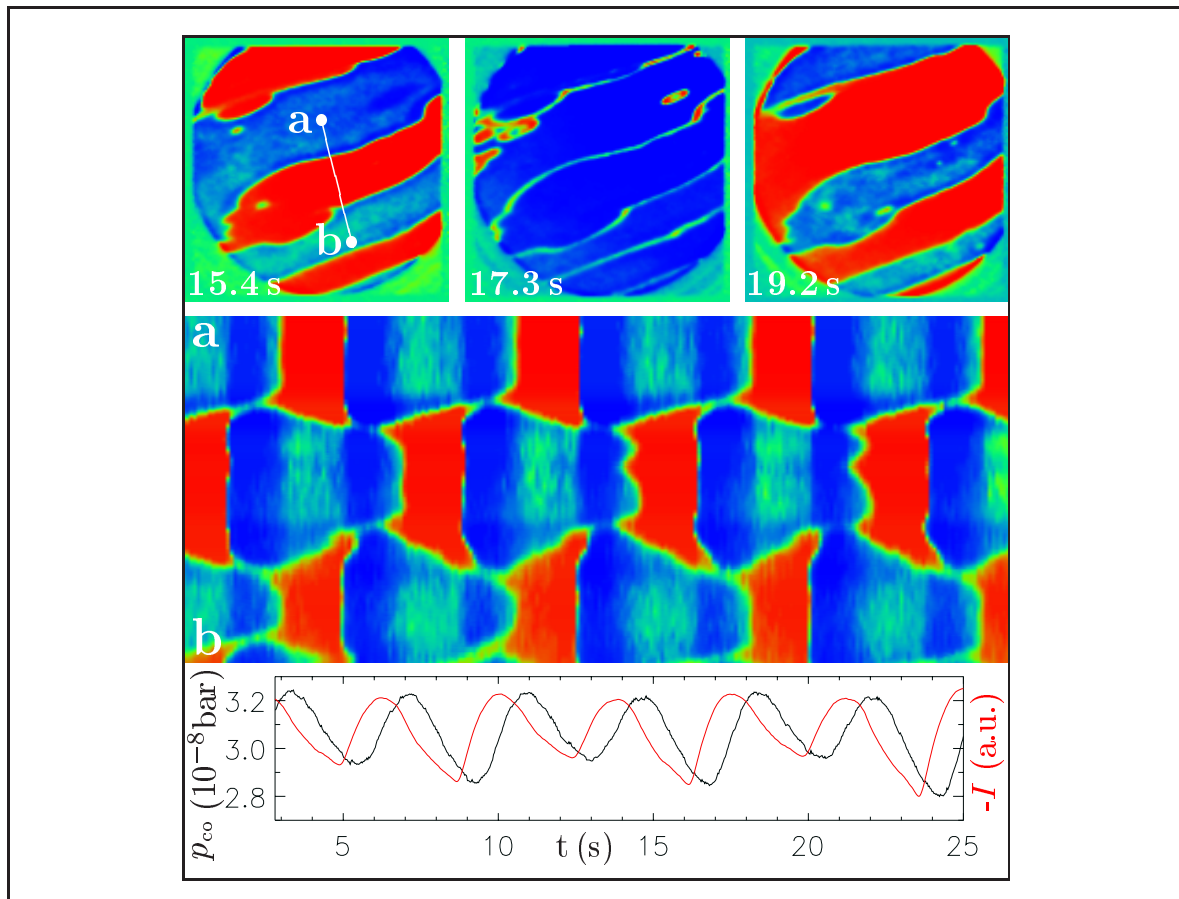


Figure 8.11: Two-phase clusters. Displayed are three subsequent PEEM images with a field-of-view of  $500\mu\text{m}$  in diameter (top), the evolution along the line  $ab$  indicated in the first image (middle), and the corresponding temporal variations of CO partial pressure (black line) and negative integral PEEM intensity (red line). The parameters are  $T = 500\text{ K}$ ,  $p_{\text{O}_2} = 10.0 \times 10^{-5}\text{ mbar}$ ,  $p_0 = 3.07 \times 10^{-5}\text{ mbar}$ ,  $\mu = 0.6 \times 10^{-5}\text{ mbar}$ , and  $\tau = 0.8\text{ s}$ . From Ref. [163].



by half a period. Usually, each of the two anti-phase clusters occupies multiple spatial domains on the surface. A typical example of phase clusters forced from turbulence is displayed in Fig. 8.11. In the top row, three snapshots taken within a single oscillation cycle of the pattern are shown. Compared to the first image, predominantly CO covered and oxygen covered regions have approximately interchanged half an oscillation period later, as seen in the third frame. At a given time moment, the total size of the opposite phase domains is approximately balanced within the monitored surface area. The space-time diagram reveals that the shape of cluster domains undergoes small periodic variations. This breathing mode is rigidly correlated with the period of local oscillations in the pattern. The spatial distribution of the different domains is almost repeated after each oscillation period, see Fig. 8.12 for a sequence of two-dimensional snapshots of the pattern.

Figure 8.13 displays the temporal variations of the PEEM intensity at two sample points located within the opposite phase domains. As it was also observed in Section 8.1.2, each maximum of PEEM intensity in the two curves is followed by a second, smaller peak, which

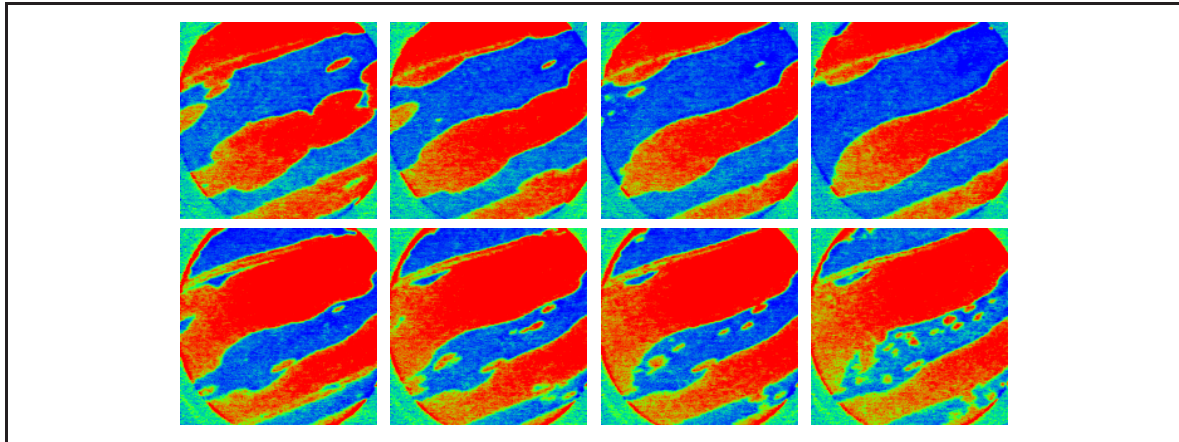


Figure 8.12: Subsequent PEEM images of phase clusters. Pairs of snapshots displayed in the upper and lower row are half an oscillation period apart, and the time interval between individual frames within each row is a full period ( $\Delta t = 7.5$  s). The parameters are as in Fig. 8.11.

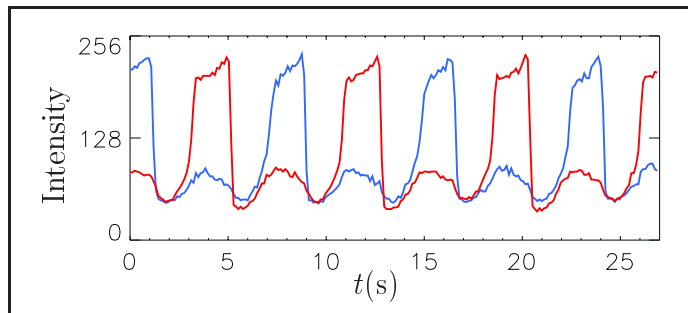


Figure 8.13: Temporal variations of the PEEM intensity at two sample points located within different cluster domains. The same parameters as in Fig. 8.11.



indicates period-doubling of local oscillations. The full oscillation period is about twice that of uniform oscillations occurring at a slightly increased feedback intensity. By looking at the time series of the local oscillations at sample points located within the domain interfaces, it has been found that the difference between subsequent oscillation maxima is strongly decreased there. The difference nearly vanishes in the center of an interface where the oscillations are almost simple periodic and have a medium amplitude. Thus, the properties of the phase fronts in the experimentally observed phase clusters agree well with the theoretical predictions for phase clusters with period-doubled oscillations (see Section 6.2.4).

### 8.2.5 Standing waves

Standing waves are displayed in Fig. 8.14. In this pattern, bright stripes repeatedly develop from the dark uniform state. The stripes are only visible during relatively short intervals of each oscillation cycle. They form a spatially periodic array and, depending on the chosen parameters, have a wavelength of roughly  $20 - 50\mu\text{m}$ . The space-time diagram reveals that the locations of stripes at subsequent oscillation cycles are shifted, and a new stripe develops in the middle between two stripes seen in the previous cycle. Thus, the initial pattern is repeated after two periods of local oscillations. The periodic emergence of the spatial structure is rigidly correlated with the variations of the CO partial pressure in the chamber.

Standing waves with similar properties have been previously observed in CO oxidation on Pt(110) due to effects of intrinsic global gas phase coupling [46, 153] [see Fig. 4.1(c)]. In those studies, they were seen only at relatively high temperatures (540 – 550 K), while in the experiments reported here, such structures have been observed also at significantly lower temperature values (down to  $T = 505\text{ K}$  in the example shown in Fig. 8.14). Another difference is that under intrinsic global coupling, usually only a part of the catalytic surface was covered by the pattern of standing waves, while the rest of the area was in the state of uniform oscillations [153]. The pattern was always perfectly synchronized with the uniform oscillations and immediately broke down when the oscillations disappeared. Therefore, it was concluded that via the gas phase, uniform oscillations on other parts of the surface provided external forcing that acted on the standing waves and stabilized this pattern. In the presently reported experiments with artificial global feedback, uniformly oscillating regions were not necessary, and standing waves usually occupied the entire monitored surface area. The required driving force could be simply generated by choosing a sufficiently large feedback intensity. The repeated alternation of the stripe positions at subsequent oscillation cycles has been explained in the previous studies [46, 153] by periodic reflective collisions of traveling

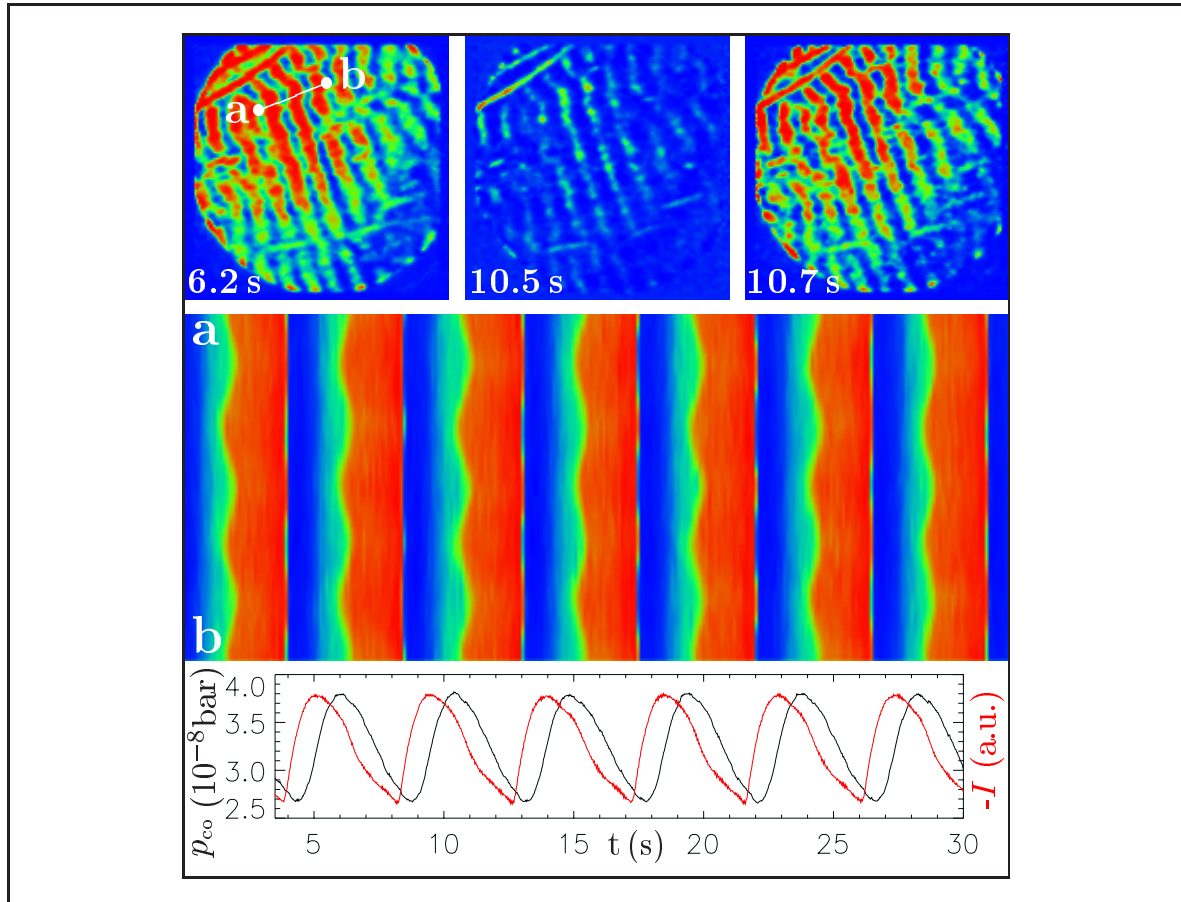


Figure 8.14: Standing waves with an intrinsic wavelength. Displayed are three subsequent PEEM images with a field-of-view of  $500\mu\text{m}$  in diameter (top), the evolution along the line *ab* indicated in the first image (middle), and the corresponding temporal variations of CO partial pressure (black line) and negative integral PEEM intensity (red line). The parameters are  $T = 505\text{ K}$ ,  $p_{\text{O}_2} = 10.0 \times 10^{-5}\text{ mbar}$ ,  $p_0 = 3.30 \times 10^{-5}\text{ mbar}$ ,  $\mu = 1.6 \times 10^{-5}\text{ mbar}$ , and  $\tau = 0.8\text{ s}$ . From Ref. [163].

waves. The occurrence of such collisions has been addressed to the presence of subsurface oxygen. Alternating standing waves could be reproduced in the model of CO oxidation on Pt(110) only by additionally taking into account the formation of subsurface oxygen [153]. Therefore, it seems likely that a certain amount of subsurface oxygen was also present in the above described experiments.

### 8.2.6 Cellular structures

A further type of pattern seen near the transition from turbulence to uniform oscillations is represented by arrays of cells. Four snapshots of such a pattern, sampled within a single oscillation period, are displayed in Fig. 8.15. The cellular structure is visible only during two short

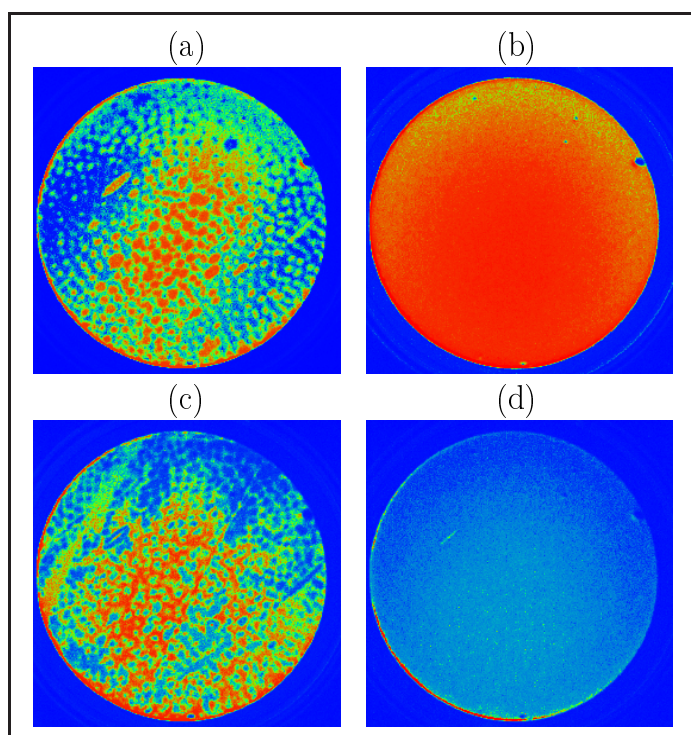


Figure 8.15: *PEEM images of cellular structures with a field-of-view of  $500\mu\text{m}$  in diameter. The time interval between subsequent frames is  $\Delta t = 1.0\text{ s}$ . The parameters are  $T = 535\text{ K}$ ,  $p_{\text{O}_2} = 40.0 \times 10^{-5}\text{ mbar}$ ,  $p_0 = 12.2 \times 10^{-5}\text{ mbar}$ ,  $\mu = 4.0 \times 10^{-5}\text{ mbar}$ , and  $\tau = 0.6\text{ s}$ .*

time intervals within each period. The appearance of cells at the transition from a predominantly oxygen covered to a mainly CO covered surface state is displayed in Fig. 8.15(a), and its recurrence during the transition back to a oxygen covered state is shown in Fig. 8.15(c). As standing waves, cellular structures usually occupy the entire imaged surface area. The local oscillations in this pattern are in harmonic resonance with the almost periodic variations of the global control signal.

Figure 8.16 displays a section of a cell array of side length  $210\mu\text{m}$  and its spatial power spectrum. As a typical observation, the arrays of cells are fairly irregular. The irregularity may be explained as a representation of phase turbulence (cf. Section 6.2.6). However, such irregularity may also, at least partly, be caused by the presence of small structural surface defects. No unambiguously regular, hexagonal cell arrays have been observed in the experiments described here.

Oscillatory cellular structures also were seen in previous measurements that employed mirror electron microscopy [126], where their presence was attributed to the action of intrinsic global gas phase coupling. The cell arrays were observed at relatively low values of temperature ( $T \approx 430\text{ K}$ ) and exhibited a temporal period of the order of 30 s and a characteristic cell size of about  $1\mu\text{m}$ . In contrast, the artificially induced cellular structures described here were found at significantly higher temperature values (525 – 550 K) and typically ex-

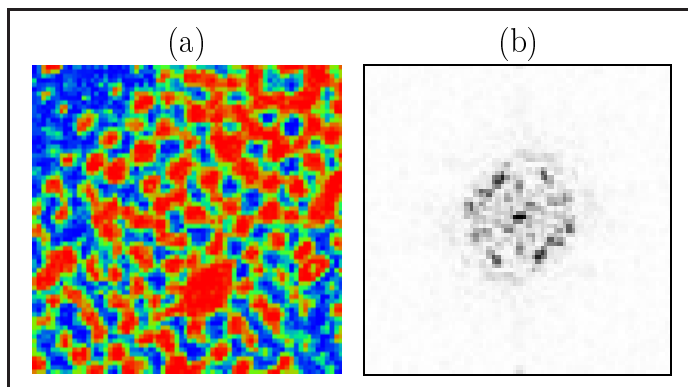


Figure 8.16: (a) *PEEM image and (b) spatial Fourier spectrum of an irregular array of cells. The same parameters as in Fig. 8.15.*

hibited an average cell size of approximately  $20\mu\text{m}$  and an oscillation period of about 4 s.

### 8.2.7 Discussion

In the above described experiments, feedback-induced pattern formation has been studied in a parameter regime where the unperturbed reaction exhibited chemical turbulence. At first, turbulence could be completely suppressed by applying global delayed feedback. After successful synchronization of local oscillations, the uniform state was maintained by a periodically varying control signal which compensated the destabilizing effect of diffusion. It is left for further investigations whether spatiotemporal chaos in the considered system can also be non-invasively controlled by means of other feedback methods such as time-delay autosynchronization (TDAS, see Section 3.2). In a preliminary study, it has been noticed that synchronization of oscillations can be also achieved using the global TDAS method, but that a small driving signal might still be required.

Moreover, a large variety of complex spatiotemporal patterns was found when global delayed feedback was used to bring the system to the boundary between regular and chaotic dynamics. Probably the most important result is the experimental observation of intermittent turbulence. This state is characterized by cascades of reproducing and annihilating turbulent bubble structures or small localized spirals on the background of uniform oscillations. In addition, phase clusters, which showed similar properties as in the non-chaotic parameter regime, could be induced. Standing waves and cellular structures represented further results of the action of global delayed feedback. The latter structures were previously also observed in CO oxidation experiments as effects of intrinsic global gas phase coupling [46, 126, 153], but their properties were then significantly different.

The experimental observations agree well with the theoretical predictions presented in Section 6.2, even though the initial turbulent state in the model of CO oxidation was

somewhat more developed than in the experimental system (e.g., in the model, spiral waves only rarely formed in the turbulent state). In both systems, turbulence could be suppressed in a wide range of feedback parameters. During intermittent turbulence, not only the formation of bubble-shaped objects on a uniformly oscillating background was indeed experimentally observed, but also their predicted reproduction cascades could be identified. Phase clusters were also observed in both systems, and showed similar properties such as stationary phase fronts, period-doubled local oscillations, and phase balance. While disordered cellular structures were found both in experiments and simulations, regular arrays of cells were not seen in the experimental system where fine tuning of the parameters is difficult and some structural surface defects are always present. In order to reproduce the experimentally observed patterns of alternating standing waves in simulations employing the CO oxidation model, it is known that additionally the formation of subsurface oxygen must be taken into account [153].

### 8.3 Pattern characterization

To further analyze the patterns observed in the previous section, a variant of the analytic signal approach [164, 165] is employed. This technique is used to transform PEEM images into the spatial distributions of phase and amplitude variables. In Section 5.3, such a transformation already has been realized for the characterization of simulated patterns. However, the developed method cannot be directly applied to the experimental data because, besides the PEEM intensity, a second variable is necessary for the projection of the dynamics. Moreover, the intensity value of the unstable steady state is not exactly known in the experiments.

The analytic signal approach can be efficiently employed to solve these problems. Using this method, a second variable is generated by means of the Hilbert transform. The dynamics are then projected into the plane spanned by the PEEM intensity and its Hilbert transform. An alternative method for the projection of the dynamics is provided by delay embedding [166, 167]. However, when the latter method was implemented, self-intersection of orbits frequently occurred in the projection plane, which resulted in difficulties for the phase definition. The delay for the embedding had to be optimized separately each time the method was applied. Therefore, the analytic signal approach was preferred.



### 8.3.1 Transformation to amplitude and phase variables

The transformation of sequences of typically 250 experimental PEEM images into the time-dependent spatial distributions of phase and amplitude variables was achieved as follows. For the local PEEM intensity  $I(\mathbf{x}, t)$  at an observation point  $\mathbf{x}$ , its Hilbert transform

$$\tilde{I}(\mathbf{x}, t) = \pi^{-1} \int_{-\infty}^{\infty} (t - t')^{-1} I(\mathbf{x}, t') dt' \quad (8.1)$$

was computed (this could be easily realized by determining the Fourier transform of  $I$ , shifting each complex Fourier coefficient by a phase of  $\pi/2$ , and performing the reverse Fourier transform [165, 168]). This was repeatedly done for all pixel points  $\mathbf{x}$  in an  $100 \times 100$  array covering the respective pattern. Using  $I(\mathbf{x}, t)$  and its Hilbert transform  $\tilde{I}(\mathbf{x}, t)$ , a complex variable

$$\zeta(\mathbf{x}, t) = I(\mathbf{x}, t) + i\tilde{I}(\mathbf{x}, t) \quad (8.2)$$

known as *analytic signal* [164] was defined.

Afterwards, the time-dependent spatial distributions of the phase  $\phi(\mathbf{x}, t)$  and amplitude  $R(\mathbf{x}, t)$  were determined from the analytic signal in the following way. The phase was directly computed as  $\phi = \arg \zeta$ , thus representing the polar angle in the plane spanned by the variables  $I$  and  $\tilde{I}$ . The amplitude was defined as  $R = \rho / \rho_{\text{ref}}(\phi)$ , where  $\rho = |\zeta|$  is the standard definition of the amplitude modulus within the analytic signal approach. The normalization to

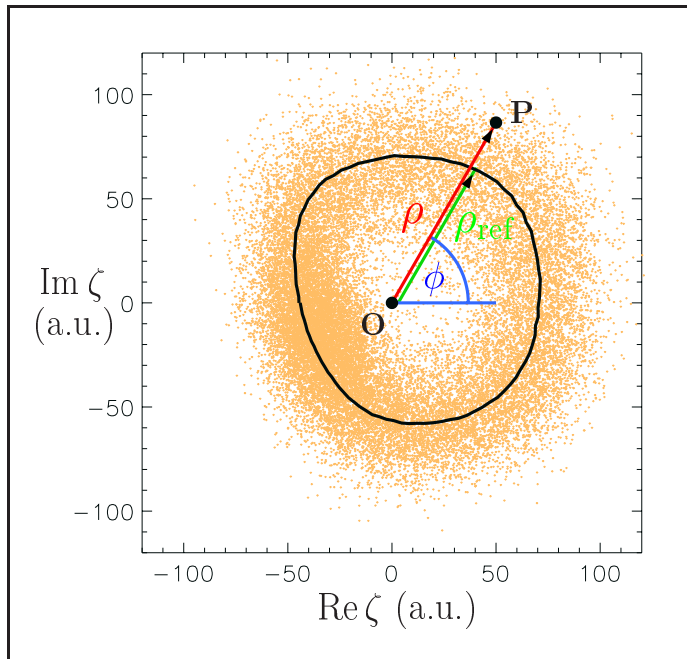


Figure 8.17: Illustration of the transformation to the amplitude  $R = \rho / \rho_{\text{ref}}(\phi)$  and phase  $\phi = \arg \zeta$  of local oscillations; the reference orbit  $\rho = \rho_{\text{ref}}(\phi)$  is indicated by the closed line.

$\rho_{\text{ref}}(\phi)$  was introduced to approximately compensate for deviations from harmonicity in the observed oscillations. To obtain  $\rho_{\text{ref}}(\phi)$ , the statistical distribution of  $\zeta(\mathbf{x}, t)$  for all  $100 \times 100$  pixels and at all 250 time moments was plotted into the complex plane, as illustrated in Fig. 8.17 for a set of spatiotemporal data representing a pattern of spiral-wave turbulence. The reference amplitude  $\rho_{\text{ref}}(\phi)$  was then determined as the statistical average of  $\rho = |\zeta|$  inside each of 200 equidistant narrow intervals of the polar angle  $\phi$ . Note that the closed curve  $\rho = \rho_{\text{ref}}(\phi)$  in the complex plane can be viewed as representing a reference orbit of the system deduced from the experimental data. In this way, a different reference orbit has been generated for each set of spatiotemporal data to which the variable transformation was applied.

### 8.3.2 Amplitude and phase patterns

By applying this technique to each type of the PEEM patterns presented in Section 8.2, spatial distributions of the phase  $\phi$  and the amplitude  $R$  in each pattern have been constructed. Snapshots of the resulting (time-dependent) distributions are displayed in Fig. 8.18. The original PEEM images are shown in the top row of Fig. 8.18. Below, the corresponding spatial distributions of phase (second row) and amplitude (third row) are displayed, using the same color map as was used in Chapter 6. Additionally, the bottom row of Fig. 8.18 shows a phase portrait of each pattern, obtained by displaying the amplitudes and phases for all resolving pixels in polar coordinates. The phase  $\phi$  of a point is represented by the polar angle and the amplitude  $R$  is the distance to the coordinate origin.

In spiral-wave turbulence [Fig. 8.18(a)], the fluctuations of amplitude and phase are strong, as indicated by the broad-band structure in the phase portrait, and the amplitude drops down in the spiral cores. For intermittent turbulence [Figs. 8.18(b) and 8.18(c)], the amplitude and the phase are almost constant in the main part of the medium where uniform oscillations take place. The amplitude is significantly decreased in the bubble-shaped objects [Fig. 8.18(b)] and small localized spirals [Fig. 8.18(c)], so that they indeed represent amplitude defects. The phase portraits of intermittent turbulence show a spot corresponding to the uniform state of the medium and a tail corresponding to the amplitude defects. In a cluster pattern [Fig. 8.18(d)], the medium breaks into the two phase states seen as spots in the phase portrait. The amplitudes in the two clusters differ because the local oscillations exhibit period-doubling. The ‘bridge’ in the phase portrait connecting the two spots corresponds to the interfaces between the cluster domains; note that the phase varies smoothly and the amplitude is not significantly reduced at the interface for such cluster patterns. In cellular



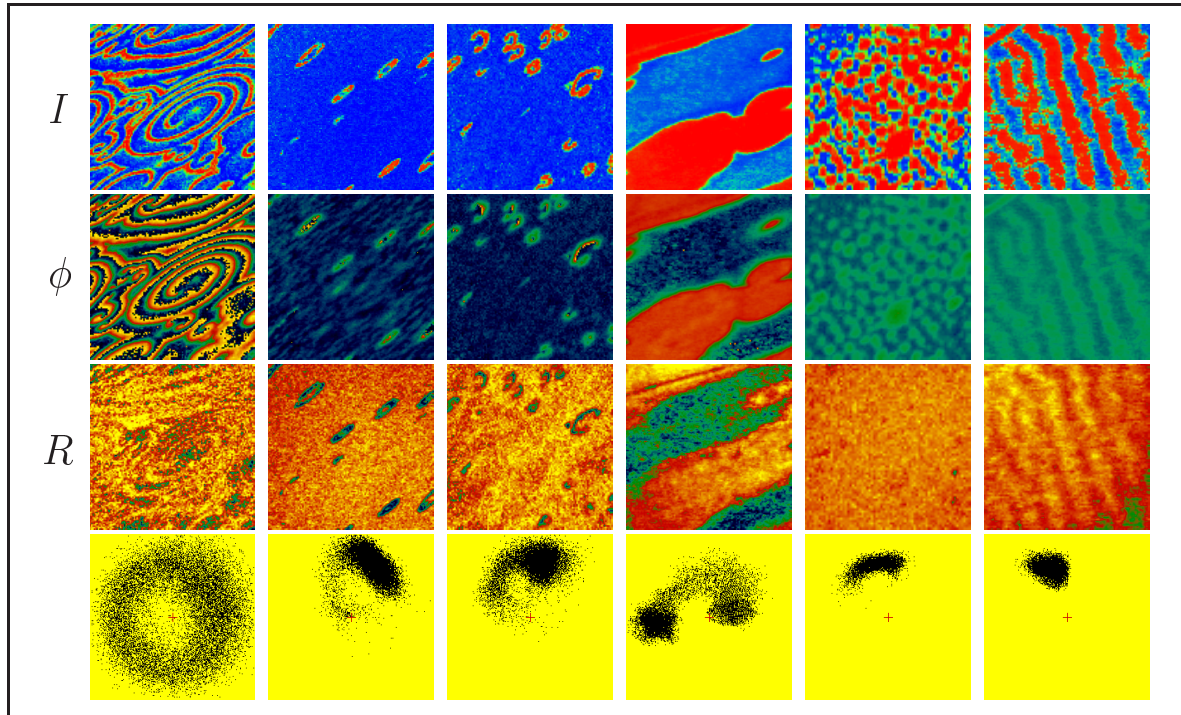


Figure 8.18: *PEEM images (top), distributions of phase (second row), amplitude (third row), and phase portraits (bottom) for several typical patterns observed in CO oxidation experiments. The values of temperature (K), oxygen partial pressure ( $10^{-5}$  mbar), base CO pressure  $p_0$  ( $10^{-5}$  mbar), feedback intensity  $\mu$  ( $10^{-5}$  mbar) and delay time  $\tau$  (s) are, respectively: (a) 548, 40.0, 12.3, 0, 0; (b) 540, 40.0, 13.1, 1.7, 0.7; (c) 537, 40.0, 11.4, 3.0, 0.7; (d) 500, 10.0, 3.1, 0.6, 0.8; (e) 535, 40.0, 12.2, 4.0, 0.6; and (f) 505, 10.0, 3.3, 1.6, 0.8. The side length of images is (a,b)  $360\mu\text{m}$ , (c,d)  $330\mu\text{m}$ , (e)  $210\mu\text{m}$ , and (f)  $270\mu\text{m}$ .*

structures [Fig. 8.18(e)], small phase modulations are observed, while the amplitude remains approximately constant. In standing waves [Fig. 8.18(f)], both the phase and the amplitude are periodically modulated.

The amplitude and phase patterns shown in Fig. 8.18 can be directly compared to the simulated patterns displayed in Fig. 6.36. The simulations successfully reproduce the principal amplitude and phase properties of the corresponding structures seen in the experiments, except that simulated cellular structures are also visible as weak variations in the amplitude distributions.

As pointed out in Section 3.2.2, similar phenomena were also reported in the general studies performed in the framework of the complex Ginzburg-Landau equation [36, 37, 112–114], where clusters, oscillatory cellular arrays, and intermittent turbulence characterized by cascades of bubble-shaped objects were also seen. The similarity between the behavior found in experiments, simulations of a realistic model, and the amplitude equation indicates that the

observed effects of pattern formation may be typical for a broad class of reaction-diffusion systems.



---

## Chapter 9

### Pattern formation under periodic forcing

---

The effects of periodic external forcing in CO oxidation on Pt(110) were first investigated shortly after self-sustained oscillations had been discovered in this reaction [75, 140]. At that time, the reaction state of the surface was monitored with a Kelvin probe, measuring the work function averaged over the entire surface. In these early experiments, small periodic variations of the oxygen partial pressure in the reaction chamber up to 1.5% were applied. The unforced system showed stable limit cycle oscillations. The observed phenomena included harmonic, subharmonic, and superharmonic entrainment, and quasiperiodic oscillations outside the frequency locked bands. Spatial patterns, which possibly formed on the catalytic surface during these experiments, could however not yet be resolved. A later study which employed PEEM to monitor pattern formation has investigated the role played by periodic forcing only with respect to the formation of standing waves [153]. The experiments presented in this chapter show that several other structures can be also induced by this method.

#### 9.1 Controlling chemical turbulence

In the experiments presented below, pattern formation in CO oxidation on Pt(110) has been investigated in the case where the unforced reaction displayed chemical turbulence. The initial reaction state was similar as in the experiments with global delayed feedback presented in Section 8.2 (refer to Fig. 8.6 for an example). After spiral-wave turbulence had spontaneously developed, the CO partial pressure in the reaction chamber was periodically modulated with a nearly harmonic signal of amplitude  $\gamma$  and frequency  $\omega_f$ , while its temporal average  $p_0$  was kept constant. The effects of periodic forcing were investigated in the frequency range  $0.2\text{ Hz} \leq \omega_f \leq 0.5\text{ Hz}$ .

### 9.1.1 Uniform oscillations

In such experiments, a rather large relative variation of CO partial pressure (about 10-20%, depending on temperature and base partial pressures) was necessary in order to suppress turbulence and to observe frequency locked patterns. In this range of the forcing amplitude, the resonance structure of the system was clearly dominated by harmonic entrainment. Within the 1:1 resonance, local oscillations at all resolving pixels in a pattern synchronized and locked to the forcing frequency.

In the previous experiments which employed the Kelvin probe [75], it was reported that, starting from simple periodic oscillations of frequency  $\omega = \omega_f$ , period doubling occurred under an increase of  $\omega_f$ . Such behavior, resulting in uniform oscillations with alternating maxima at consecutive cycles of the forcing, has also been observed in the present study. Harmonic resonance of period-two oscillations is more accurately denoted as 2:2 entrainment, indicating that two different response cycles of the system lie within two periods of the forcing.

### 9.1.2 Irregular oscillatory stripes

In addition to uniform oscillations, different resonant spatiotemporal patterns have been also observed. First the attention is focused on the type of structure displayed in Fig. 9.1. This pattern consists of an array of stripes which are mainly oriented into the surface direction with fast CO diffusion (the  $[1\bar{1}0]$  orientation of the Pt(110) single crystal surface). Note that multiple dislocations, represented by the regions where individual stripes merge to form a fork-like structure, are present in this pattern.

The spatial structure is seen only during a certain time interval of each oscillation cycle. After one forcing period, when the pattern appears again, the locations of the stripes are shifted, and new stripes are present in the middle between those seen at the previous cycle (compare the first and the third image in the top row of Fig. 9.1). The initial pattern is repeated after two forcing periods. The curves below the space-time diagram in Fig. 9.1 show the temporal evolution of the pattern at two different points, which are located in the centers of two alternating stripes. The locations are indicated by arrows in the space-time diagram. It is seen that the oscillations have the same shape and frequency ( $\omega = \omega_f/2$ ), but are phase-shifted by half a period.

To further analyze resonant patterns, the frequency demodulation technique [40] described in Section 3.1 is employed. In a first step, the temporal power spectrum for each

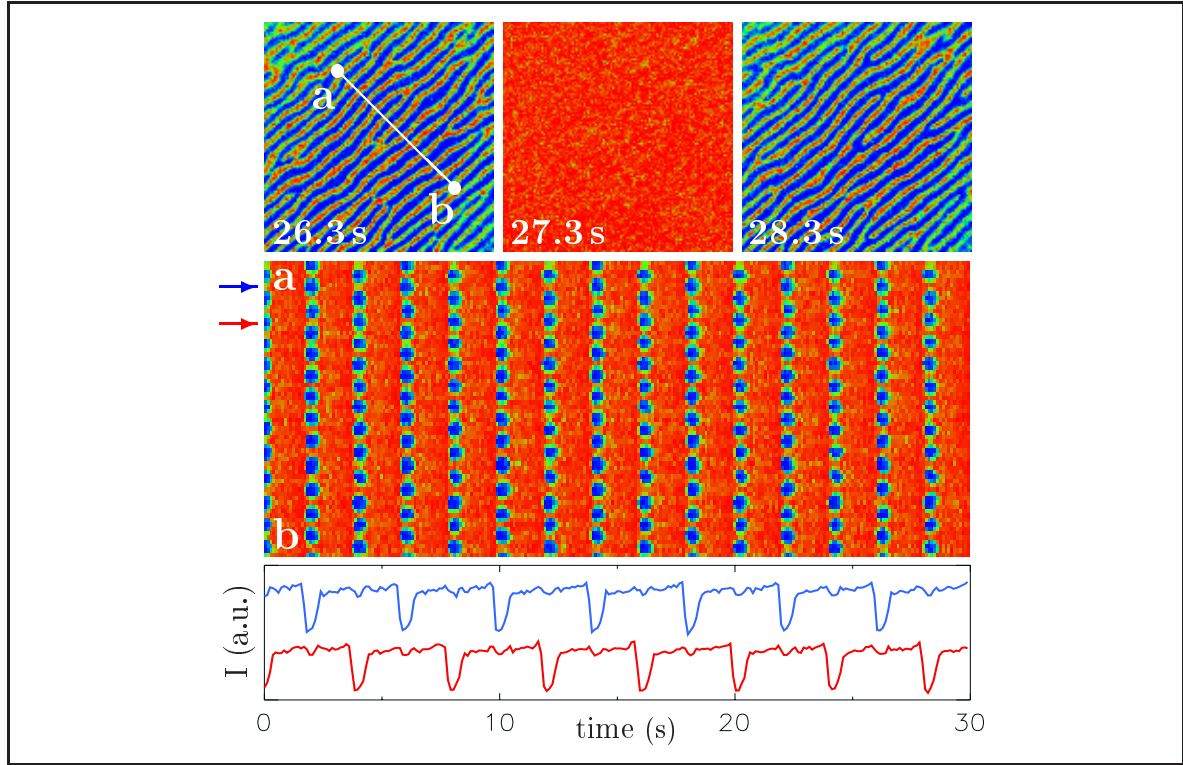


Figure 9.1: *Irregular oscillatory stripes in experiments with periodic forcing.* Displayed are three subsequent PEEM images of size  $240 \times 240 \mu\text{m}^2$  at a time interval of half a forcing period (top), the evolution along the line  $ab$  indicated in the first image (middle), and the temporal variation of the local PEEM intensity at two different points in the space-time diagram indicated by arrows (bottom). The employed color map is the same as the one used in Chapter 8. The reaction parameters are  $T = 531 \text{ K}$ ,  $p_{\text{O}_2} = 40.0 \times 10^{-5} \text{ mbar}$ , and  $p_0 = 10.4 \times 10^{-5} \text{ mbar}$ . The forcing amplitude is  $\gamma = 20.2 \%$  and the forcing frequency is  $\omega_f/2\pi = 0.50 \text{ Hz}$ .

resolving pixel in a pattern is determined. This is done by calculating the fast Fourier transform of the local time series at each pixel. The average over all pixel provides the power spectrum of the entire pattern.

The result for the pattern of irregular stripes is displayed in Fig. 9.2. The average spectrum shows distinct peaks at the frequencies  $\omega_f/2$  and  $\omega_f$ . Higher order harmonics are also present.

To determine the spatial information contained in the different excited temporal modes separately, the complex Fourier coefficients  $a(x, y)$  associated with the  $\omega_f$ -mode and the  $\omega_f/2$ -mode are extracted from the Fourier spectrum at each pixel  $(x, y)$  in the pattern. By plotting the spatial distributions of the quantities  $\arg(a)$  and  $|a|$ , phase and amplitude images are obtained for each associated frequency.

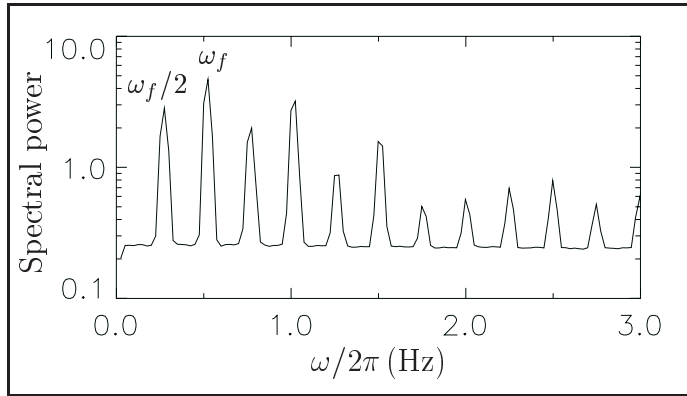


Figure 9.2: *Temporal power spectrum of a pattern of irregular stripes, determined by fast Fourier transformation of the time series of 1000 PEEM images ( $100 \times 100$  pixels) sampled at a rate of 25 images per second. The same parameters as in Fig. 9.1.*

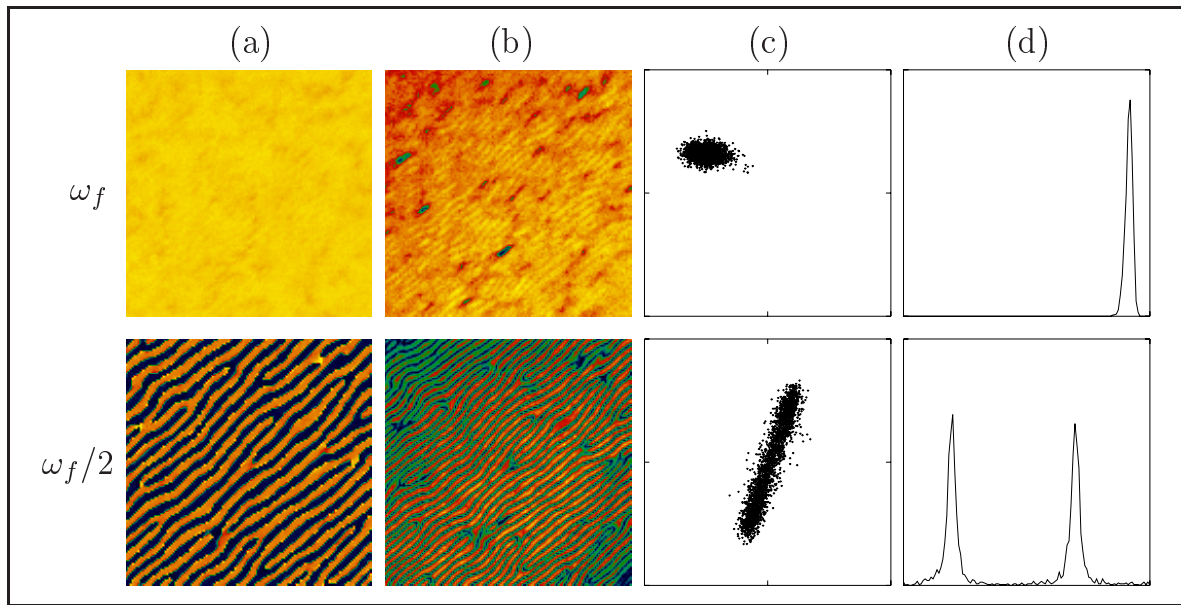


Figure 9.3: (a) Phase patterns, (b) amplitude patterns, (c) phase portraits, and (d) phase histograms of a pattern of irregular stripes demodulated at the frequencies  $\omega_f$  (top row) and  $\omega_f/2$  (bottom row). In the phase portraits, each of the coefficients  $a$  is plotted into the complex plane. The phase histograms show the distributions of phases  $\arg(a)$ ; the abscissa range is  $[0, 2\pi]$  and the ordinate range is arbitrary. The amplitude and phase images are plotted with the same color map as in Section 8.3.2.

Such phase and amplitude patterns are displayed in Figs. 9.3(a) and 9.3(b), respectively. The plots in the top row of Fig. 9.3 show the response of the system at the frequency  $\omega_f$ , and the bottom row shows the results of a frequency demodulation at  $\omega_f/2$ . Phase portraits and phase angle histograms for the different frequencies are further displayed in Figs. 9.3(c) and 9.3(d), respectively.

Examining Fig. 9.3, one finds that the spatial pattern associated with the mode  $\omega_f$  is almost uniform. Spatial variations are observed only as depletions of the amplitude field at some locations where structural defects exist (the regions in the pattern where different



stripes merge). In contrast, the array of stripes is nicely seen in the patterns associated with the mode  $\omega_f/2$ . The corresponding phase image shows an array of yellow and blue stripes which are of opposite phase. In the amplitude pattern, it is seen that the oscillation magnitude in the mode  $\omega_f/2$  is greatly reduced along the boundaries between the  $\pi$ -shifted stripes. Structural defects are visible in this amplitude image as well. In the corresponding phase portrait, the pixels are spread along a straight line that crosses the origin of the complex plane, indicating that the oscillation magnitude actually vanishes along the lines that separate neighbored  $\pi$ -shifted stripes. The two phase states are evenly weighted within the pattern, see the phase histogram. Thus, by means of frequency demodulation it is found that, though significant power is present in the harmonic mode, the observed irregular arrays of stripes are solely due to 2:1 entrainment and consist of two phase-locked,  $\pi$ -shifted phase states.

The sequence of PEEM images displayed in Fig. 9.4 illustrates the growth mechanism of irregular oscillatory stripes. The pattern originates from small-amplitude uniform oscillations around a mainly CO covered state. The predominantly oxygen covered state is only reached at certain locations on the surface where fragments of stripes first appear. During the further evolution, at such locations the structure grows stripe by stripe, until it occupies the entire imaged surface area. As time goes on, the number of dislocations in the pattern slowly decreases and a more regular, quasi-stationary configuration is established (see Fig. 9.1 for the final state of the shown example).

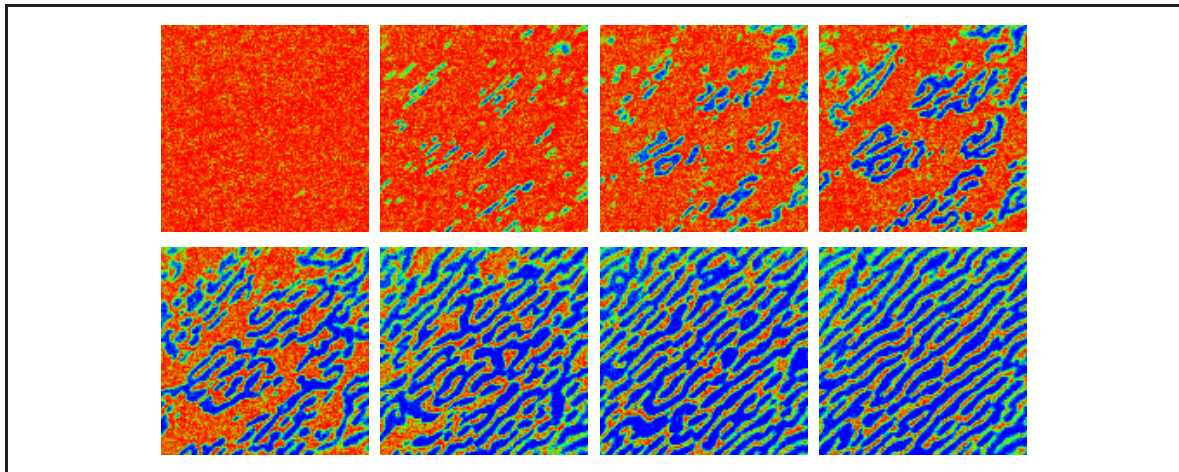


Figure 9.4: Development of irregular stripe patterns. The time interval between subsequent PEEM images (from left to right) is  $\Delta t = 2.0$  s and corresponds to one period of the driving force. The same parameters as in Fig. 9.1.

Note that the growth mechanism of irregular stripes is different from that of standing waves in the same system. The development of standing waves was previously studied in detail in experiments with intrinsic global gas-phase coupling [153]. In contrast to irregular stripes, standing waves develop as small modulations of large-amplitude uniform oscillations and are closely related to traveling waves, to which they transform upon a small change of experimental conditions.

### 9.1.3 Clusters with coexistent resonances

A further type of frequency locked pattern can be attributed to the simultaneous excitation of different resonances. In a region of parameter space where the harmonic 1:1 and the sub-harmonic 2:1 resonances possibly overlapped, clusters with coexistent resonances have been observed, see Fig. 9.5 for an example.

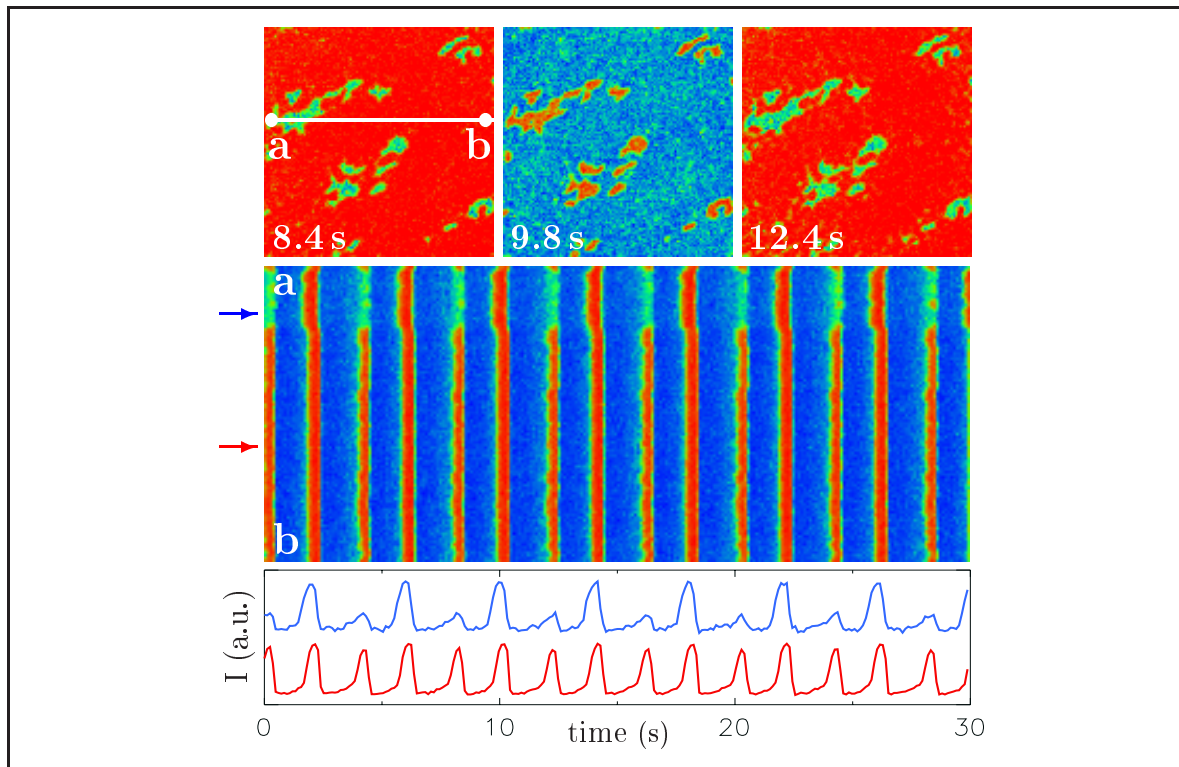


Figure 9.5: Amplitude clusters. Displayed are three subsequent PEEM images of size  $330 \times 330 \mu\text{m}^2$  (top), the evolution along the line  $ab$  indicated in the first image (middle), and the temporal variation of the local PEEM intensity at two different points in the space-time diagram indicated by arrows (bottom). The reaction parameters are  $T = 537 \text{ K}$ ,  $p_{\text{O}_2} = 40.0 \times 10^{-5} \text{ mbar}$ , and  $p_0 = 10.9 \times 10^{-5} \text{ mbar}$ . The forcing amplitude is  $\gamma = 11.0 \%$  and the forcing frequency is  $\omega_f/2\pi = 0.50 \text{ Hz}$ .

The three PEEM images in the top row of Fig. 9.5 show that several localized spatial domains exist in such a pattern. Though such domains have a complex, irregular shape, their boundaries are almost stationary during several periods of oscillations. As it was also observed in previous patterns, the spatial structure is only seen during a relatively short fraction of each oscillation cycle. The initial pattern (first frame) repeats after two forcing periods (third frame). Within this time interval, a reversed state appears for a short time (second frame in Fig. 9.5), where bright and dark regions in the pattern have interchanged.

The space-time diagram shown in the middle of Fig. 9.5 reveals that the underlying temporal behavior within the domains significantly differs from that of their background. For comparison, below the space-time diagram the temporal variation of the PEEM intensity at two sample points is shown, one located within the domains and one outside. In both regions, period-doubled oscillations characterized by an alternating magnitude of subsequent maxima are found; however, inside the domains, the difference between consecutive maxima is much more pronounced. By applying the frequency demodulation technique to this pattern, one finds that inside the small domains, the  $\omega_f/2$ -mode in the power spectrum of the local time series is more strongly excited than the mode with frequency  $\omega_f$  (not shown in Fig. 9.5). The opposite is true for pixels located outside the domains, where more power is concentrated in the harmonic mode.

### 9.1.4 Intermittent turbulence

By fixing the forcing amplitude below the transition to frequency locked behavior, also different types of non-resonant spatiotemporal patterns could be observed. In a wide range of forcing parameters near the harmonic resonance, period forcing transformed spiral-wave turbulence into intermittent turbulence, characterized by the presence of localized turbulent bubbles on a uniformly oscillating background. Such a state has been also observed under global delayed feedback (cf. Section 8.2.3); note that in the latter case, however, an aperiodic control signal was then generated.

A series of PEEM images showing intermittent turbulence under periodic forcing is displayed in Fig. 9.6. The repeated emergence of localized bubbles is strictly correlated with the period of the driving force. In the shown example, the pattern further undergoes long-term evolution cycles of five forcing periods. The density of bubbles is roughly repeated after such a cycle. To see this, compare the images in the different rows of Fig. 9.6. However, the exact positions of bubbles are not repeated, and some of them disappear or are newly created from one cycle to another, such that the long-term evolution of the pattern is chaotic.



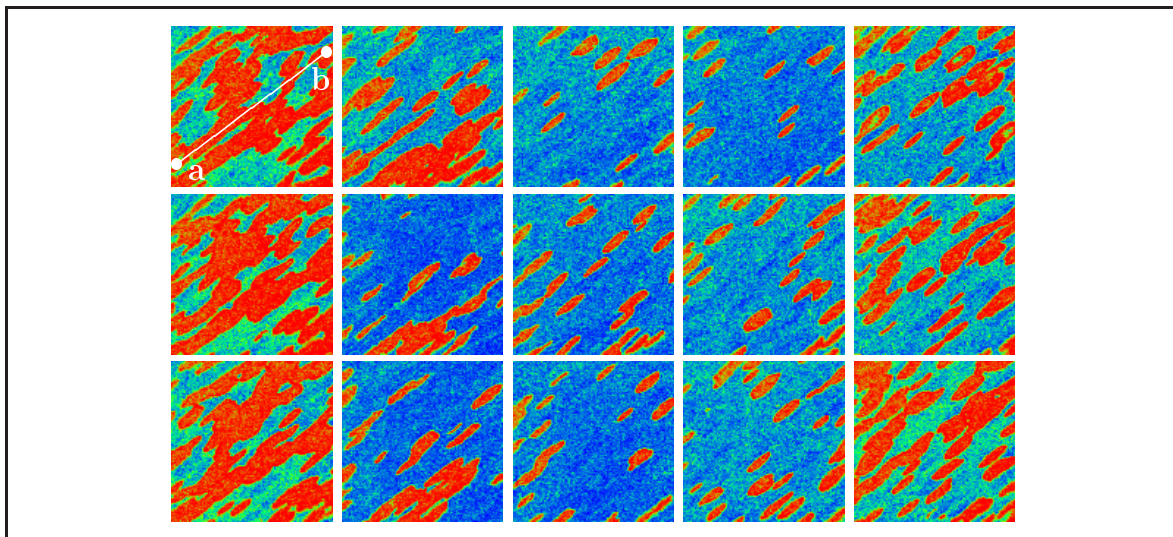


Figure 9.6: Intermittent turbulence under periodic forcing. The time interval between subsequent PEEM images of size  $330 \times 330 \mu\text{m}^2$  is  $\Delta t = 2.1 \text{ s}$  and corresponds to the period of the driving force. The reaction parameters are  $T = 513 \text{ K}$ ,  $p_{\text{O}_2} = 40.0 \times 10^{-5} \text{ mbar}$ , and  $p_0 = 8.7 \times 10^{-5} \text{ mbar}$ . The forcing amplitude is  $\gamma = 10.3 \%$  and the forcing frequency is  $\omega_f/2\pi = 0.48 \text{ Hz}$ .

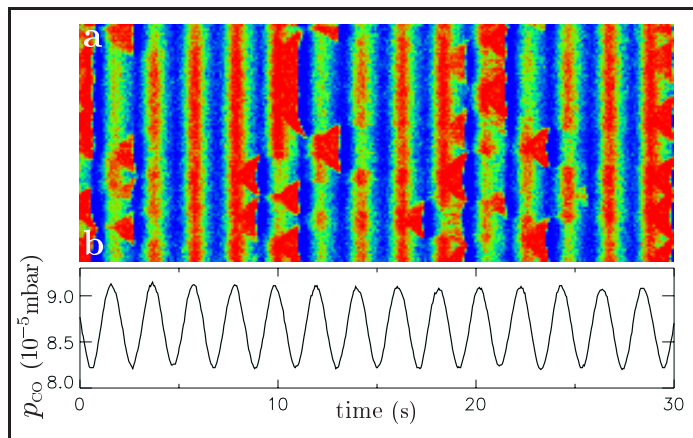


Figure 9.7: Space-time diagram displaying the temporal evolution of the pattern shown in Fig. 9.6 along the line  $ab$  indicated in the first image. For comparison, the curve in the bottom shows the periodically varying signal of CO partial pressure in the reaction chamber.

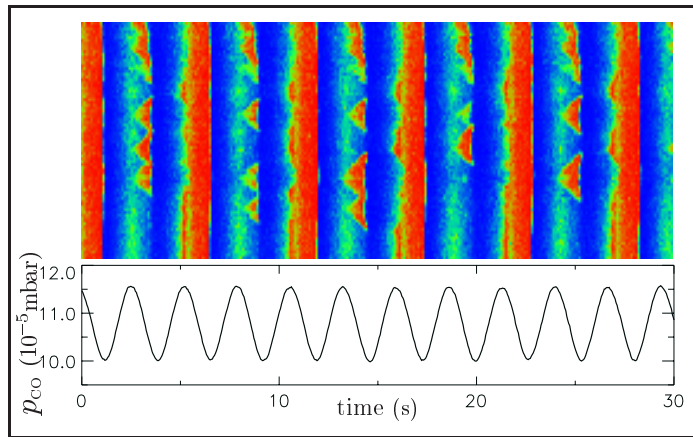


Figure 9.8: Space-time diagram along a cross section through a pattern of intermittent turbulence with period-doubled oscillations. The parameters are  $T = 533 \text{ K}$ ,  $p_{\text{O}_2} = 40.0 \times 10^{-5} \text{ mbar}$ ,  $p_0 = 10.8 \times 10^{-5} \text{ mbar}$ ,  $\gamma = 14.8 \%$ , and  $\omega_f/2\pi = 0.37 \text{ Hz}$ .

It was mentioned before that in the case of harmonic entrainment, either simple periodic or period-doubled uniform oscillations could be observed. This behavior is also reflected by the states of intermittent turbulence found below the harmonic resonance. The space-time diagrams displayed in Figs. 9.7 and 9.8 provide examples of a period-one and a period-two oscillating background, respectively. In the cross section, the localized bubbles are seen as triangular shaped objects.

### 9.1.5 Cellular structures

Oscillating cell arrays, which were also seen under global delayed feedback (cf. Section 8.2.6), represent a further type of pattern that was frequently observed in experiments with periodic forcing. Upon a decrease of the forcing amplitude, such cellular structures arise from locked uniform oscillations as small-amplitude modulations, see Fig. 9.9(a) for a typical PEEM image. Initially, such cells are visible only at a certain point of time during each oscillation cycle and are hardly detectable in a space-time diagram. Upon a further decrease of  $\gamma$ , the size of individual cells significantly grows, see Figs. 9.9(b)– 9.9(d), and they become more strongly developed, such that they are visible for larger fractions of each forcing cycle. Starting from resonant uniform oscillations, the formation of cellular structures has also been observed upon an increase of the forcing frequency.

A typical example of a developed, disordered array of cells is displayed in Fig. 9.10. The four PEEM images in the top row are sampled within a single forcing period. In the first frame, the cells emerge as small CO covered islands while the main part of the surface is mainly covered by oxygen. The bright regions then extend (second frame), until they fill

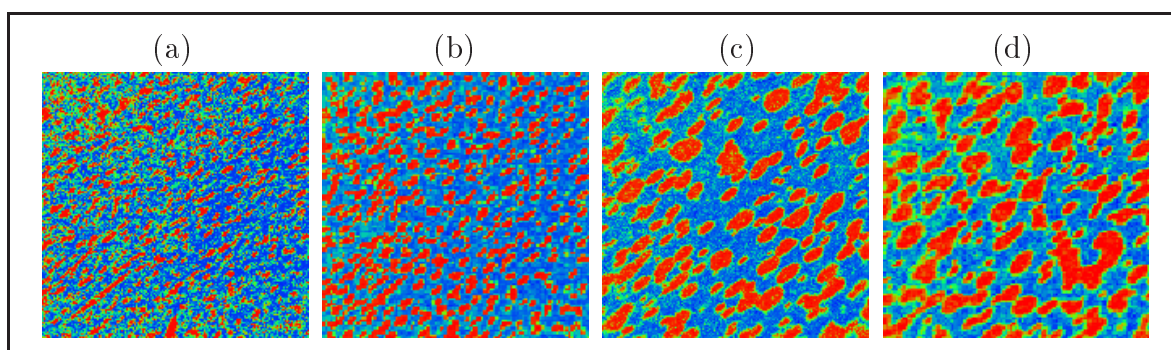


Figure 9.9: Cellular structures at different values of the forcing amplitude. Each PEEM image is  $330 \times 330 \mu\text{m}^2$  in size. The reaction parameters are  $T = 533 \text{ K}$ ,  $p_{\text{O}_2} = 40.0 \times 10^{-5} \text{ mbar}$ , and  $p_0 = 9.0 \times 10^{-5} \text{ mbar}$ . The forcing frequency is  $\omega_f/2\pi = 0.30 \text{ Hz}$  and the forcing amplitude is (a)  $\gamma = 25.2 \%$ , (b)  $23.0 \%$ , (c)  $21.9 \%$ , and (d)  $19.7 \%$ .

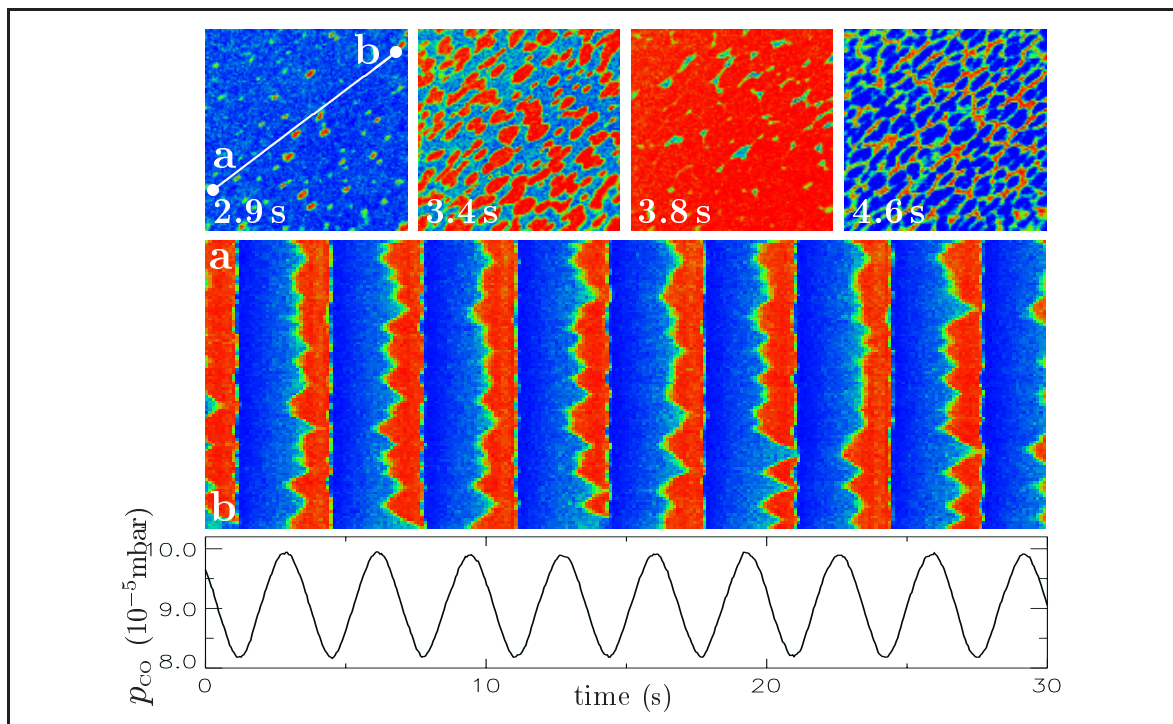


Figure 9.10: *Cellular structures under periodic forcing. Displayed are four subsequent PEEM images of size  $330 \times 330 \mu\text{m}^2$  (top), the evolution along the line  $ab$  indicated in the first image (middle), and the temporal variation of the CO partial pressure in the reaction chamber (bottom). The reaction parameters are the same as in Fig. 9.9. The forcing amplitude is  $\gamma = 19.7\%$  and the forcing frequency is  $\omega_f/2\pi = 0.30\text{ Hz}$ .*

almost the entire imaged surface area (third frame). The cell array is again temporarily seen during the transition back to the mainly oxygen covered state (fourth frame). Such evolution cycles are locked to the forcing period. However, the cell positions change significantly from one cycle to another, such that the cells form a complex, irregular pattern in the space-time diagram.

## 9.2 Discussion

In this chapter, the results of CO oxidation experiments with periodic external forcing have been described. The effects of such forcing have been studied in the case where the unforced reaction exhibited developed chemical turbulence. Such turbulence could be suppressed using relatively large forcing amplitudes. The frequently locked patterns observed in the considered range of forcing parameters exhibited 1:1 or 2:1 entrainment. Below, the observed structures are discussed with respect to results of previous studies performed in the framework of the light-sensitive Belousov-Zhabotinsky (BZ) reaction and the forced complex

Ginzburg-Landau equation (CGLE) (cf. Section 3.1).

Irregular oscillatory stripes with multiple dislocations represent a novel type of structure in catalytic CO oxidation. Such patterns consist of two phase-locked,  $\pi$ -shifted states and are due to 2:1 subharmonic entrainment of local oscillations. They grow via nucleation of stripes at various locations on the surface. A similar growth mechanism was recently described in the framework of the forced complex-Ginzburg-Landau equation, where it led to the development of irregular stripes forming a labyrinthine structure [87]. Standing-wave labyrinthine patterns due to this mechanism were also reported in the light-sensitive Belousov-Zhabotinsky reaction [87]. The labyrinthine organization of these patterns resulted from disinclinations of individual stripes. In contrast, a labyrinthine structure was not seen in the above described experiments. This might be explained by the diffusion anisotropy of the Pt(110) single crystal surface, which favors the orientation of stripes in  $[1\bar{1}0]$  direction. A stretched large-scale labyrinth-like structure was probably also present in the above described experiments, but could not be identified within the relatively small imaged surface area (about  $500\mu\text{m}$  in diameter).

Two-phase clusters represent another 2:1 locked pattern predicted by the forced CGLE, but have not been observed in the experiments with periodic forcing. Note that, however, in the considered temperature range ( $T \approx 535\text{ K}$ ) the time scale of the reaction is relatively fast, and no systematic exploration of the full 2:1 resonance could be undertaken. Phase clusters may still exist at forcing frequencies larger than  $\omega_f/2\pi = 0.5\text{ Hz}$ , which were not accessible due to the limitations of the automated gas inlet system.

A further type of pattern that has been observed under periodic forcing is represented by clusters with coexistent resonances. Similar clusters have also been observed in the CO oxidation model (cf. Section 6.2.4) and in the BZ reaction under global feedback [41]. The simultaneous presence of two or more resonances in a pattern is not possible in the forced CGLE [equation (3.1)] because in this model, the considered resonance is predetermined by the chosen value of  $n$ . Therefore, such clusters cannot be analyzed in its framework.

In addition to frequency locked patterns, non-resonant patterns have been investigated near harmonic resonance. Intermittent turbulence under periodic forcing is characterized by the presence of localized turbulent bubbles on the background of either period-one or period-doubled uniform oscillations. In the forced CGLE, intermittent turbulence has been quite extensively studied in one space dimension [34], but detailed studies in two dimensions are still lacking. Disordered cellular structures represent another type of structure forming due



to competition of a synchronizing effect of forcing and a destabilizing effect of diffusion. Numerical simulations of the amplitude equation have shown a transition from uniform oscillations to small-amplitude hexagonal cells, whose symmetry is then destroyed by further instabilities [62].

In conclusion, by means of periodic external forcing a variety of spatiotemporal patterns could be induced in experiments with CO oxidation on Pt(110). Although the system was not operated close to a Hopf bifurcation and oscillations were far from harmonic, a large part of the observed behavior is qualitatively well described by the forced complex Ginzburg-Landau equation. Other phenomena, such as localized bubble structures on a background of period-doubled uniform oscillations and clusters with coexistent resonances, should be modeled in the framework of the realistic model of CO oxidation. The observations provide a description of the self-organized behavior of a periodically forced oscillatory reaction-diffusion system in a parameter range where the unforced system shows chemical turbulence. Some of the observed structures also appeared under global delayed feedback and similar properties were then found, indicating the possibility of their existence in different environments.

---

## Chapter 10

### Summary

---

The catalytic oxidation reaction of carbon monoxide on a platinum (110) single crystal surface is an example of a reaction-diffusion system known to exhibit rich behavior, including oscillations, chemical waves, and turbulence. In order to control and manipulate turbulence and pattern formation in this system, two different control methods, global delayed feedback and periodic forcing, have been employed. The effects of global delayed feedback on the self-organized behavior of the system have been studied both in a theoretical model of the reaction and in laboratory experiments. The influence of periodic forcing was studied experimentally only. It was found that the chosen control methods allow to suppress turbulence in the considered system, and that they can be successfully used as a tool to produce various complex patterns.

For the theoretical investigations, a realistic three-variable model of CO oxidation on Pt(110) was supplied by an extra term accounting for global delayed feedback. This model was then systematically studied by means of numerical simulations. Two cases have been considered, differing in the behavior of the system in absence of feedback. In both cases, several spatiotemporal patterns could be induced into the system by variation of the two feedback parameters, namely the feedback intensity and the time delay in the feedback loop. The resulting structures have been analyzed using a newly developed transformation to phase and amplitude variables designed for non-harmonic oscillations.

In the first studied case, the model parameters were chosen in such a way that uniform oscillations were stable in absence of feedback. Typical feedback-induced patterns in this case were represented by phase flips, asynchronous oscillations, and dynamical clustering. The existence regions of these patterns in the plane of the feedback parameters have been determined. Phase flips were small traveling objects that shifted the oscillation phase by  $2\pi$ , thereby connecting different uniform regions in a pattern. They disappeared through the

formation of an amplitude defect when the feedback intensity was increased beyond a critical value. Asynchronous oscillations were characterized by smooth spatial phase gradients along a pattern and resulted from a desynchronizing effect of global feedback. Their formation was accompanied by the breakdown of global oscillations.

Three different types of cluster patterns have been identified: amplitude clusters, phase clusters, and cluster turbulence. Amplitude clusters were due to coexistent limit cycles of equal period and consisted of different domains which differed both in their oscillation phase and amplitude. The domain walls were usually stationary. In phase clusters, the phase difference between the two cluster domains was  $\pi$  and the oscillation amplitude was the same. In contrast to amplitude clusters, stationary phase clusters showed the property of phase balance, i.e., the total fractions of the medium occupied by the domains of the different clusters were equal. Two different front instabilities have been observed for stationary phase clusters: a pitchfork bifurcation led to propagation of cluster fronts, and an instability of the state of phase balance resulted in spatial front oscillations. Cluster turbulence was characterized by irregular behavior of phase fronts, which repeatedly split or died out.

In the second studied case, uniform oscillations in the model of CO oxidation were unstable with respect to small perturbations and amplitude turbulence spontaneously developed in absence of feedback. Such turbulence could be suppressed by means of global delayed feedback, and uniform oscillations could be induced in a wide range of feedback parameters. The minimal feedback intensity needed to control turbulence was strongly dependent on the choice of the time delay. Strong hysteresis was found in the transition between the turbulent and the uniform state.

Moreover, near the edge of chaos, where global delayed feedback was too weak to induce uniform oscillations but strong enough to significantly affect pattern formation, a broad variety of complex patterns was found. Synchronization diagrams have been constructed for different initial conditions, revealing the existence regions of such patterns.

Cluster patterns resulted from an incomplete synchronization process. Stationary two-phase clusters showed similar spatial properties as in the case where uniform oscillations were stable in absence of feedback, with the difference that local oscillations were period-doubled. This opened up the possibility for stationary phase fronts in absence of oscillation nodes. In addition to phase clusters, amplitude clusters were found in one of the cluster regions at higher feedback intensities.

A complex spatiotemporal regime of intermittent turbulence was observed under increasing feedback intensity close to the synchronization border. This regime was characterized by cascades of reproducing and annihilating localized structures on the background of uniform oscillations. In two space dimensions, such structures represented bubbles developing into ring-shaped objects. The objects mediating intermittent turbulence were identified as amplitude defects.

Oscillatory standing waves developed from uniform oscillations in one space dimension due to a finite wavelength instability. In two dimensions, nonlinear interactions between three modes with the same wave number resulted in the formation of hexagonal cell arrays. Secondary instabilities of these structures led to breathing waves and cells, and to phase turbulence. Such patterns were stable with respect to small perturbations, but transformed into amplitude turbulence when stronger perturbations were applied.

The simulated phenomena of pattern formation have been tested in laboratory experiments with CO oxidation on Pt(110). Global delayed feedback was artificially introduced into the experimental system via a controlled state-dependent variation of the CO partial pressure in the reaction chamber. The spatiotemporal patterns developing on the catalytic surface have been imaged by means of photoemission electron microscopy.

In these experiments, many of the simulated patterns could be indeed observed. In a non-chaotic parameter regime, characterized by the existence of stable spiral waves in absence of feedback, three different types of dynamical behavior occurred upon application of global delayed feedback: synchronization and desynchronization of local oscillations, and formation of phase clusters. While synchronous oscillations were accompanied by a periodically varying control signal, the process of desynchronization led to the breakdown of global oscillations. Phase clusters showed the property of phase balance and were characterized by a period doubling of local oscillations.

Even richer behavior was found in experiments performed in a parameter regime where the unforced reaction exhibited chemical turbulence. At first, spiral-wave turbulence could be suppressed by applying global delayed feedback. After successful synchronization of local oscillations, the uniform state was maintained by a periodically varying control signal which compensated the destabilizing effect of diffusion. Moreover, a remarkable variety of complex spatiotemporal patterns was found when global delayed feedback was used to bring the system to the border between regular and chaotic dynamics. Intermittent turbulence was characterized by cascades of reproducing and annihilating turbulent bubble structures or

small localized spirals on the background of uniform oscillations. Alternating standing waves and disordered cellular structures represented further results of the action of global delayed feedback. In addition, phase clusters, which showed similar properties as in the non-chaotic parameter regime, were found.

The experimentally observed patterns were transformed into phase and amplitude patterns using a technique based on the Hilbert transform. Good agreement was found between the structures seen in the model and in the experiments. The types of simulated and experimentally observed patterns also to a wide extent resembled the structures found in previous studies [36, 37, 112–114] of the complex Ginzburg-Landau equation with global feedback, even though experiments and simulations were not performed close to a supercritical Hopf bifurcation.

In a further set of experimental investigations, the effects of periodic external forcing on chemical turbulence in CO oxidation on Pt(110) have been studied. At relatively strong forcing, turbulence could be suppressed and frequency locked patterns could be induced. The resonant patterns observed in the considered range of forcing parameters exhibited 1:1 or 2:1 entrainment. They were analyzed using a frequency demodulation technique [40].

Within the 1:1 resonance, local oscillations at all resolving pixels in a pattern synchronized and locked to the forcing frequency. Irregular stripe patterns were observed at underlying 2:1 resonance. Such patterns consisted of phase-locked,  $\pi$ -shifted states and contained multiple dislocations. Upon a suitable change of forcing parameters, they grew from uniform oscillations via nucleation of stripes. Moreover, clusters consisting of complex-shaped domains on a uniform background formed due to coexistent resonances in a pattern.

In addition to frequency locked patterns, two different types of non-resonant patterns arose due to competition of a synchronizing effect of forcing and a destabilizing effect of diffusion. Intermittent turbulence under periodic forcing was characterized by the presence of localized turbulent bubbles on the background of either period-one or period-doubled uniform oscillations. Disordered cellular structures smoothly originated from locked uniform oscillations. The properties of these patterns were similar as when they formed under global delayed feedback. Previous studies [34, 35, 62, 87] of the periodically forced complex Ginzburg-Landau equation provided an interpretation basis for the experimental observations.

---

## Bibliography

---

- [1] G. Nicolis and I. Prigogine, *Self-organization in Nonequilibrium Systems* (Wiley, New York, 1977).
- [2] D. Walgraef, *Spatio-Temporal Pattern Formation* (Springer, New York, 1997).
- [3] N. B. Abraham and W. J. Firth, J. Opt. Soc. Am. B **7**, 6 (1990).
- [4] F. T. Arecchi, S. Boccaletti, G. Giacomelli, G. P. Pucconi, P. L. Ramazza, and S. Residori, Physica D **61**, 25 (1992).
- [5] E. Schöll, *Nonlinear Spatio-Temporal Dynamics and Chaos in Semiconductors* (Cambridge University Press, Cambridge, 2001).
- [6] J. Jalife, J. M. Davidenko, and D. C. Michaels, J. Cardiovasc. Electrophysiol. **2**, 133 (1991).
- [7] P. N. Devreotes, M. J. Potel, and S. A. MacKay, Developments in Biology **96**, 405 (1983).
- [8] *Oscillations and Traveling Waves in Chemical Systems*, edited by R. J. Field and M. Burger (Wiley, New York, 1985).
- [9] M. C. Cross and P. C. Hohenberg, Rev. Mod. Phys. **65**, 851 (1993).
- [10] *Chemical Waves and Patterns*, edited by R. Kapral and K. Showalter (Kluwer, Dordrecht, 1995).
- [11] E. Schrödinger, *What is Life ?* (Cambridge Univ. Press, 1944).
- [12] P. Glandsdorff and I. Prigogine, *Thermodynamic Theory of Structure, Stability and Fluctuations* (Wiley, New York, 1971).
- [13] I. Prigogine, Angew. Chemie **90**, 74 (1978).
- [14] J. M. T. Thompson and H. B. Stewart, *Nonlinear Dynamics and Chaos* (Wiley, Chichester, 1986).
- [15] H. Poincaré, *Les Méthodes Nouvelles de la Mécanique Céleste* (Gauthier-Villard, Paris, 1892).
- [16] H. G. Schuster, *Deterministic Chaos* (VCH, Weinheim, 1988).
- [17] H. Haken, *Synergetics: An Introduction* (Springer, Berlin, 1978).

- [18] Z. Noszticzius, W. Horsthemke, W. D. McCormick, and H. L. Swinney, *Nature* **329**, 6140 (1987).
- [19] A. M. Zhabotinsky, *Chaos* **1**, 379 (1991).
- [20] A. N. Zaikin and A. M. Zhabotinsky, *Nature* **225**, 535 (1970).
- [21] A. T. Winfree, *Science* **175**, 634 (1972).
- [22] A. S. Mikhailov, *Foundations of Synergetics I* (Springer, Berlin, 1994).
- [23] A. S. Mikhailov and A. Y. Loskutov, *Foundations of Synergetics II* (Springer, Berlin, 1996).
- [24] L. Q. Zhou and Q. Ouyang, *J. Phys. Chem. A* **105**, 112 (2001).
- [25] Y. Kuramoto, *Chemical Oscillations, Waves, and Turbulence* (Springer, Berlin, 1984).
- [26] A. M. Turing, *Phil. Trans. Roy. Soc. B* **237**, 37 (1952).
- [27] V. Castets, E. Dulos, J. Boissonade, and P. de Kepper, *Phys. Rev. Lett.* **64**, 2953 (1990).
- [28] Q. Ouyang and H. L. Swinney, *Nature* **352**, 610 (1991).
- [29] L. L. Hegedus, C. C. Chang, D. J. McEwer, and E. M. Sloan, *Ind. Eng. Chem. Fundam.* **19**, 367 (1980).
- [30] M. B. Cutlip, C. J. Hawkins, D. Mukesh, W. Morton, and C. N. Kenney, *Chem. Eng. Commun.* **22**, 329 (1983).
- [31] G. Vaporciyan, A. Annapragada, and E. Gulari, *Chem. Eng. Sci.* **43**, 2957 (1988).
- [32] P. Coullet, J. Lega, B. Houchmanzadeh, and J. Lajzerowicz, *Phys. Rev. Lett.* **65**, 1352 (1990).
- [33] C. Elphick, A. Hagberg, and E. Meron, *Phys. Rev. Lett.* **80**, 5007 (1998).
- [34] H. Chaté, A. Pikovsky, and O. Rudzick, *Physica D* **131**, 17 (1999).
- [35] H.-K. Park, *Phys. Rev. Lett.* **86**, 1130 (2001).
- [36] D. Battogtokh and A. S. Mikhailov, *Physica D* **90**, 84 (1996).
- [37] D. Battogtokh, A. Preusser, and A. S. Mikhailov, *Physica D* **106**, 327 (1997).
- [38] G. Franceschini, S. Bose, and E. Schöll, *Phys. Rev. E* **60**, 5426 (1999).
- [39] V. Petrov, Q. Ouyang, and H. L. Swinney, *Nature* **388**, 655 (1997).
- [40] A. L. Lin, M. Bertram, K. Martinez, H. L. Swinney, A. Ardelea, and G. F. Carey, *Phys. Rev. Lett.* **84**, 4240 (2000).



- [41] V. K. Vanag, L. Yang, M. Dolnik, A. M. Zhabotinsky, and I. R. Epstein, *Nature* **406**, 389 (2000).
- [42] V. K. Vanag, A. M. Zhabotinsky, and I. R. Epstein, *Phys. Rev. Lett.* **86**, 552 (2001).
- [43] R. Imbuhl and G. Ertl, *Chem. Rev.* **95**, 697 (1995).
- [44] G. Ertl, P. R. Norton, and J. Rüstig, *Phys. Rev. Lett.* **49**, 177 (1982).
- [45] H. H. Rotermund, W. Engel, M. Kordesch, and G. Ertl, *Nature* **343**, 355 (1990).
- [46] S. Jakubith, H. H. Rotermund, W. Engel, A. von Oertzen, and G. Ertl, *Phys. Rev. Lett.* **65**, 3013 (1990).
- [47] C. Sachs, M. Hildebrand, S. Völkening, J. Wintterlin, and G. Ertl, *Science* **293**, 1635 (2001).
- [48] J. Guckenheimer and P. J. Holmes, *Nonlinear Oscillations, Dynamical Systems and Bifurcations of Vector Fields* (Springer, New York, 1983).
- [49] K. Krischer, Dissertation, Free University of Berlin (1990).
- [50] V. S. Zykov, *Biophysics (GB)* **32**, 385 (1987).
- [51] M. Bär and M. Eiswirth, *Phys. Rev. E* **48**, R1635 (1993).
- [52] M. Stich, Diploma Thesis, Free University of Berlin (1999).
- [53] M. Stich, M. Ipsen, and A. S. Mikhailov, *Phys. Rev. Lett.* **86**, 4406 (2001).
- [54] I. S. Aranson and L. Kramer, *Rev. Mod. Phys.* **74**, 99 (2002).
- [55] M. Ipsen, Dissertation, University of Copenhagen (1996).
- [56] B. I. Shraiman, A. Pumir, W. van Saarloos, P. C. Hohenberg, H. Chaté, and M. Holen, *Physica D* **57**, 241 (1992).
- [57] H. Chaté, in *Spatiotemporal Patterns in Nonequilibrium Complex Systems, Santa Fe Institute Series in the Sciences of Complexity* (Addison-Wesley, Reading, 1993).
- [58] M. van Hecke, *Phys. Rev. Lett.* **80**, 1896 (1998).
- [59] H. Chaté and P. Manneville, *Physica A* **224**, 348 (1996).
- [60] L. Gil, J. Lega, and J. L. Meunier, *Phys. Rev. A* **41**, 1138 (1990).
- [61] G. Huber, P. Alstrøm, and T. Bohr, *Phys. Rev. Lett.* **69**, 2380 (1992).
- [62] P. Coullet and K. Emilsson, *Physica D* **61**, 119 (1992).
- [63] H. Gang and H. Kaifen, *Phys. Rev. Lett.* **71**, 3794 (1993).

- [64] I. Aranson, H. Levine, and L. Tsimring, Phys. Rev. Lett. **72**, 2561 (1994).
- [65] W. Lu, D. Yu, and R. G. Harrison, Phys. Rev. Lett. **76**, 3316 (1996).
- [66] M. E. Bleich and J. E. S. Socolar, Phys. Rev. E **54**, R17 (1996).
- [67] R. Martin, A. J. Scroggie, G.-L. Oppo, and W. J. Firth, Phys. Rev. Lett. **77**, 4007 (1996).
- [68] M. E. Bleich, D. Hochheiser, J. V. Moloney, and J. E. S. Socolar, Phys. Rev. E **55**, 2119 (1997).
- [69] M. Münkkel, F. Kaiser, and O. Hess, Phys. Rev. E **56**, 3868 (1997).
- [70] R. O. Grigoriev, M. C. Cross, and H. G. Schuster, Phys. Rev. Lett. **79**, 2795 (1997).
- [71] S. Sinha and N. Gupte, Phys. Rev. E **58**, R5221 (1998).
- [72] J. Buck and E. Buck, Sci. Am. **234**, 74 (1976).
- [73] M. R. Guevara and L. Glass, J. Math. Biology **14**, 1 (1982).
- [74] T. Bohr, P. Bak, and M. H. Jensen, Phys. Rev. A **30**, 1970 (1984).
- [75] M. Eiswirth and G. Ertl, Phys. Rev. Lett. **60**, 1526 (1988).
- [76] L. Pivka, A. L. Zheleznyak, and L. O. Chua, Int. J. of Bif. and Chaos **4**, 1743 (1994).
- [77] F.-J. Niedernostheide, C. Brillert, B. Kukuk, H.-G. Purwins, and H.-J. Schulze, Phys. Rev. B **54**, 14012 (1996).
- [78] M. Bertram, M.A. Thesis, University of Texas at Austin (1999).
- [79] V. I. Arnol'd, Am. Math. Soc. Trans. **46**, 213 (1965).
- [80] E. Ott, *Chaos in Dynamical Systems* (Cambridge University Press, Cambridge (UK), 1993).
- [81] V. Petrov, M. Gustafsson, and H. L. Swinney, *Proceedings of the Fourth Experimental Chaos Conference* (World Scientific, Singapore, 1998).
- [82] T. Mizuguchi and S. Sasa, Prog. Theor. Phys. **89**, 599 (1993).
- [83] C. Elphick, A. Hagberg, and E. Meron, Phys. Rev. E **59**, 5285 (1999).
- [84] C. J. Hemming and R. Kapral, Chaos **10**, 720 (2000).
- [85] J. M. Gambaudo, J. Diff. Eq. **57**, 172 (1985).
- [86] C. Elphick, G. Iooss, and E. Tirapegui, Phys. Lett. A **120**, 459 (1987).
- [87] A. Yochelis, A. Hagberg, E. Meron, A. L. Lin, and H. L. Swinney, submitted to SIAM J. of Appl. Dyn. Systems (2002).

- [88] A. L. Lin, A. Hagberg, A. Ardelea, M. Bertram, H. L. Swinney, and E. Meron, *Phys. Rev. E* **62**, 3790 (2000).
- [89] O. Steinbock, V. Zykov, and S. C. Müller, *Nature* **366**, 322 (1993).
- [90] M. Braune and H. Engel, *Chem. Phys. Lett.* **211**, 534 (1993).
- [91] M. Braune, A. Schrader, and H. Engel, *Chem. Phys. Lett.* **222**, 358 (1994).
- [92] A. Schrader, M. Braune, and H. Engel, *Phys. Rev. E* **52**, 98 (1995).
- [93] I. Sendiña-Nadal, E. Mihaliuk, J. Wang, V. Pérez-Muñuzuri, and K. Showalter, *Phys. Rev. Lett.* **86**, 1646 (2001).
- [94] G. Nicolis, *Adv. Chem. Phys.* **19**, 209 (1971).
- [95] A. L. Pardhanani and G. F. Carey, *J. Comp. Appl. Math.* **74**, 295 (1996).
- [96] E. Ott, C. Grebogi, and J. A. Yorke, *Phys. Rev. Lett.* **64**, 1196 (1990).
- [97] K. Pyragas, *Phys. Lett. A* **170**, 421 (1992).
- [98] S. Bielawski, M. Bouazaoui, and P. Glorieux, *Phys. Rev. A* **47**, 3276 (1993).
- [99] J. E. S. Socolar, D. W. Sukow, and D. J. Gauthier, *Phys. Rev. E* **50**, 3245 (1994).
- [100] W. Wang, I. Z. Kiss, and J. L. Hudson, *Phys. Rev. Lett.* **86**, 4954 (2001).
- [101] P. Parmananda and M. Eiswirth, *J. Phys. Chem. A* **103**, 5510 (1999).
- [102] P. Parmananda and J. L. Hudson, *Phys. Rev. E* **64**, 037201 (2001).
- [103] L. Yang, M. Dolnik, A. M. Zhabotinsky, and I. R. Epstein, *Phys. Rev. E* **62**, 6414 (2000).
- [104] V. K. Vanag, A. M. Zhabotinsky, and I. R. Epstein, *J. Phys. Chem. A* **104**, 11566 (2000).
- [105] K. Krischer and A. Mikhailov, *Phys. Rev. Lett.* **73**, 3165 (1994).
- [106] S. Grill, V. S. Zykov, and S. C. Müller, *Phys. Rev. Lett.* **75**, 3368 (1995).
- [107] V. S. Zykov, A. S. Mikhailov, and S. C. Müller, *Phys. Rev. Lett.* **78**, 3398 (1997).
- [108] O.-U. Kheowan, C.-K. Chan, V. S. Zykov, O. Rangsiman, and S. C. Müller, *Phys. Rev. E* **64**, 035201(R) (2001).
- [109] E. Mihaliuk, T. Sakurai, F. Chirila, and K. Showalter, *Discuss. Faraday Soc.* (to be published).
- [110] M. E. Bleich and J. E. S. Socolar, *Phys. Lett. A* **210**, 87 (1996).

- [111] W. Just, E. Reibold, H. Benner, K. Kacperski, P. Fronczak, and J. Holyst, *Phys. Lett. A* **254**, 158 (1999).
- [112] F. Mertens, R. Imbihl, and A. Mikhailov, *J. Chem. Phys.* **99**, 8668 (1993).
- [113] F. Mertens, R. Imbihl, and A. Mikhailov, *J. Chem. Phys.* **101**, 9903 (1994).
- [114] M. Falcke, H. Engel, and M. Neufeld, *Phys. Rev. E* **52**, 763 (1995).
- [115] P. Hugo, *Ber. Bunsen-Ges. Phys. Chem.* **74**, 121 (1970).
- [116] H. Beusch, D. Fieguth, and E. Wicke, *Chem. Eng. Tech.* **44**, 445 (1972).
- [117] G. Ertl, *Adv. Catal.* **37**, 213 (1990).
- [118] M. Eiswirth and G. Ertl, *Surf. Sci.* **177**, 90 (1986).
- [119] M. Eiswirth, K. Krischer, and G. Ertl, *Surf. Sci.* **202**, 565 (1988).
- [120] M. Eiswirth, P. Möller, and G. Ertl, *Surf. Sci.* **208**, 13 (1989).
- [121] S. Nettesheim, A. von Oertzen, H. H. Rotermund, and G. Ertl, *J. Chem. Phys.* **98**, 9977 (1993).
- [122] S. Jakubith, Dissertation, Free University of Berlin (1991).
- [123] W. Engel, M. E. Kordesch, H. H. Rotermund, S. Kubala, and A. von Oertzen, *Ultramicroscopy* **36**, 148 (1991).
- [124] H. H. Rotermund, *Surf. Sci. Rep.* **29**, 265 (1997).
- [125] H. H. Rotermund, S. Jakubith, A. von Oertzen, and G. Ertl, *Phys. Rev. Lett.* **66**, 3083 (1991).
- [126] K. C. Rose, D. Battogtokh, A. Mikhailov, R. Imbihl, W. Engel, and A. M. Bradshaw, *Phys. Rev. Lett.* **76**, 3582 (1996).
- [127] M. D. Graham, I. G. Kevrekidis, K. Asakura, J. Lauterbach, K. Krischer, H. H. Rotermund, and G. Ertl, *Science* **264**, 80 (1994).
- [128] M. Pollmann, H. H. Rotermund, G. Ertl, X. Li, and I. G. Kevrekidis, *Phys. Rev. Lett.* **86**, 6038 (2001).
- [129] J. Wolff, A. G. Papathanasiou, I. G. Kevrekidis, H. H. Rotermund, and G. Ertl, *Science* **294**, 134 (2001).
- [130] H. H. Rotermund, G. Haas, R. U. Franz, R. M. Tromp, and G. Ertl, *Science* **270**, 608 (1995).
- [131] H. H. Rotermund, *Surf. Sci.* **386**, 10 (1997).
- [132] J. Lauterbach, G. Haas, H. H. Rotermund, and G. Ertl, *Surf. Sci.* **294**, 116 (1993).

- 
- [133] A. von Oertzen, A. S. Mikhailov, H. H. Rotermund, and G. Ertl, *J. Phys. Chem. B* **102**, 4966 (1998).
- [134] R. Imbihl and G. Voser, *J. Vac. Sci. Technol. A* **12**, 2170 (1994).
- [135] M. Eiswirth, K. Krischer, and G. Ertl, *Appl. Phys. A* **51**, 79 (1990).
- [136] K. Krischer, M. Eiswirth, and G. Ertl, *Surf. Sci.* **251/252**, 900 (1991).
- [137] K. Krischer, M. Eiswirth, and G. Ertl, *J. Chem. Phys.* **96**, 9161 (1992).
- [138] R. P. H. Gasser, *An Introduction to Chemisorption and Catalysis by Metals* (Clarendon Press, Oxford, 1985).
- [139] A. von Oertzen, A. S. Mikhailov, H. H. Rotermund, and G. Ertl, *Surf. Sci.* **350**, 259 (1996).
- [140] K. Krischer, M. Eiswirth, and G. Ertl, *J. Chem. Phys.* **97**, 307 (1992).
- [141] M. Bär, M. Eiswirth, H. H. Rotermund, and G. Ertl, *Phys. Rev. Lett.* **69**, 945 (1992).
- [142] M. Bär, M. Falcke, C. Zülicke, H. Engel, M. Eiswirth, and G. Ertl, *Surf. Sci.* **269/270**, 471 (1992).
- [143] M. Bär, M. Falcke, and M. Eiswirth, *Physica A* **188**, 78 (1992).
- [144] D. Barkley, *Physica D* **49**, 61 (1991).
- [145] M. Bär, N. Gottschalk, M. Eiswirth, and G. Ertl, *J. Chem. Phys.* **100**, 1202 (1994).
- [146] M. Bär, S. Nettesheim, H. H. Rotermund, M. Eiswirth, and G. Ertl, *Phys. Rev. Lett.* **74**, 1246 (1995).
- [147] M. Hildebrand, M. Bär, and M. Eiswirth, *Phys. Rev. Lett.* **75**, 1503 (1995).
- [148] H. Levine and X. Zou, *Phys. Rev. Lett.* **69**, 204 (1992).
- [149] H. Levine and X. Zou, *Phys. Rev. E* **48**, 50 (1993).
- [150] M. Falcke and H. Engel, *Phys. Rev. E* **50**, 1353 (1994).
- [151] M. Falcke and H. Engel, *J. Chem. Phys.* **101**, 6255 (1994).
- [152] M. Falcke and H. Engel, *Phys. Rev. E* **56**, 635 (1997).
- [153] A. von Oertzen, H. H. Rotermund, A. S. Mikhailov, and G. Ertl, *J. Phys. Chem. B* **104**, 3155 (2000).
- [154] J. M. Hyman, R. J. Knapp, and J. C. Scovel, *Physica D* **60**, 112 (1992).
- [155] W. H. Press, S. A. Teukolsky, W. T. Vetterling, and B. P. Flannery, *Numerical Recipes in C* (Cambridge University Press, Cambridge (USA), 1992).

- [156] K. J. Lee, W. McCormick, J. E. Pearson, and H. L. Swinney, *Nature* **369**, 215 (1994).
- [157] D. Lima, D. Battogtokh, A. Mikhailov, P. Borckmans, and G. Dewel, *Europhys. Lett.* **42**, 631 (1998).
- [158] H. Chaté, *Nonlinearity* **7**, 185 (1994).
- [159] M. Pollmann, Dissertation, Free University of Berlin (2002).
- [160] A. von Oertzen, Diploma Thesis, Free University of Berlin (1990).
- [161] A. von Oertzen, Dissertation, Free University of Berlin (1992).
- [162] M. Pollmann, M. Bertram, and H. H. Rotermund, *Chem. Phys. Lett.* **346**, 123 (2001).
- [163] M. Kim, M. Bertram, M. Pollmann, A. von Oertzen, A. S. Mikhailov, H. H. Rotermund, and G. Ertl, *Science* **292**, 1357 (2001).
- [164] P. Panter, *Modulation, Noise, and Spectral Analysis* (McGraw-Hill, New York, 1965).
- [165] M. Rosenblum and J. Kurths, in *Nonlinear Analysis of Physiological Data*, edited by H. Kantz, J. Kurths, and G. Mayer-Kress (Springer, Berlin, 1998), p. 91.
- [166] N. H. Packard, J. P. Crutchfield, J. D. Farmer, and R. S. Shaw, *Phys. Rev. Lett.* **45**, 712 (1980).
- [167] A. M. Fraser and H. L. Swinney, *Phys. Rev. A* **33**, 1134 (1986).
- [168] M. G. Rosenblum, A. Pikovsky, and J. Kurths, *Phys. Rev. Lett.* **76**, 1804 (1996).

---

## *I would like to thank ...*

---

- ... the Deutsche Forschungsgemeinschaft for financial support under SFB 555 “Complex Nonlinear Processes”.
- ... Gerhard Ertl for giving me the opportunity to prepare this work in an excellent scientific environment.
- ... Alexander S. Mikhailov for suggesting a very interesting project and for his professional advice and support that made this dissertation possible.
- ... Harm H. Rotermund for giving me the opportunity to perform experiments in his lab and for his trust in my abilities.
- ... Michael Pollmann for introducing me into the experimental setup and, together with Minseok Kim, for the successful experimental collaboration.
- ... Mads Ipsen, Michael Stich, and Alexander von Oertzen for many helpful discussions.
- ... Dieter Bauer for technical assistance.
- ... Michael Stich, Carsten Beta, and Vanessa Casagrande for reading and correcting the manuscript.
- ... all members of the Complex Systems Group and the Surface Reactions Imaging Group for the pleasant interaction.
- ... and, last but not least, my parents Beate and Horst-Günther for all their support, and Ulrike for making the past years to a very special, wonderful time for me.





---

## Curriculum Vitae

---

Name	Matthias Bertram
Born	July 6, 1975 in Wermelskirchen, Germany
Parents	Beate and Horst-Günther Bertram
1981 - 1985	Katholische Grundschule Remscheid-Lüttringhausen (Elementary School)
1985 - 1994	Ernst-Moritz-Arndt-Gymnasium Remscheid (Secondary School) 05/94: Abitur (School Leaving Examination)
08/94 - 10/95	Civilian Service at the Hospital zum Heiligen Geist, Hagen
10/95 - 07/98	Physics Student at the Ludwig-Maximilians-Universität Würzburg 08/97: Pre-Diploma
03/98 - 09/99	Fellow of the Studienstiftung des Deutschen Volkes
08/98 - 05/99	Scholarship of the W. E. Heraeus Foundation
08/98 - 08/99	Graduate Student at the University of Texas at Austin 08/99: Master of Arts Degree in Physics Thesis Supervisor: Prof. Dr. H. L. Swinney
10/99	Beginning of Ph.D. Studies at the Department of Physical Chemistry, Fritz-Haber-Institut der Max-Planck-Gesellschaft, Berlin Thesis Supervisor: Prof. Dr. A. S. Mikhailov

